# 3D analysis of fracture processes in concrete

Lilliu, G

**Publication date**
2007

**Document Version**
Final published version

**Citation (APA)**
Lilliu, G. (2007). *3D analysis of fracture processes in concrete*. [Dissertation (TU Delft), Delft University of Technology].
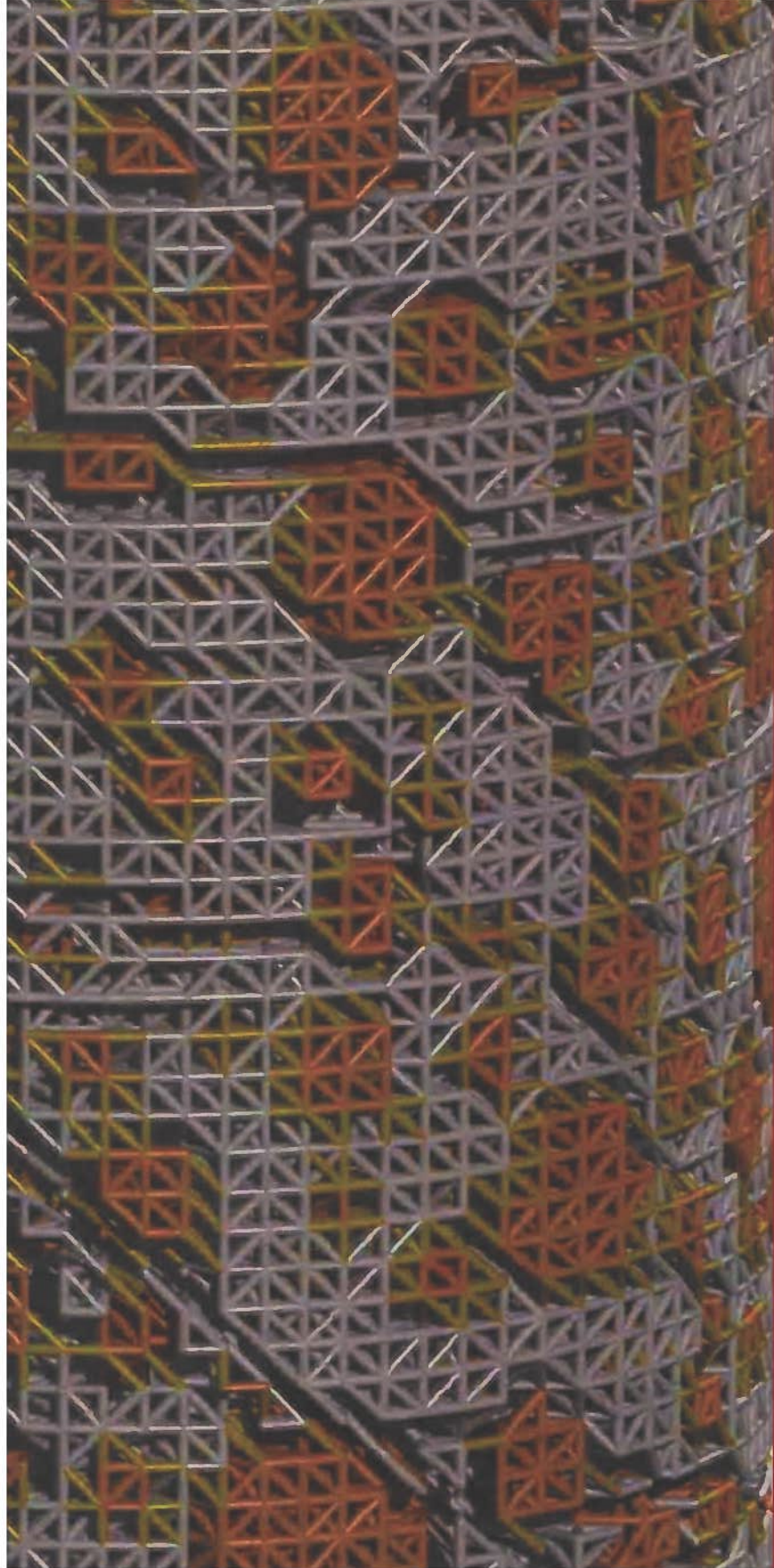
**Important note**
To cite this publication, please use the final published version (if applicable).
Please check the document version above.

**3D Analysis of Fracture Processes in Concrete**

Giovanna Lilliu

# 3D Analysis of Fracture Processes in Concrete

# 3D Analysis of Fracture Processes in Concrete

Proefschrift

ter verkrijging van de graad van doctor
aan de Technische Universiteit Delft,
op gezag van de Rector Magnificus prof.dr.ir. J.T. Fokkema,
voorzitter van het College voor Promoties,
in het openbaar te verdedigen
op dinsdag 8 mei 2007 te 10.00 uur

door

## Giovanna LILLIU

Dottore in Ingegneria
Universitá degli Studi di Cagliari, Italië

geboren te Tuili, Italië

Dit proefschrift is goedgekeurd door de promotor:
Prof.dr.ir. J.G.M. van Mier

Samenstelling promotiecommissie:

| | |
|---|---|
| Rector Magnificus | voorzitter |
| Prof.dr.ir. J.G.M. van Mier | Eidgenössische Technische Hochschule Zürich |
| Prof.dr. J.E. Bolander | University of California Davis |
| Prof.dr.ir. M.G.D. Geers | Technische Universiteit Eindhoven |
| Prof.dr. H.J. Herrmann | Eidgenössische Technische Hochschule Zürich |
| Prof.dr.ir. J.G. Rots | Technische Universiteit Delft |
| Prof.dr.ir. L.J. Sluys | Technische Universiteit Delft |
| Prof.dr.ir. J.C. Walraven | Technische Universiteit Delft |

*To Anna, my daughter*
*To my mother*

*In memory of my father*

# Acknowledgements

# Contents

# List of symbols

$\alpha$      fraction of bending moment contributing to the critical stress

$A$      size of the regular grid in the Voronoi construction

$s$      size of the sub-cell in the Voronoi construction

$A/s$      randomness of the lattice

$d_a$      particle diameter

$d_{a,min}$      minimum particle diameter

$d_{a,max}$      maximum particle diameter

$\delta$      vertical displacement

$\delta_{peak}$      vertical displacement at the peak load

$\varepsilon$      normal strain

$E_a$      Young's modulus of aggregate lattice beams

$E_m$      Young's modulus of matrix lattice beams

$E_b$      Young's modulus of bond lattice beams

$E_{b,eq}$      Young's modulus of bond lattice beams in a series system

$E_{beam}$      Young's modulus of lattice beams in a homogeneous lattice

$E^*$      averaged Young's modulus of the lattice

$f_{t,a}$      tensile strength of aggregate lattice beams

$f_{t,m}$      tensile strength of matrix lattice beams

$f_{t,b}$      tensile strength of bond lattice beams

$F$      load

$F_{peak}$      peak load

$G^*$      averaged shear modulus of the lattice

$h$      height of the rectangular cross section in a 2D lattice, diameter of the circular cross section in a 3D lattice

$K^*$      averaged bulk modulus of the lattice

$l$      length of the lattice beam in a regular lattice

$l_{beam}$      length of the lattice beam

$l_{avr}$      average beam length in a random lattice

$\nu^*$      averaged Poisson's ratio of the lattice

$M_x, M_y$      bending moments in the lattice beam

$N$      axial force in the lattice beam

$P_k$      volumetric particle density before lattice overlay

ix

| | |
|---|---|
| $P_{k,latt}$ | density of aggregate lattice beams |
| $\sigma$ | normal stress |
| $\sigma^*$ | critical normal stress in the lattice beam |
| $S$ | area of the lattice beam's cross section |
| $V_{aggr}$ | particle volume |
| $W$ | section modulus of the lattice beam |
| $W_f^*$ | area under the post-peak branch of the dimensionless load-displacement diagram (where loads and displacements are divided by the corresponding values at the peak load) |

# Chapter 1

# Introduction

*Heterogeneity* and *discontinuity* are the most important concepts involved with mechanics of concrete. Heterogeneity is related to the structure of the material, which is obtained from a mix of aggregates, cement and water. The water reacts with the grains of cement producing a paste which hardens and binds the aggregates. The characteristics of the final product depend on the quantity and characteristics of each component, and the way they interact. Discontinuity is related to the presence of cracks in concrete structures during all their life. Already at the early age, before external loads are applied, shrinkage cracks are present. Fracture models in concrete, however, often consider material as homogeneous, or cracks as continuous, or both. This implies the definition of *averaged material properties*, which are difficult to be measured in laboratory experiments, or even without a clear physical meaning.

Both concepts of *heterogeneity* and *discontinuity* can be included easily and in a straight-forward manner in lattice models. This thesis will focus on such a model, where the material is discretized with a network of elements that follow the Bernoulli beam theory. This model is the 3D version of the original 2D *Delft lattice model*, which was based on the idea of Jan van Mier and first developed in close collaboration with Erik Schlangen [81].

## 1.1  Background and objectives

Lattice models are commonly used in computational physics as approximation of continuum theory. Since the 1980s these models have become increasingly popular in statistical physics for studying disordered materials. The 2D *Delft lattice model* originates from the square beam lattice developed by Herrmann et al.[41], where the quadrilateral lattice is replaced with a triangular lattice, and the breaking thresholds are assigned after overlaying of a computer-generated particle distribution on top of the lattice, rather than being randomly distributed. Simulations of a wide variety of laboratory experiments with the 2D *Delft lattice model* showed that, while the crack patterns and the load-displacement

diagrams were qualitatively correct, the response of the structure predicted in the numerical experiments was far too brittle in comparison with the laboratory experiments. The concepts of brittleness and of ductility are elucidated in Figure 1.1, which represents dimensionless diagrams of uni-axial tensile tests performed with a 2D and a 3D lattice model. The response of the structure is relatively brittle when the descending branch is steeper. In this thesis the notion of ductility is related to the relative amount of energy required for formation and propagation of macro-cracks in the structure (see Chapter 4).
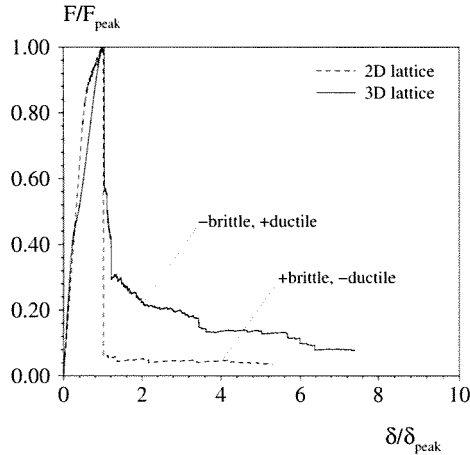


Figure 1.1: Comparison between dimensionless load-displacement diagrams obtained from a 2D and a 3D lattice analysis.

The reasons addressed as cause of the brittle response were two: (1) the smaller fractions of the particle distributions are neglected; (2) 3D effects are neglected. Schlangen and van Mier [83] have shown that inclusion of smaller particles increases crack branches and bridges (see Chapter 4) and, as a result, the ductility of the structural responses. The very first 3D analysis with the beam lattice model was already conducted in 1994 [84] but showed an even more brittle behaviour than observed in the 2D analyses, probably because a too coarse mesh was adopted. Later, Vervuurt [103] used a simplified model where parallel 2D lattices are connected with springs to prove that a 3D model gives a more ductile response than a 2D model. An attempt to include 3D effects was also made by introducing a step-wise removal of each element, in order to simulate gradual progression of the crack through the specimen [4]. However this procedure still required long computational times, which could not be afforded at that time. An attempt to consider 3D effects was also made by Bolander and Kobashi [18], who considered a gradual reduction of the element's stiffness upon violation of the fracture criterion, by means of a damage variable. The importance of including the third direction in modelling fracture of concrete cannot be questioned. A 3D model cannot be avoided in some cases, when the combination of load and boundary conditions cause crack patterns oriented in all three directions

(an example is the torsion experiment in Chapter 6). Even when the applied load and boundary conditions would produce a planar crack in a homogeneous material, the crack is still three-dimensional in concrete. In fact, the presence of randomly distributed aggregates that work as crack arrestors causes deviations of the crack from the straight pattern. The 2D lattice schematizes a 3D model where aggregates are cylinders, and cracks cross the complete depth of the specimen as soon as they form. In the 3D lattice aggregates are modelled as spheres that are randomly distributed in the space. In this case the crack pattern becomes tortuous and, as the area of the crack surface increases, also the energy necessary to form such a crack does.

The purely brittle local fracture criterion adopted in the beam lattice model is sometimes indicated as another reason of the brittle 2D lattice response. This led to the suggestion to include in the model a non-linear stress-strain relation at beam level [3]. A more ductile response of the lattice is also obtained when permanent deformations are taken into account [98].

The objective of this thesis was to develop a 3D version of the 2D Delft lattice model, and to carry out a series of experiments for validation of the model. The only limitation to a 3D version of the lattice model was the computer power. For this reason, the model was implemented in a code for parallel computing [59]. For sake of computational time still relatively small specimens and coarse meshes were used. However, the schematization of the material was much more detailed than in the early 2D analyses: for example, the 2D analyses reported in Chapter 4 and Chapter 5 of this thesis are performed using beams with 0.25 mm length, while in the early 2D analyses lengths of 1.0-2.5 mm were adopted. In this manner a more detailed study of the influence of the material structure on the response of the lattice was possible. Last, and most important, it was possible to include 3D effects.

## 1.2   Outline

The rest of this chapter reviews different types of models for analysis of fracture in concrete. These models are generally classified as homogeneous/heterogeneous, continuous/discontinuous, and discrete models. In Chapter 2, the beam lattice model is outlined. The construction of the lattice geometry, the implementation of the heterogeneities, the simulation of the fracture process and the fracture criterion form the object of this chapter. The effect of the bending moment and its contribution to the critical stress (e.g. the stress that causes failure of the beam) is studied in the 3D case and compared with previous results from 2D analyses.

In Chapter 3, the overall elastic properties of the 3D lattice are determined numerically and compared with analytical models, both in the case of a homogeneous and of a heterogeneous lattice. The 3D results are also compared with earlier 2D results. The assumption of a plane stress or plane strain equivalent 2D continuum is critically reviewed in this chapter, with reference to the effect that such an assumption has on the fracture mechanisms.

Chapter 4 and Chapter 5 are dedicated to the influence of the material structure on the overall fracture behaviour of the lattice.

In Chapter 4 the effect of the particle density on the fracture mechanism is studied both in the 2D and the 3D case. The numerical study is conducted on a relatively small specimen under uni-axial tension, and the results are compared with experiments.

In Chapter 5 the effect of the properties of the interfacial transition zone is studied. First, different thicknesses are considered using a 2D lattice. Then, the elastic properties of the interfacial transition zone are varied. Finally, the effect of the tensile strength of the interface is studied using a 3D lattice.

In Chapter 6 the 3D lattice is applied to a real scale laboratory experiment where a specimen is subjected to torsion. The crack pattern and the torque-rotation diagram are compared with those obtained from laboratory experiments, where cracks were detected not only on the surface of the specimen by means of the naked eye, but also inside the specimen using an impregnation technique.

In Chapter 7 conclusions of the work conducted and perspectives for future research in this subject are drawn.

## 1.3   Models of fracture in concrete

Concrete fracture models can be typified into homogeneous and heterogeneous. These models, in turn, can be classified as continuum, *piece-wise* continuum, discrete and lattice models. Continuum models are based on continuum mechanics theory, which considers the displacement field everywhere continuous and differentiable. In piece-wise continuum models, continuum mechanics theory is still applied in the bulk of the structure, while a discontinuous displacement field is considered at the locations where cracks form. In discrete models the structure is considered composed of discrete elements. Continuum and discrete models adopt *strain* and *displacement*, respectively, as internal variables.

The adopted level of observation defines the model as heterogeneous or homogeneous. Three levels of observation are usually considered for modelling concrete: the micro-level, where the scale of observation is in the order of $< 10^0$ mm; the meso-level, where the scale of observation is in the order of $10^0 - 10^2$ mm; the macro-level, where the scale of observation is in the order of $10^2 - 10^6$ mm. At the micro-level, products of hydration of cement grains are recognizable. This level of observation is usually considered in models that study hardening of concrete. At the meso-level of observation, concrete is schematized as a three-phase material. The three phases are: aggregates; matrix, namely the mix of cement paste with the finest sand portions; interfacial transition zone (*ITZ*), namely the $30 \div 50$ $\mu$m thick layer of weak cement paste which surrounds the aggregates. This level of observation is adopted in the beam lattice model. The *numerical concrete* proposed by Roelfstra et al. [74] is by all means a pioneer among the meso-scale models of concrete. More often the adopted level of observation is the macro-level, where concrete is regarded as a homogeneous material, whose behaviour can be described by means of a material constitutive relation between local stresses and strains. An increasing interest is nowadays addressed to the *multi-scale* approach. The key idea in the multi-scale

approach is to derive the behaviour of the material at the macro-level, once it is known how the material behaves at the meso-level. The multi-scale approach requires the definition of a *Representative Volume Element* (RVE), which can be viewed as the smallest volume of material whose properties are representative for the whole structure. The existence of a RVE in concrete is questionable because cracking is a localised phenomenon, which implies a displacement jump (or zone of localized strains).

## 1.3.1   Continuum type models

Cracking is a localized phenomenon which implies a discontinuous displacement field. On the contrary, continuum models consider cracks in an averaged, smeared sense. At this manner continuum mechanics theory is preserved and the displacement field remains continuous and differentiable.
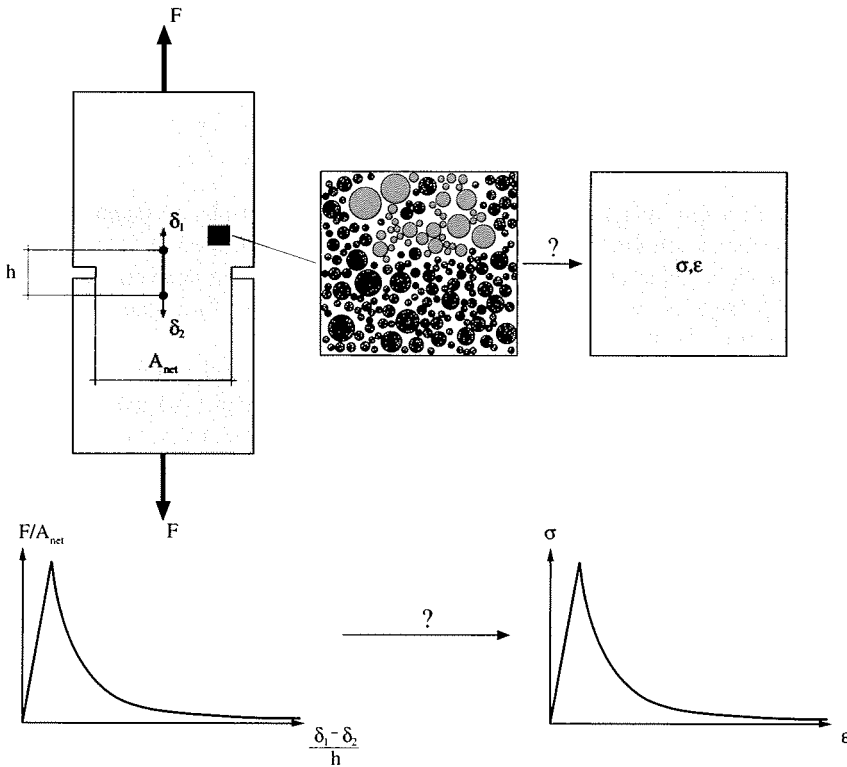


Figure 1.2: Definition of softening properties from a laboratory experiment: example of a uni-axial tensile test.

Homogeneous and continuum models are based on the concept of *softening*. Softening is characteristic of *quasi-brittle* materials, such as concrete and rocks, which undergo in-

creasing deformations under decreasing loads, after the maximum load has been reached. In continuum models, the concept of softening is applied locally, at the material level. In addition to the elastic properties of the material and the strength, softening entails *fracture energy* of the material. The softening parameters are determined from laboratory experiments on specimens of finite size, under specific boundary and loading conditions. The local response of the material is extrapolated from the global response of the structure. However, the response of the structure includes also other effects such as: effect of boundaries; effect of eccentricities in the stress field; effect of pre-existing cracks; effect of instabilities in the laboratory experiment. As a result, the material properties depend, as a matter of fact, on the properties of the structure [97]. The consequence is the well-known phenomenon of *size-dependence*, namely the dependence of material strength and fracture energy on the size of the structure. Figure 1.2 summarizes the homogeneous continuum approach by means of an example. A double-notched specimen is subjected to uni-axial tension. During the test the load $F$ and the elongation of the LVDT, $\delta_1 - \delta_2$, are recorded. The tensile stress and the strain are derived from the measured load and LVDT elongation, after dividing these quantities by the area of the cross section and the length of the LVDT, respectively.

**Piece-wise continuum models**

Linear elastic fracture mechanics (LEFM), which considers cracks propagating from the tip of a pre-existing stress-free crack, is one of the models that consider a discontinuous displacement field. The criterion for crack propagation can be derived using a stress formulation [110] or an energy based formulation [36]. The two formulations are related, as derived by Irwin in 1957 [46].

In more recent times, LEFM has been applied to heterogeneous models for predicting crack propagation in concrete [53, 26]. In these models the micro-structure of concrete is represented as inclusions embedded in a matrix, and micro-cracks are inserted between the inclusions and the matrix. Both the inclusions and the matrix are considered linear elastic and crack propagation is controlled by LEFM fracture criteria.

The stress field predicted by LEFM presents a singularity at the crack tip. In reality, inelastic deformations occur at the crack tip, which are due to plastic deformations in ductile materials such as metals, and to micro-cracking in quasi-brittle materials. In the case of quasi-brittle materials, the zone ahead of the crack tip is named *fracture process zone* (FPZ). In order to solve the stress singularity at the crack tip, Dugdale [30] and Barenblatt [5] introduced a cohesive model for metals, where the crack and the plastic zone are replaced by a fictitious crack, and cohesive forces are applied to impose smooth closure of the crack. Similar to the model of Dugdale and Barenblatt, Hillerborg et al. [42] proposed the *Fictitious Crack Model* (FCM) for quasi-brittle materials. In the FCM the width of the FPZ is negligible and the crack is localized in a line. For this reason this model must be considered as a *discrete crack model*. The cohesive stresses are function of the crack opening, as elucidated in Figure 1.3. The FCM is a three-parameters model: the material behaviour is defined by the tensile strength $f_t$, by the ultimate crack opening and by the shape of the softening curve (or by the fracture energy $G_f$).
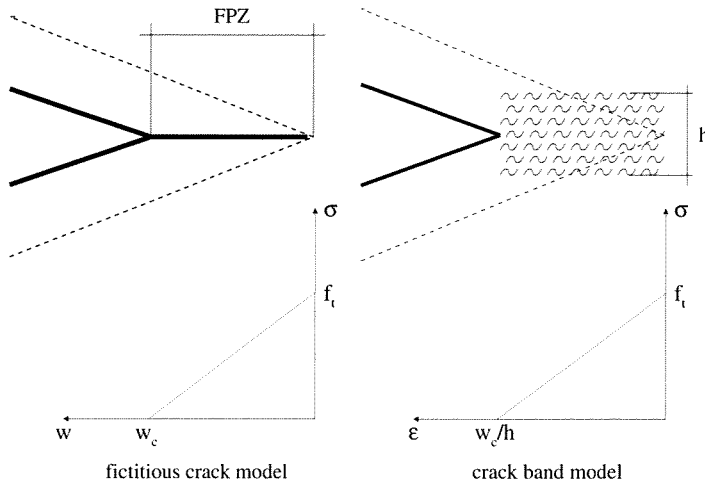
Figure 1.3: Scheme adopted to model the crack in the fictitious and in the crack band models.

In the finite element approach, the discontinuous displacement field between adjacent continuum elements is usually introduced by means of contact or interface elements. An example of a model using contact elements is the model proposed by Rossi and Richer [75]. In the model of Rossi and Richer random material properties are assigned both to the solid and the contact elements, and an elastic perfectly brittle behaviour is assumed for the material constitutive law. Caballero et al. [20] have proposed a model were interface elements are used instead. In this model the larger aggregate pieces are represented by polyhedra embedded in a matrix phase. Both the aggregates and the matrix are considered linear elastic, while failure can be achieved by means of zero-thickness interface elements with a non-linear fracture-based law. The interface elements are inserted between all particle-matrix interfaces and also along selected matrix-matrix inter-element boundaries. A disadvantage of this type of models is that cracks are aligned with inter-element lines. A model which includes a discontinuous displacement field without the disadvantage of crack alignment with inter-elements lines is the *Strong Discontinuity Approach* (SDA) [87]. In the SDA the displacement jumps are embedded in the finite element displacement field. An alternative manner to embed discontinuity in the displacement field is given by the extended finite element method, based on nodal enrichment and the partition of unity concept. The latter, however, requires more implementation effort in comparison with the embedded discontinuities method. An extensive comparison of the two methods can be found in [109].

## Continuum models

Alternative to the FCM is the *Crack Band Model* (CBM) proposed by Bažant and Oh [12]. The CBM is a continuum model where the crack is smeared over a band with height

*h*, whose size depends on the characteristic size of the micro-structure. For this reason, the model is also called *smeared crack model*. In the CBM the softening curve is defined in terms of an equivalent strain, which is related to the crack opening according to $w = \varepsilon h$ (see Figure 1.3). When classical continuum models are used in combination with the Finite Element Method, they exhibit mesh sensitivity: the dissipated energy decreases with a decrease in size of the finite elements, which causes crack localization in a band of width zero in the extreme case of elements with vanishing size. Spurious mesh sensitivity is solved in the finite element implementation of the CBM by adjusting the slope of the $\sigma - \varepsilon$ curve with the finite element size.

Progressive deterioration of the material which causes formation of macro-cracks is described in the *damage models* by means of the *damage* variable, $D$ ($0 \leq D \leq 1$). In the classical formulation of damage models (*local* models) the state variables are defined locally. Also *local* damage models suffer of mesh sensitivity when the FEM is applied. To prevent mesh dependence, solutions based on the introduction of the *characteristic length of the material* have been proposed [8, 12, 54]. The techniques for overcoming localization of damage in vanishing volumes are based on *non-local* and *gradient* approaches. In the *non-local* approach the stress at a certain point depends not only on the strain at that point but also on the neighbouring strain field [69]. In the *gradient* damage approach, which can be regarded as a variant of the non-local approach, higher-order deformation gradients are added in the constitutive model [28, 67]. Gradient damage models require additional boundary conditions whose physical meaning is not always well understood.

Other models that do not present mesh sensitivity include strain rate dependency [64, 88]. Another high gradient model, where localization during fracture is limited by the activation of rotational degrees of freedom, is the Cosserat continuum. It should be remarked here that the beam lattice is a discretization of the Cosserat continuum.

One of the aspects related with concrete and concrete fracture is the anisotropic behaviour of the material. This aspect is often neglected in continuum models, or, at least, approached in a *simplified* manner. For example, damage models are often formulated as isotropic models (scalar damage variable) rather than anisotropic (vectorial damage variable). In other models, the simplifications consist in considering the deterioration of the material only in one direction. This is done, for example, in the fixed and rotating crack models [76]. Another type of approach is followed in the *micro-plane model*, where the complex anisotropic inelastic behaviour of concrete is captured by using constitutive relations between stresses and strains computed as weighted sums on each micro-plane [9]. Another aspect of concrete fracture is tortuosity of cracks, which requires use of remeshing techniques when homogeneous-continuum models are applied [45].

## 1.3.2   Discrete models

*Particle models* are discrete models, which are usually applied to study the behaviour of granular materials such as sand, or rock. This method was first introduced by Cundall and Strack [23] with the name of *Distinct Element Method* (DEM). In the DEM the material is schematized with discrete bodies that interact dynamically. The particles move with finite relative displacements, with the possibility of complete detachment. A recent

version of this model [71] considers rock as a cemented material by introducing a bond between adjacent particles. Progressive damage is represented as broken bonds that form and coalesce in macroscopic fractures. A similar approach was also used by Vonk [105] for studying concrete loaded in tension and compression. In the model of Vonk the aggregates are polygonals connected at the corners with interface elements, which represent the matrix and the ITZ. The interfaces have a linear elastic behaviour until a critical value of stress is reached, and present softening both in tension and shear after failure.

Similar to the beam lattice model: particle models give the possibility to model structural softening without using local softening; particle models can reproduce anisotropic behaviour induced by damage accumulation; particle models do not require remeshing. Additional advantages of particle models are: particle models can simulate both tensile and compressive/shear failure modes; particle models can include increased strength under confinement and crack dilation; particle models can analyze large deformations. Belytschko et al. [14] applied a particle model to model dilatant slip in rock joints. Another application of a particle model is the simulation of fracture in an ice floe during impact with an obstacle (for example, the impact of an ice sheet with an offshore platform). In the work of Jirásek and Bažant [48] the ice floe is modelled with particles that interact only by central forces with a prescribed force-displacement or stress-strain relation that presents softening.

Another discrete type model is the *Rigid Body Spring Model* (RBSM) [50]. In the RBSM the model is divided into polyhedron elements that behave as rigid bodies and whose faces are interconnected with springs. A three-dimensional RBSM model was proposed by Nagai et al. [63]. In the 3D RBSM each rigid body has three transitional and three rotational degrees of freedom at the centre of gravity, and springs simulating transmission of normal or shear forces are placed at the centre of gravity of each face between two adjacent bodies. In the analyses, the normal stresses evolve according to a linear softening, while the shear stresses follow a Mohr-Coulomb like criterion. Like the DEM, this model is able to predict fracture mechanisms in compression. A RBSM approach is also followed in [17], where three rotational springs are considered at the facets, in addition to the three linear springs. Modelling of fracture is based in this case on the crack band model.

### 1.3.3   Lattice models

The discretization of a continuum by means of a lattice was first proposed by Hrennikoff [43], who used the *framework method* to solve problems of elasticity. In the 1970s lattice models were introduced in statistical physics to study fracture of disordered media. Initially the problem was reduced to a scalar problem by using the *electric analogy* where each lattice element is associated to a resistor of unit conductivity. Once the current exceeds a certain threshold in an element, this becomes an insulator. Then the external current is increased and another element breaks. The process is repeated until the network is not any longer conducting. In the 1980s it became clear that the electric analogy was not sufficient to compare theory and experiments, and that it was necessary to consider the vectorial nature of elasticity. Herrmann et al. [41] proposed then the 2D beam lattice. Different types of lattice models differ for the type of elements (trusses or beams), for

the way the heterogeneity is implemented in the model (random distribution of properties or particle overlay), and for the adopted fracture criterion (linear elastic purely brittle or with softening). Plain pin-jointed random network structures of linear elastic brittle trusses were used by Burt and Dougill [19] to simulate uni-axial tests. In the model of Burt and Dougill a range of different strengths and stiffnesses was assigned to the trusses, to demonstrate the effect of changes in heterogeneity on the form of the stress-strain diagram. Schorn and Rode [85] developed a 3D lattice model where linear elastic trusses were arranged in a regular cubic pattern, where each node was connected to all other neighbouring nodes. Stiffness, tensile and compressive strength were assigned to the trusses by a given distribution. Cubic lattice cells including crossing diagonal elements are considered also in the model proposed by Leite, Slowik and Mihashi [27], where heterogeneity is assigned by projecting the lattice onto a computer-generated aggregate-matrix structure. In this approach softening laws have been introduced both for compression and for tension. A particle model is combined with a lattice made of truss elements in the model formulated by Bažant et al. [7]. In the *particle-lattice* model the material is schematized with randomly distributed particles having a given particle size distribution, separated by layers of matrix. The thickness of the matrix layer decides whether two adjacent particles interact or not: if the thickness is smaller than a certain value, the centres of the two particles are connected with a truss element, whose material behaviour is an average of the behaviour of the aggregate and the matrix. In this model the particles are considered elastic while a stress-strain relation with softening is adopted for the matrix. This particle-lattice model has been extended by Cusatis et al. [24, 25] to simulate tri-axial compression. In the extended version of the model, the truss elements have been replaced with elements that transmit both normal and shear stresses, but no bending. The relative displacements of two adjacent particles define the strains in the truss connecting the two particles. The corresponding stresses are calculated using a damage-like constitutive relation, which includes softening for tension, and hardening for compression and shear with high compression.

In the lattice model developed by van Mier and his co-workers, beams are used instead of trusses. The beams were preferred to trusses for two reasons: 1) the beam networks, on the contrary of the truss networks, can simulate a very wide range of Poisson's ratios; 2) the beam networks can simulate the rotation of intact pieces of material linking the crack faces (crack bridging), while the truss networks cannot simulate this phenomenon. Another reason, though of minor relevance, is that truss networks require an additional algorithm in the numerical code for removing those elements that, being disconnected at one end, can rotate freely. According to Schlangen and Garboczi [80], trusses are suitable only for simulating simple crack patterns, while beams are necessary for more complex crack patterns, such as mixed mode cracks. This conclusion was based on results from lattice analyses of shear experiments on double-notched square specimens [65] with homogeneous lattices.

A distinct feature of the Delft lattice model is the direct schematization of the meso-structure of the material, in combination with a linear elastic, purely brittle constitutive law at beam level. As softening is not introduced locally, the model is suitable for giving more insight in the origin of softening. On the contrary, the approach followed in contin-

uum models is more phenomenological, as softening is introduced as intrinsic property of the material. Local softening is also used in many lattice models, in the attempt of matching the experimental results not only from a qualitative but also from a quantitative point of view. Softening is introduced to account for the heterogeneity of phases that are roughly schematized as homogeneous in the model [3]. In this case there is not a clear advantage of using a lattice model rather than a classical continuum model.

Rots and Invernizzi [77] have recently developed a similar approach as the lattice model. The *Saw-Tooth Model* does not pretend of explaining the physics behind fracture mechanisms, but simply to solve numerical instability and divergence in incremental-iterative procedures. In this model the non-linear response is captured via a series of linear steps. The softening stress-strain curve, which is still considered as material characteristic, is replaced by a scaled sequentially linear procedure. Mesh-size objectivity is achieved by adjusting both the peaks and the ultimate strain of the saw-tooth diagram to the size of the finite element, and keeping the fracture energy invariant.

# Chapter 2

# The beam lattice model

In Chapter 1 it has already been mentioned that the *beam lattice model* was originally applied to study fracture of disordered media in the field of statistical physics [41]. Lately, it was applied in the field of fracture mechanics of concrete [81, 79]. In this model, concrete is schematized as a network of Bernoulli beams with different mechanical properties. The disorder of the material can be implemented either by assigning a randomly distributed elastic stiffness and tensile strength to the beams, or overlaying a computer-generated particle distribution on top of the lattice, and assigning different properties to the beams that fall in each of the three phases: aggregate, matrix, and interfacial transizion zone (ITZ, also referred to as *bond* in this thesis). In the sequel of this thesis, only the latter version will be used. Finally, fracture is simulated by sequential removal from the mesh of the elements that have exceeded the critical stress.

In this chapter, the beam lattice model is outlined with emphasis on the construction of the mesh, the implementation of heterogeneities, and simulation of fracture.

## 2.1   Construction of the lattice

In this thesis both regular and random lattices are considered. In the 2D regular lattice the beams have all the same length and form a network of equilateral triangles. An example of a regular lattice is given in Figure 2.1(a). In random lattices the lengths of the beams are randomly distributed. The lattices considered in this thesis are, as a matter of fact, *conditionally-random*. Examples of random lattices with a different *randomness* are given in Figure 2.1(b), (c), (d). The concept of *randomness* will be clarified in the following.

For constructing the *random* lattice, first the nodes are randomly positioned inside a sub-cell of size $A$ in a regular grid with cell size $s$, see Figure 2.2(a). The ratio $A/s$ is defined as *randomness* of the lattice. Then, the nodes are connected using the Voronoi/Delaunay construction [62]. Figure 2.2(b), (c) show how the connectivity between a node and its *potential neighbours* is generated in a 2D lattice with $A/s=1$, for example. The node is connected to two other nodes when the circumference to which these nodes belong

does not encircle other nodes of the mesh. In Figure 2.2(c) the solid lines indicate that the connectivity is generated, and the dashed lines indicate that the connectivity is not generated. In [62] it was investigated how the probability of connectivity varies with the number of *potential neighbours*, and it was found that the *potential neighbours* with the highest probability of connectivity are the 36 nodes in the 6x6 cluster around a site, as shown by the grey area in Figure 2.2(b).



(a)                    (b)                    (c)                    (d)
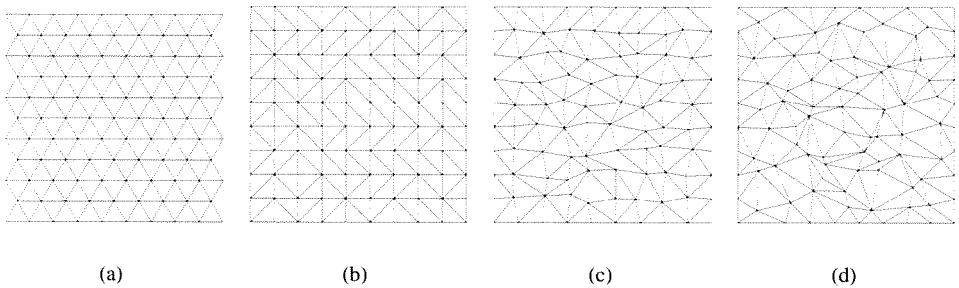
Figure 2.1: Example of 2D regular and random lattices: (a) regular lattice; (b) 0.001 randomness; (c) 0.50 randomness; (d) 1.00 randomness.



(a)                                    (b)                                    (c)
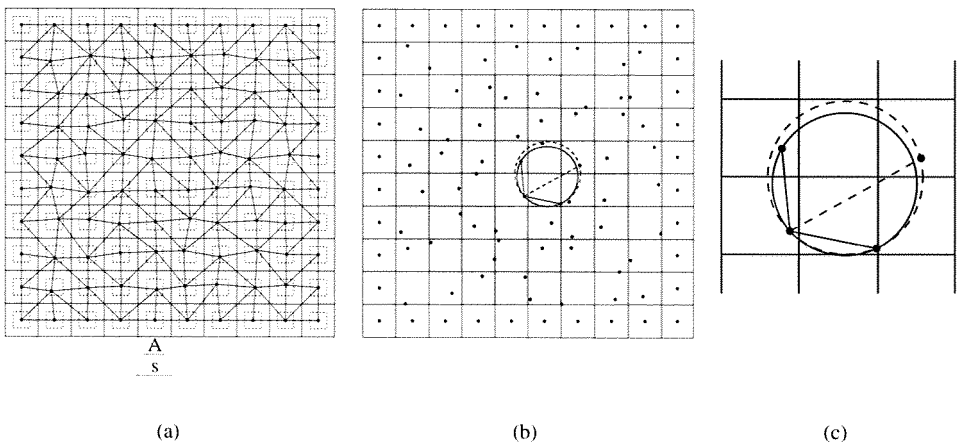
Figure 2.2: Construction of a random lattice: (a) positioning of the nodes in a lattice with $A/s = 0.50$; (b), (c) check for connectivity in a lattice with $A/s = 1.00$.

In analogy to the 2D lattices, in 3D lattices the connectivity is searched among 178 po-

tential neighbours. In this case the connectivity is generated among one node and three neighbours when the four nodes belong to a sphere which does not contain other nodes of the mesh. The Voronoi/Delaunay construction prevents generation of overlapping or crossing beams. For a randomness equal to zero, the nodes would coincide with the centres of the cells and it would not be possible to generate diagonal elements. This can be avoided simply considering a small value of the randomness, for example $A/s = 0.001$. Despite the very small value, still some degree of randomness is achieved by the different orientation of the diagonal beams, as shown in Figure 2.1(b).

In random lattices the disorder of the material is already mimicked at geometrical level, as the beams have different lengths, and therefore also different stiffness. At the very beginning in the development of the beam lattice model, random lattices were introduced to compensate the poor schematization of the material texture. In case of regular lattices the particles, which work as crack arrestors, cause the tortuosity of the crack pattern. However, if the particle distribution is too sparse, cracks run straight through the depth of the specimen, and cause brittleness of the lattice response. In the following chapters it will be shown that more tortuous cracks can be found when denser particle distributions are used. In this case it is not necessary to use random lattices. Furthermore, when random lattices are used, it becomes difficult to isolate the effect of the *geometrical* disorder from the effect of the single phases of the material and their interaction on the overall lattice response. For this reason, with the only exception of the Brazilian test analysis (see Appendix A) only 2D regular lattices will be considered in the next chapters. In analogy with 2D regular lattices, in a 3D regular lattice the beams form a network of tetrahedra. A disadvantage of regular lattices in comparison with random lattices is that elements are preferentially oriented. Preferential orientation of the lattice beams can affect the crack pattern [80]. Mesh bias can be prevented when sufficiently fine meshes and sufficiently dense (realistic) particle distributions are included in the model. For computational reasons, the 3D meshes considered in this thesis are still relatively coarse in comparison with the 2D meshes ($l_{beam}$=0.25 mm in the 2D configuration, against $l_{beam}$=0.75 mm in the 3D configuration). In this case a 3D regular lattice configuration presents *holes* in a direction, which depends on the orientation of the lattice. In a random configuration, on the contrary, beams are oriented in all directions. For this reason only 3D random networks will be considered in this thesis. However, the effect of the random geometry on the overall response of the lattice will be reduced as much as possible by considering the smallest possible randomness ($A/s$=0.001 is the value of randomness adopted throughout this thesis).

## 2.2   Implementation of the heterogeneity

After constructing the mesh, the next step is to assign different mechanical properties to the beams. This is done by overlaying the lattice on top of a computer-generated particle distribution, see Figure 2.3(a), and identifying different material phases, see Figure 2.3(b):

- the aggregate beams are those that fall completely inside the particles;

- the matrix beams are those that fall completely outside the particles;

- the bond beams, which represent the interfacial transition zone, are those with one node falling inside a particle and the second node outside.



(a)                                                                (b)
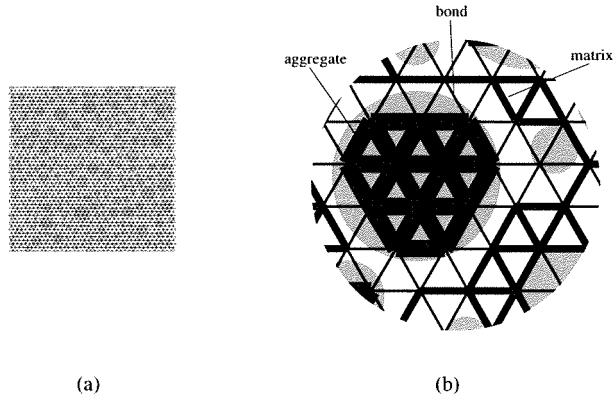
Figure 2.3: Implementation of the heterogeneity: (a) overlay of the lattice on top of a particle distribution; (b) identification of the different phases.

Next, different mechanical properties are assigned to the different phases. Commonly used ratios of the Young's moduli and tensile strengths in lattice analyses [79, 103, 101] have also been adopted in this thesis: $E_a/E_m$=70000/25000, $E_m/E_b$=25000/25000, $f_{t,a}/f_{t,m}$=10/5, and $f_{t,m}/f_{t,b}$=5/1.25 (the indices $a$, $m$, $b$ refer to aggregate, matrix and bond, respectively). Figure 2.3(b) shows that the accuracy in the representation of the particles depends on the adopted length for the lattice beams. The minimum requirement, for guaranteeing that at least one beam falls inside a particle, should be $l_{beam} \leq 1/3 \cdot d_{a,min}$. However, when small particles are present, the fulfilment of this requirement implies an enormous increase in computational effort. Therefore, for sake of computational time, rather coarse lattices are used and the smallest fractions of the particle distributions are in this manner automatically discarded. In this case bond elements can form clusters in the mesh (an example is shown also in Figure 2.3(b)), and affect the crack process. Neglecting the small particles is, among others, a cause of the decrease of the particle density with respect to the input value. Another cause is that part of the volume of the particle falls inside the bond phase, which is much thicker in the numerical model than in the real material. Finally, also the procedure adopted to generate the particles limits the particle density which can be obtained numerically. This *random-placement* procedure consists in placing the particles at a random location in a volume, starting from the fractions with the largest size, in a way that a prescribed minimum mutual distance is respected. The consequence is that placement of the smallest fractions becomes more and more difficult as the particle density increases. The procedure for generating the particle distribution
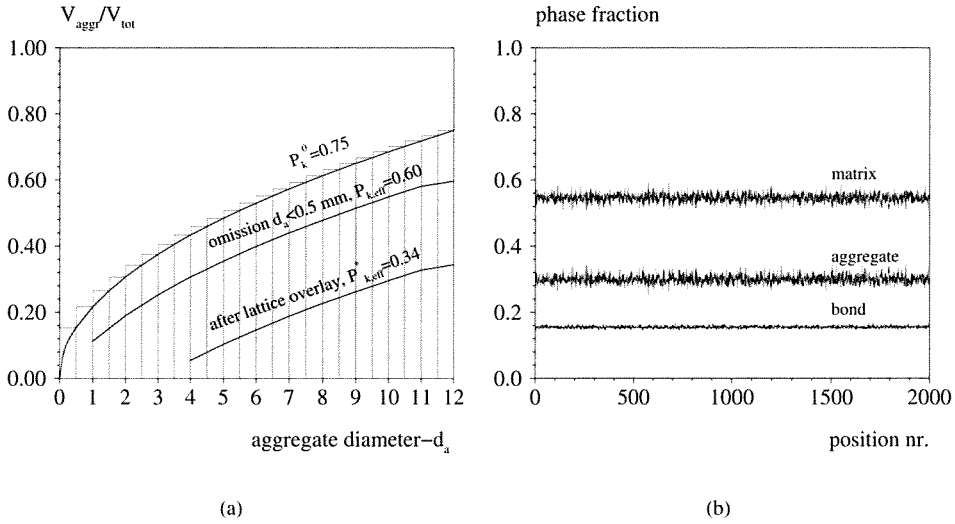
Figure 2.4: (a) Grading curves and (b) phase fractions after overlay of the particle distribution on top of the lattice.

will be outlined in the following, with reference to a 3D example with maximum grain size $d_{a,max}=12$ mm and volumetric density $P_k^0=0.75$. The same particle distribution will be used for the analyses reported in Chapter 4. The grading curve adopted as basis for the computer-generated aggregate structure is a Fuller curve, where the number of particles with diameter $d_{i-1} \leq d_a \leq d_i$ is obtained following

$$P_k^0 \cdot (\sqrt{d_i/d_{a,max}} - \sqrt{d_{i-1}/d_{a,max}}) \cdot V_{tot}$$

$V_{tot}$ is the volume to be filled (in this example $V_{tot} = 72 \cdot 72 \cdot 72$ mm$^3$). The Fuller curve is discretized by dividing the range 0 mm$\leq d_a \leq 12$ mm of diameters into intervals of 0.5 mm, as shown in Figure 2.4(a). As an approximation, all grains falling in one interval of the distribution are considered to have the same diameter, namely, the integer value of the interval. In this manner the grains falling in the interval 0 mm$\leq d_a \leq 0.5$ mm are neglected and the resulting particle density decreases to $P_{k,eff} = 0.60$. Next, the grains are positioned randomly inside the volume $V_{tot}$. Starting from the biggest diameter, the particles are placed at a minimum mutual distance of $1.1 \cdot (d_{a,i} + d_{a,j})/2$. The condition of minimum mutual distance cannot easily be satisfied during positioning the smallest particles, and require in this case a long computer time for generating the particle distribution. For this reason the smallest particles are neglected. Finally, another fraction of small particles is not taken into account as consequence of the coarseness of the mesh. The result is that only the particles with $d_a \geq 4$ mm are left of the initial particle distribution, and the particle density decreases to the value $P_{k,eff}^* = 0.34$. In Figure 2.4(a) it

is shown how the grading curve varies at the different stages. Finally, the actual density will be computed as ratio between the number of aggregate beams and the total number of beams, $P_{k,latt} < P^*_{k,eff}$. Figure 2.4(b) shows how the fractions of the three phases (aggregate, matrix and bond) vary when the position of the lattice inside the volume occupied by particle distribution varies randomly.

In the 2D case, the cumulative distribution function derived by Walraven [106] is used as basis for the generation of the aggregates. This curve is based on a Fuller curve and gives the probability $P_c$ that a point on an intersection plane with the volume containing the particle distribution is located in an intersection circle with diameter $d < d_0$

$$P_c(d < d_0) = P^0_k \cdot \{1.065(d_0/d_{a,max})^{0.5} - 0.053(d_0/d_{a,max})^4 - 0.012(d_0/d_{a,max})^6$$

$$-0.0045(d_0/d_{a,max})^8 - 0.0025(d_0/d_{a,max})^{10}\}$$

In Chapter 4 also denser particle distributions will be considered. These particle distributions are obtained by contracting the original volume containing the particles and applying dynamic impact models [90].

## 2.3   Fracture simulation

In the lattice model, fracture is simulated by sequential removal of beams from the lattice mesh. At each step only the beam with the maximum ratio between the critical stress, which is calculated according to the adopted fracture criterion, and its tensile strength, $\sigma^*_i/f_{t,i}$, is removed. The basic assumption is that the material behaves linearly elastic at the beam level. The sequence in a lattice analysis is as follows:

- a load (force $F_0$ or displacement $\delta_0$) is applied to the structure;

- a linear elastic analysis is performed and the beam $i$ with max $\sigma^*_i/f_{t,i}$ is removed from the mesh;

- displacements and forces are then scaled by the factor $f_{t,i}/\sigma^*_i$ in order to achieve the condition that in all beams $\sigma^*_i/f_{t,i} < 1$;

- the same load as in the previous step is applied and the next critical beam is removed from the mesh.

At each step the load is applied on the specimen, whose stiffness matrix is adjusted after removal of the beam which fails in the previous step (*secant method*). The value of the load (or displacement) which causes failure of the beam depends on the stress distribution after the previous step. For this reason, the load-displacement diagram from a lattice analysis presents a characteristic zigzagging, see Figure 2.5(a). This type of diagram resembles quite well diagrams recorded during laboratory experiments, where load drops are caused by local instabilities occurring during crack formation and propagation [100]. In experiments, however, stable crack propagation can be obtained when a specific control method is adopted for conducting the experiment. Still, local instabilities may occur but

load−F                              load−F



displacement−δ                      displacement−δ

(a)                                 (b)
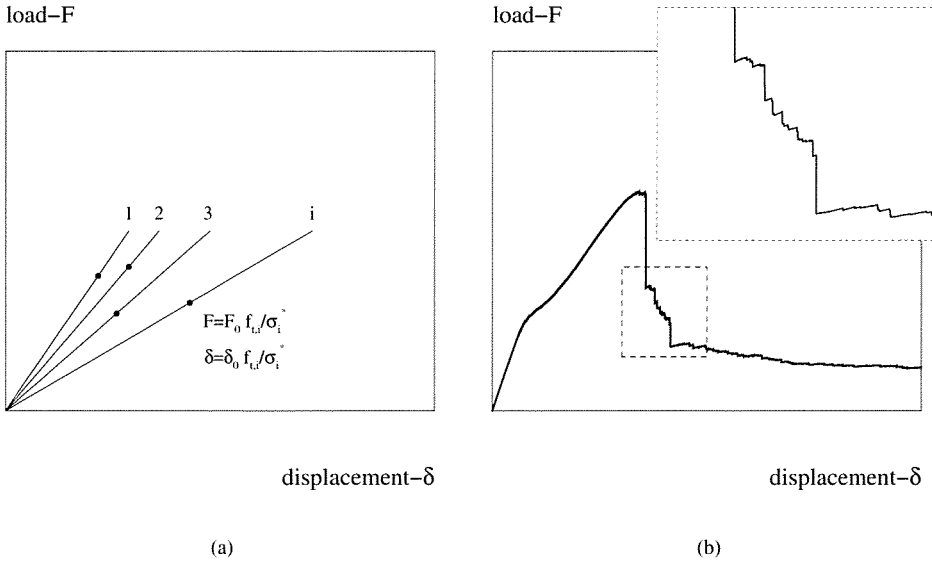
Figure 2.5: (a) Construction of the load-displacement diagram from a lattice analysis and (b) smoothening procedure.

they give rise only to small load drops. The zigzag in the lattice load-displacement diagrams is usually hidden by applying a smoothening technique as shown in Figure 2.5(b). Smoothening is quite helpful for comparing different diagrams. The inconvenience of this procedure is that information about possible snap-back is lost and the amount of dissipated energy is overestimated.

It has already been outlined that the fracture process is mimicked in the lattice by removing elements from the mesh. This limits the capability of the model to reproduce for example irreversible deformations due to geometrical mismatch of the crack faces during cyclic loading [29]. A way for including permanent deformations in the lattice model is to use a phenomenological approach like in [98].

## 2.3.1 Fracture criterion

The fracture criterion adopted in the lattice model considers as critical stress $\sigma^*$ the tensile stress calculated according to

$$\sigma^* = \frac{N}{S} + \alpha \cdot \frac{\sqrt{M_x^2 + M_y^2}}{W} \tag{2.1}$$

where $S$ and $W$ are the area and the section modulus of the cross section of the beam, and $N$, $M_x$ and $M_y$ are the internal axial force and bending moments. The coefficient $\alpha$ is used

to adjust the contribution of the bending moment. According to this fracture criterion, only mode I fracture occurs locally, while the strength in compression is infinite, see Figure 2.6(a). In this case failure occurs when the critical stress in the beam has reached the tensile strength $f_{t,i}$.

Some attempts have also been made to include failure in compression and shear in the fracture criterion. For example, in [102] the fracture criterion was based on a Mohr-Coulomb criterion earlier proposed by [16]. This fracture criterion gave a good prediction of the bi-axial failure contours for concrete, though hardly any difference was observed when it was applied to uni-axial tensile tests.

The Mohr-Coulomb criterion, see Figure 2.6(b), was applied also in the analysis of the Brazilian test (see Appendix A). In this case the beam that fails is the one with the maximum value of $(\tau^* - \sigma^* tg\phi)/c$, where $\phi$ and $c$ are the friction angle and cohesion of concrete, respectively. The critical value of shear stress was computed as ratio between internal shear force and area of the cross section of the beam, $\tau^* = Q/S$.

Other fracture criteria could be introduced in order to take failure in compression into account. Nevertheless, the fracture criterion alone is not sufficient to reproduce failure in compression because the model, in its actual formulation, cannot represent phenomena such as contact and friction between the crack surfaces.



(a)                                                                                    (b)
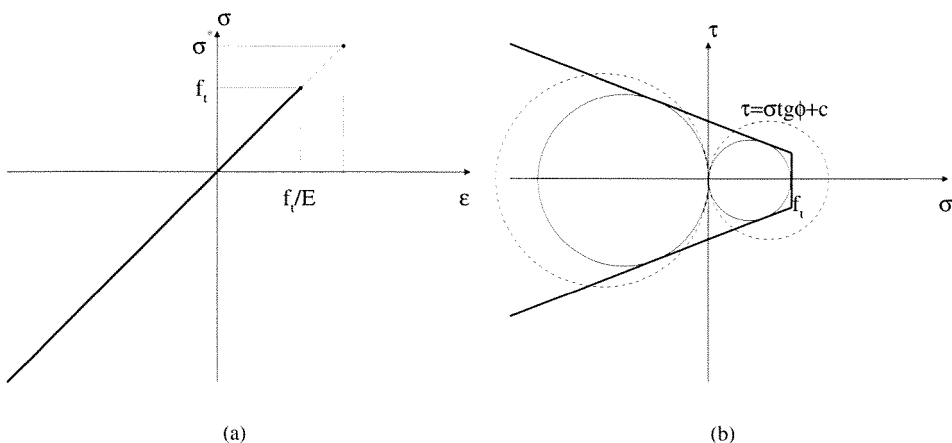
Figure 2.6: (a) Standard and (b) Mohr-Coulomb type fracture criteria.

One of the criticisms against the lattice model is the brittleness of its response. The fracture criterion, which assumes a local brittle behaviour, has been mentioned as the major responsible factor for the brittle lattice response. The solution proposed by some researchers is to introduce softening at the beam level [3]. It is necessary to mention once again that it is a unique feature of the lattice model that structural softening is represented, while the local behaviour is purely brittle.

## Influence of parameter $\alpha$

In 2D lattice analyses the commonly used value for the coefficient scaling the bending moment is $\alpha = 0.005$. In [79] it was shown that $\alpha$ affects the tail in the stress-deformation curve: a small $\alpha$ gives a long tail, while a large $\alpha$ results in a more brittle global behaviour. Nevertheless, if $\alpha$ is taken too small, than the predicted fracture process shows *peeling effects* [94]. This was shown by simulations with a rectangular beam lattice where $\alpha = 0$. For understanding the influence of $\alpha$ on 3D lattice analyses, one of the analysis reported in Chapter 4 (uni-axial tensile test of a cube) has been conducted using different values of $\alpha$ (=0, 0.005, 0.025, 0.05, 0.5). The results from these analyses are summarized in Figure 2.7 and Figure 2.8.



(a)                                         (b)
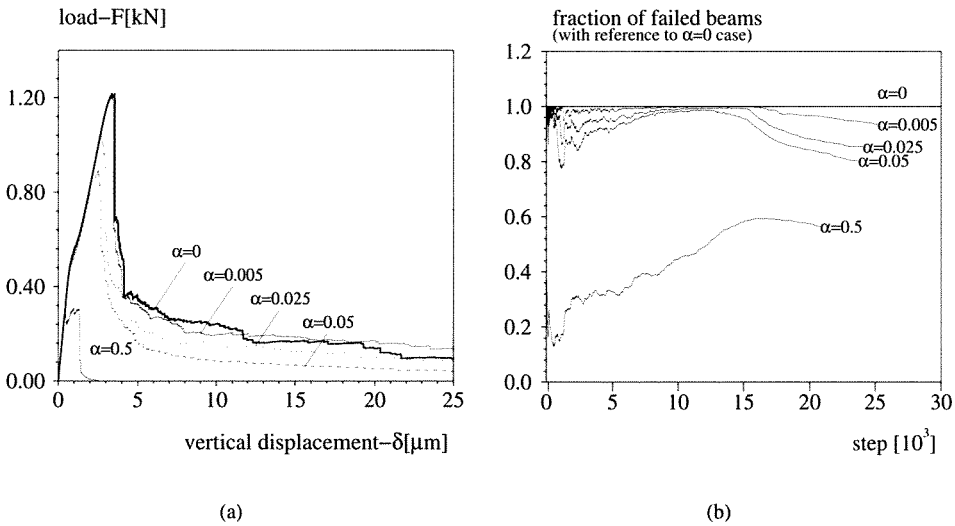
Figure 2.7: Influence of parameter $\alpha$: (a) load-displacement diagrams; (b) fraction of beams failing in the analyses with $\alpha \neq 0$, referred to the number of beams failing in the analysis with $\alpha = 0$.

In Figure 2.7(a) the load-displacement diagram up to a maximum displacement of $\delta = 25 \ \mu m$ is represented as function of $\alpha$. In Figure 2.7(b), the fraction of beams failing in each analysis with different value of $\alpha$ is compared to the analysis with $\alpha = 0$. If exactly the same beams fail, and in the same sequence, then this fraction would be 1 at any step. This diagram can be quite helpful to understand the different process of crack formation in the different specimens, especially at loading stages when only micro-cracks are present. In this case the differences between the crack patterns are in fact not clearly

visible, especially in a 3D specimen. Finally, Figure 2.8 represents the crack patterns in the specimen, which is cut into sections normal to the Z-axis of the reference system.
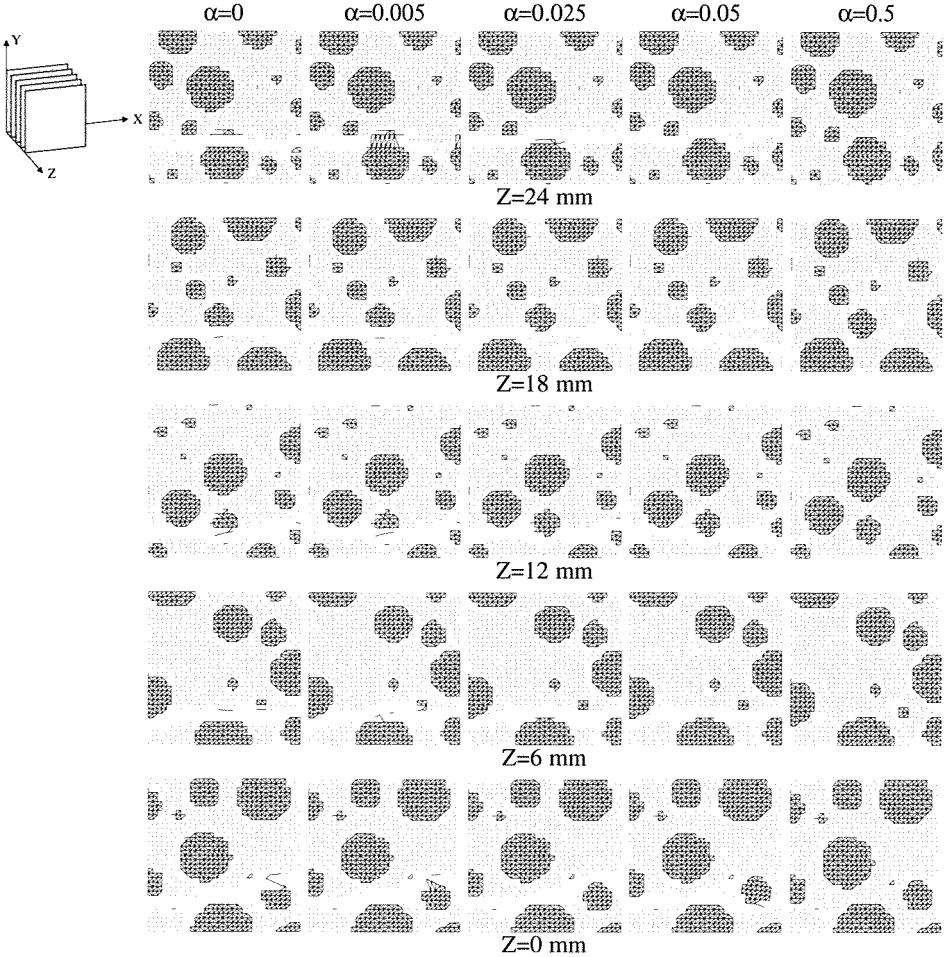


Figure 2.8: Influence of parameter $\alpha$: crack pattern at $\delta = 25$ $\mu$m for different values of $\alpha$.

The results obtained show that, though the value of the peak load is affected by the value of $\alpha$, the shape of the load-displacement diagrams and the final crack patterns do not change when $\alpha$ varies in the range $0 \div 0.05$. This is also confirmed by the diagram in Figure 2.7(b), which shows that for these values of $\alpha$ the beams removed are for more than 80% the same as those removed in the analysis with $\alpha = 0$ during the whole numerical experiment. However, for $\alpha = 0.5$ a completely different response of the specimen in terms of load-displacement diagram is obtained. Also the process of crack formation

proceeds differently, as the fraction of failed beams in common with the specimen with $\alpha = 0$ remains always much lower than 60%, and eventually approaches this value only in the tail of the softening branch. As a matter of fact, the final crack is located approximately at the same position in the specimen, but the crack opening is much smaller (all crack patterns in Figure 2.8 are obtained amplifying the displacements by a factor 60) and the crack deviates from the straight pattern upwards at the right side of the specimen.

As there is no essential difference in the results with $\alpha = 0.005$ and $\alpha = 0$, the latter value has been adopted in all 3D analysis that will be reported in Chapter 4.

# Chapter 3

# Elastic behaviour of the beam lattice

The aim of the beam lattice is to mimic the behaviour of concrete when it is still linear elastic, up to micro-cracking, propagation of macro-cracks and, finally, failure.

The geometrical properties alone of the beams define the overall elastic response of a homogeneous lattice. A lattice is intended to be homogeneous when all elements have the same Young's modulus. However, when particles are embedded, also the distribution and stiffness of the particles contribute to define the effective Young's modulus and Poisson's ratio of the lattice, $E^*$ and $\nu^*$.

The influence of the beam geometry and of the embedded particles on the elastic behaviour of a 3D beam lattice is the subject of this chapter.

## 3.1  2D beam lattice

Already in the early 1940s a framework method was proposed to solve problems of elasticity [43]. The basic idea of this method consists in replacing the continuum with a framework of bars, arranged according to a definite pattern, whose elements are endowed with elastic properties suitable to the specific type of problem. In a two-dimensional stress situation, for example, the framework is plane and composed of bars offering elastic resistance to change in length (trusses). Considering a framework of equilateral triangles, Hrennikoff found that the only value of Poisson's ratio for such a pattern is $\nu^* = 1/3$, and that the cross section of the bar must follow the relation $S = \sqrt{3}/2 \cdot l \cdot t$, where $l$ is the length of each bar in the framework, and $t$ is the thickness of the cross section. The conclusion is that, though the framework of trusses is suitable to model a material such as steel, it is not for concrete, which has $\nu \approx 0.2$.

When the same pattern (equilateral triangles) is used for a framework of beams, it can be

shown [80] that the expression of the Poisson's ratio is:

$$\nu^* = \frac{1-(\frac{h}{l})^2}{3+(\frac{h}{l})^2} \tag{3.1}$$

where $h$ is the height of the rectangular cross section. Equation 3.1 gives values of $1/3 \geq \nu^* \geq 0$ for $0 \leq h/l \leq 1$, which indicates that frameworks of beams are more suitable than frameworks of trusses for describing the elastic behaviour of concrete. Equation 3.1 was derived analytically by comparing the strain energy of a unit cell of a lattice and an equivalent continuum area, under conditions of boundary periodicity. In a similar fashion the expression of the Young's modulus can be derived:

$$E^* = 2 \cdot \sqrt{3} \cdot \frac{E_{beam} \cdot S}{l} \cdot \frac{1+(\frac{h}{l})^2}{3+(\frac{h}{l})^2} \tag{3.2}$$

where $E_{beam}$ is the Young's modulus of the single beam.



(a)                                        (b)

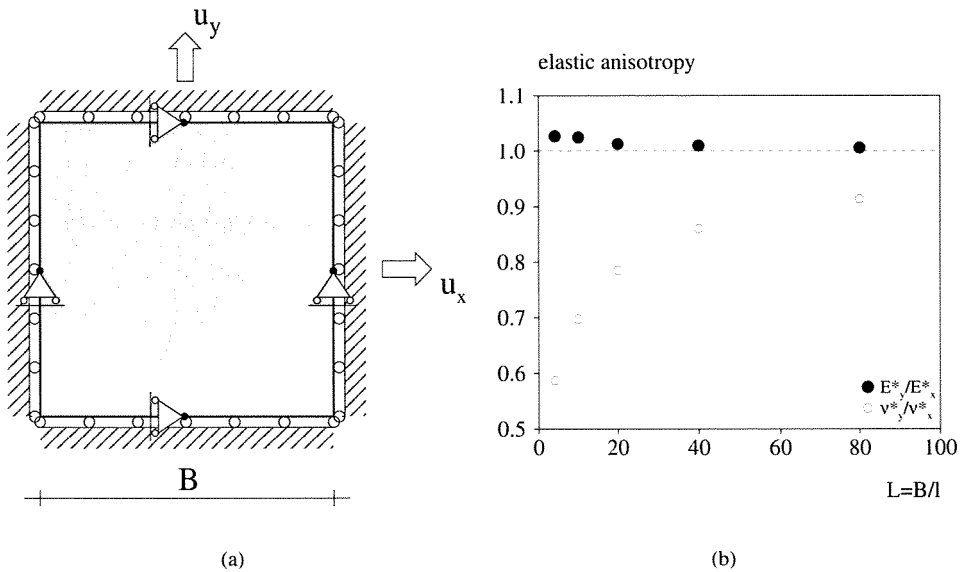Figure 3.1: (a) Model for the computation of elastic properties and (b) elastic anisotropy in a 2D regular lattice, after [101].

The boundary periodicity prevents the boundaries from affecting the determination of the elastic properties. If boundary periodicity is not adopted, the effect of boundaries does affect the elastic behaviour of a lattice of finite size. In order to study this effect,

van Vliet [101] considered 2D triangular regular lattices in the shape of a square with varying width $B$. After a uniform displacement was applied along the direction normal to each side of the lattice (first in $X$ and then in $Y$ direction as indicated in Figure 3.1), forces and displacements at the nodes in the faces where derived and, from these, stresses and strains by means of an averaging procedure. Finally, $E^*$ and $v^*$ were computed from the average stresses and strains. As the behaviour of a lattice of finite size is not isotropic, $E^*$ and $v^*$ have different values in the directions $X$ and $Y$. From a comparison of analytical and numerical results van Vliet concluded that, with respect to the Young's modulus, these agree well and the lattice can be considered almost-isotropic already for $L \geq 20$. With respect to the Poisson's ratio, the lattice not only presents a highly anisotropic behaviour, but also a considerable scatter between the analytical and computational results. The effect of the specimen size on the elastic anisotropy is elucidated in Figure 3.1(b).

The same scheme as in [101] was used previously in [103] to compute the elastic parameters of a random lattice. In [103] a mesh of 50x50 nodes was used to determine $E^*$ and $v^*$, and the randomness was varied between $0.001 \leq A/s \leq 1.0$. The results of this analysis are summarized in Figure 3.2(a) and Figure 3.2(b). As in random lattices the beams have all different lengths, the graphs in Figures 3.2(a) refer to the average beam length, $l_{avg}$. The results of Vervuurt show that $v^*$ not only depends on the geometry of the beam, but also on the randomness of the lattice, and that a 2D regular lattice has nearly the same Poisson's ratio as a 2D random lattice with the highest degree of disorder, $A/s = 1$, see Figure 3.2(a).
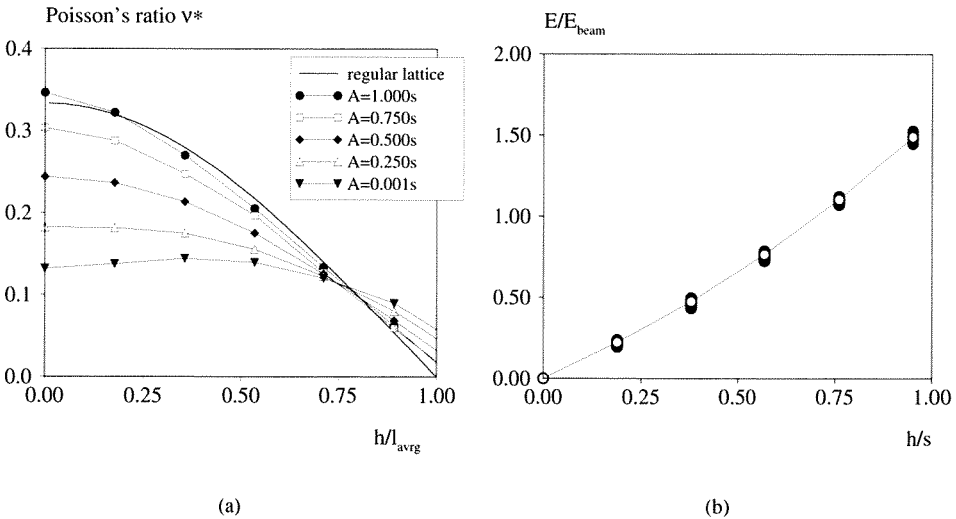


(a)                             (b)

Figure 3.2: (a) Poisson's ratio and (b) Young's modulus in a 2D beam lattice, after [103].

## 3.2   3D beam lattice

In a similar fashion as in the 2D lattice, the effective elastic properties have been computed also for a 3D beam lattice. The specimen was a cube whose size was chosen $B = 30$ mm, in order to limit the computational effort. The effects of the boundaries were analyzed by varying the cell size $s$=1, 1.2, 1.5, 2, 3, 6 mm. Also the influence of the randomness was investigated. For this purpose, meshes with randomness $A/s = 0.001, 0.25, 0.50, 0.75, 1.00$ were generated. Due to the geometrical disorder of the mesh, some scatter can be expected in the results when different meshes are considered. For this reason, for each combination of parameters $s$ and $A/s$, three different meshes were generated. The variation of the average beam length with the cell size $s$ is shown in Figure 3.3 The diameter of the cross section of the beam was maintained constant, $h$=1 mm.
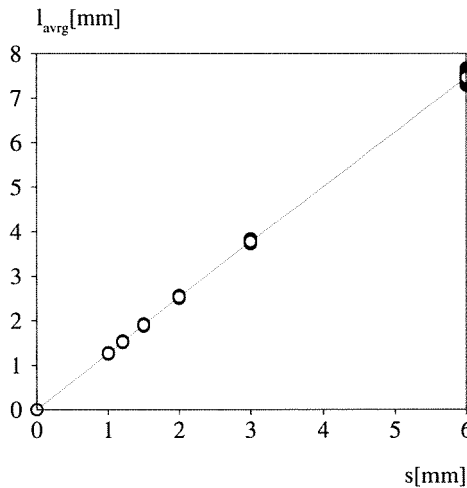


Figure 3.3: Relation between average beam length and cell size in a 3D random lattice.

In order to compute $E^*$ and $v^*$ the same approach as in [101] was followed. The specimen was loaded with a unit displacement at the nodes of a face, in the direction normal to the face. In this manner, three load cases were considered for each mesh, corresponding to uni-axial stress in the directions $X$, $Y$ and $Z$, respectively. For each load case a linear system of equations had to be solved. Despite the size of the specimen, the number of degrees of freedom for this model was relatively high. In the finest mesh considered ($s = 1$), for example, the number of elements was 205169, for 27000 nodes and 162000 degrees of freedom. At the time this analysis was performed, the beam lattice model had not yet been implemented in the code for parallel computing and the standard one-processor workstation which was available required one hour for a run if an iterative solver was used, against sixteen hours if a LDU solver was used.

After each analysis stresses and strains were computed averaging reaction forces and displacements at the nodes of the faces of the cube according to:

$$\sigma_i = \frac{\sum F_i}{B^2}$$
$$\varepsilon_i = \frac{\sum u_i}{B}$$

(3.3)

where $i = X, Y, Z$. Next, the octahedral stresses and strains were computed:

$$\sigma_{oct} = \frac{\sigma_1 + \sigma_2 + \sigma_3}{3}$$
$$\varepsilon_{oct} = \frac{\varepsilon_1 + \varepsilon_2 + \varepsilon_3}{3}$$
$$\tau_{oct} = \frac{1}{3}\sqrt{(\sigma_1 - \sigma_2)^2 + (\sigma_2 - \sigma_3)^2 + (\sigma_3 - \sigma_1)^2}$$
$$\gamma_{oct} = \frac{2}{3}\sqrt{(\varepsilon_1 - \varepsilon_2)^2 + (\varepsilon_2 - \varepsilon_3)^2 + (\varepsilon_3 - \varepsilon_1)^2},$$

(3.4)

and, from Equations 3.4, the bulk modulus $K^*$ and the shear modulus $G^*$ were derived following:

$$K^* = \frac{\sigma_{oct}}{3\varepsilon_{oct}}$$
$$G^* = \frac{\tau_{oct}}{\gamma_{oct}}.$$

(3.5)

Finally, from Equation 3.5 the Young's modulus $E^*$ and Poisson's ratio $\nu^*$ were computed as:

$$E^* = \frac{9K^*G^*}{3K^* + G^*}$$
$$\nu^* = \frac{3K^* - 2G^*}{2G^* + 6K^*}.$$

(3.6)

## 3.2.1 Homogeneous lattice

Due to the anisotropy of the lattice different values of $E^*$ and $\nu^*$ were found when applying the load in different directions. To measure the anisotropy of the lattice, the maximum values of the ratios $E_i/E_x$ and $\nu_i/\nu_x$ ($i = y, z$) have been calculated for each value of randomness. The scattered values corresponding to the three different meshes are drawn in Figure 3.4 as function of $L = B/l_{avg}$.
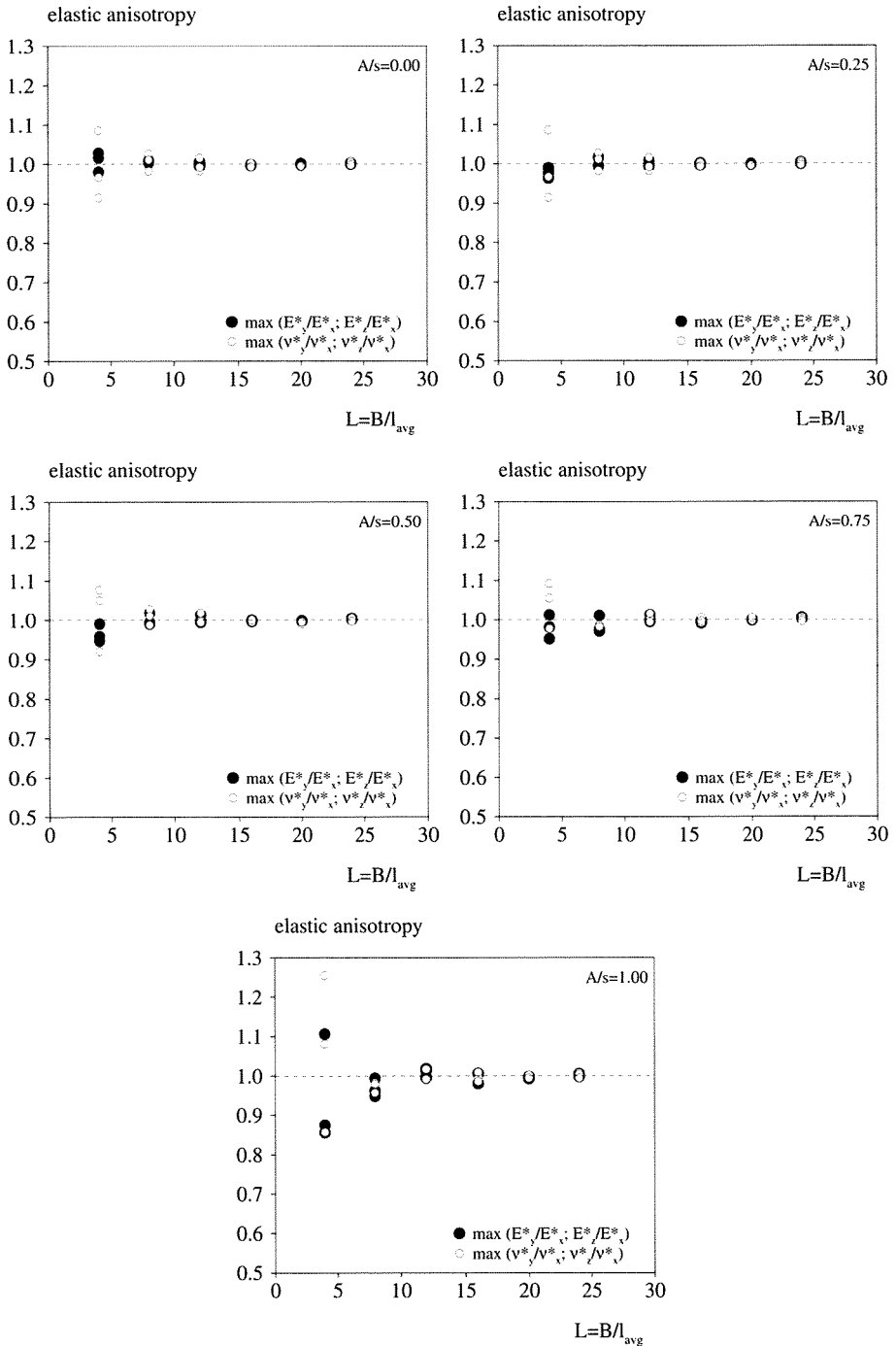
Figure 3.4: Elastic anisotropy in a 3D beam lattice for different values of randomness.

Also the 3D random lattice, as the 2D regular lattice, shows an almost-isotropic behaviour with respect to the Young's modulus, while for the Poisson's ratio directional effects are found. These effects depend on the type of mesh, and disappear if a sufficiently fine mesh is used or, alternatively, a sufficiently large specimen: $L \geq 8$. It is curious and worth to mention here that the same minimum ratio between characteristic size of the specimen and maximum aggregate size $(B/d_{max} = 8)$ is suggested, based on scatter in experiments. The reason for the different anisotropy lies in the adopted averaging procedure. As a matter of fact, the average includes also the effect of the boundaries, to which the transversal displacements are probably more sensitive than the displacements in the direction of the load. Despite the qualitatively similar behaviour, the 3D random lattice shows to be less affected by the boundary effects than the 2D random lattice, as can be derived from comparing the results in Figure 3.1 and Figure 3.4. While in the 3D lattice already for $L = 8$ the variation of Poisson's ratios obtained loading the specimen in different directions is smaller than 5%, in the 2D regular lattice the same variation can be obtained only for $L \geq 80$. It would be interesting to conduct a similar comparison with results from 2D random lattices, to conclude that 3D effects contribute to smoothen the effect of the boundaries already in coarse lattices.

As concerns the randomness, no specific effect is registered on the overall elastic response of the 3D random lattice.

Since the behaviour of the 3D random beam lattice is almost-isotropic, the overall Young's modulus $E^*$ and Poisson's ratio $\nu^*$ have been computed as average of the values corresponding to the three loading directions, $X$, $Y$, and $Z$. Furthermore, due to the small scatter, also the results from the three different meshes have been averaged. In Figure 3.5 the ratios $E^*/E_{beam}$ and $\nu^*$ are presented as functions of $h/l_{avg}$ and $h/s$, respectively. The analyses were conducted only for $0.10 \leq h/l_{avrg} \leq 0.80$ and, from these, the results for $0.00 \leq h/l_{avrg} \leq 0.10$ and $0.80 \leq h/l_{avrg} \leq 1.00$ were extrapolated. For this reason these results are drawn as dashed lines in Figure 3.5(a). The diagrams in Figure 3.5 can be used to define the geometry to be assigned to the 3D lattice, in order to achieve an assigned Young's modulus and Poisson's ratio. The curves in Figure 3.5(a) define the diameter of the cross section of the beam, for an assigned $A/s$ and $s$ ($l_{avg}$ can in turn be derived from the diagram in Figure 3.3). Next, the curves in Figure 3.5(b) define the value of $E_{beam}$.

As in the 2D lattice, $E^*/E_{beam}$ is independent of the randomness of the mesh, while the Poisson's ratio $\nu^*$ is considerably affected by it. For $h/l_{avg} \leq 0.65$, $\nu^*$ increases with the randomness, while decreases when $h/l_{avg} \geq 0.65$. The randomness influences also the type of dependence of $\nu^*$ on $h/l_{avg}$. In the 2D lattice $\nu^*$ decreases monotonically, reaching the maximum value at $h/l_{avg} = 0.00$. Only when $A/s = 0.001$ the maximum is reached at $l_{avg} \approx 0.35$. In the 3D lattice, $\nu^*$ decreases monotically only for $A/s = 1.00$ and for all other values of the randomness it exhibits a maximum at $h/l_{avg} \approx 0.25$. Furthermore, as the randomness decreases, also the range of variation of $\nu^*$ with $h/l_{avg}$ decreases. The type of variation of $\nu^*$ with $h/l_{avg}$ depends on the relative values of the shear, axial, bending and torsional stiffness of the beams, as the first increases more rapidly than the others when $h/l_{avg}$ increases. The effect of the shear stiffness on the Poisson's ratio of a 2D lattice was studied analytically in [91] for a lattice of springs endowed with axial and shear stiffness only, both for a hexagonal and square configuration. For both configurations

it was found that the Poisson's ratio decreases monotonically with increasing the shear stiffness, reaching its maximum at 0.25 when the springs have only axial stiffness. It is not clear if the relative value of the different stiffness contributions, and their distribution among all beams, also affect the dependence of $\nu^*$ on the randomness. By increasing the randomness, the probability to have much shorter and longer beams than the average is increased, as well as the probability that the beams are oriented in all possible directions. Due to the non-linear relation between shear and axial stiffness, the total contribution of *short* beams can result in prevailing contribution of the shear stiffness on the axial stiffness, or vice versa if the contribution of the *long* beams prevail. The first case corresponds to the region $h/l_{avg} \geq 0.65$, where the Poisson's ratio decreases with the randomness. The second case corresponds to the region $h/l_{avg} \leq 0.65$, where the Poisson's ratio increases with the randomness. However, for very small randomness, the probability of very short or long beams decreases, which results in a more gradual variation of $\nu^*$ with $h/l_{avg}$.



(a)                                                          (b)
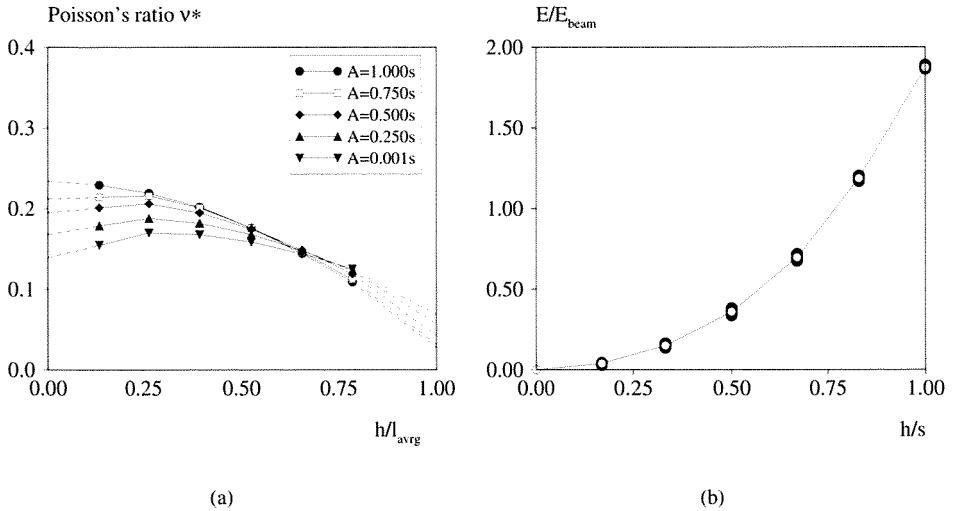
Figure 3.5: (a) Poisson's ratio and (b) Young's modulus in a 3D beam lattice.

Comparison of 2D and 3D results show two major differences. The first difference is that the range of variation of $\nu^*$ with the randomness is larger in the 2D lattice than in the 3D lattice. The maximum variation, at $h/l_{avg} = 0.00$, is $\nu^* = 0.13 \div 0.34$ in the 2D lattice, against $\nu^* = 0.11 \div 0.24$ in the 3D lattice. The second difference is that the 2D and 3D lattice give different upper bounds for $\nu^*$: $1/3$ in the 2D lattice against $1/4$ in the 3D lattice. Notice that the same value, 0.25, was found in [91]. As both models pretend to describe the same continuum, the relation between elastic properties of the continuum and elastic properties of the discrete model should be unique. It should be recalled here that the stress condition considered in the 2D lattice was plane stress. If plane strain

is considered instead of plane stress, the relation between transversal and longitudinal displacements reads as:

$$\frac{u_y}{u_x} = \frac{v^*}{1 - v^*} \tag{3.7}$$

By substituting $u_y/u_x = 1/3$, which was found for the plane stress condition, in Equation 3.7, the value $v^* = 0.25$ can be found. Namely, if plane strain is considered instead of plane stress, the same upper bounds are found for $v^*$ in the 2D and 3D situation. Thus, the plane strain condition should be preferred to the plane stress condition, and all graphs in Figure 3.2(a) should be scaled by the factor $v^*/(1 - v^*)$. As a consequence the same $v^*$ of the equivalent continuum can be obtained using different heights of the beam's cross section, and depending whether plane stress or plane strain has been considered. The different choice of $h$, however, would affect not only the elastic properties but also the fracture behaviour. To illustrate this the fracture analysis of a 3D lattice with height of the beam's cross section $h=1$ mm and $h=0.5$ mm, respectively, is considered. The sample under consideration is a cube of 24 mm size subjected to a vertical displacement applied at the nodes of the upper face, and supported at the bottom face. More details about this analysis will be given in Chapter 4, while now attention is paid only to comparing the different results obtained for different heights of the beams' cross section.

The values of the axial load ($F_{peak}$) and of the vertical displacement ($\delta_{peak}$) at the peak load are summarized in Table 3.1.

| $h$[mm] | $F_{peak}$[kN] | $\delta_{peak}[\mu$ m] |
|---------|----------------|------------------------|
| 1.0     | 1.06           | 3.43                   |
| 0.5     | 0.18           | 4.02                   |

Table 3.1: Results at the peak.

The load-displacement diagrams from the two analyses are shown in Figure 3.6(a). In order to make a comparison, the diagrams are made dimensionless by dividing the load and displacement by the corresponding values at peak. The comparison between the fracture mechanisms is shown in the diagram in Figure 3.6(b). This diagram shows, for each step, the percentage of beams failing in the analysis with $h=0.5$ mm that have also failed in the analysis with $h=1.0$ mm. For example, if at step $i$ the same beams would have failed in both analysis, then the value on the diagram would be 1. Furthermore, if the beams would have also failed in the same sequence, the diagram would be a straight line parallel to the $x$ coordinate axis.

(a)                                                              (b)
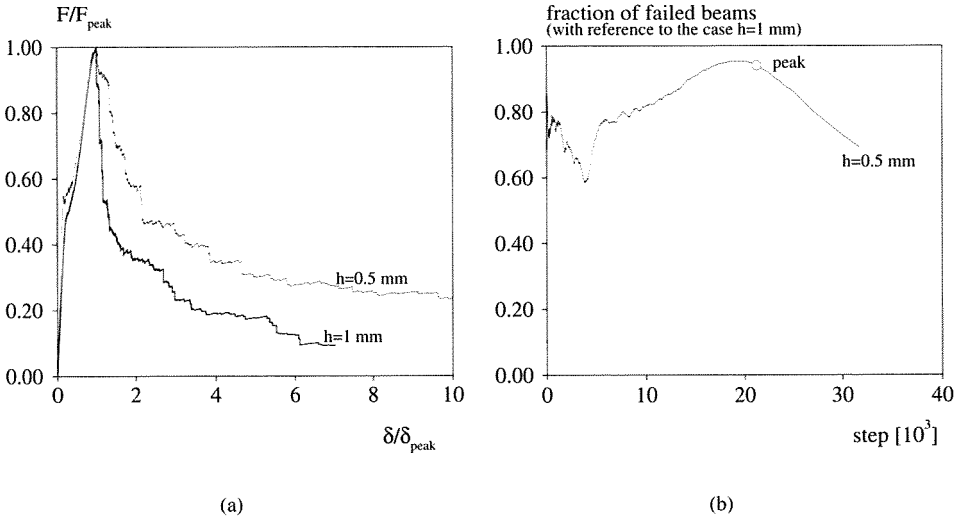
Figure 3.6: Comparison between 3D lattices with different height *h* of the cross section: (a) dimensionless load-displacement diagrams; (b) fraction of beams failing in the analysis with *h*=0.5 mm, referred to the number of beams failing in the analysis with *h*=1 mm.
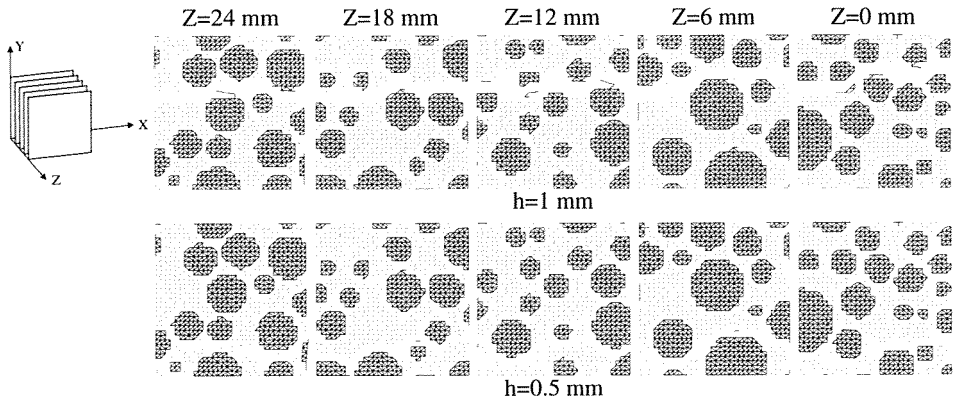


Figure 3.7: Comparison between 3D lattices with different height *h* of the cross section: crack patterns at step 31700, which corresponds to $\delta = 25\ \mu m$ in the analysis with *h*=1 mm. The 3D specimen is cut into slices, and the cracks are visualized on each slice. The displacements are amplified by factor 60.

The results demonstrate that the different height of the cross section of the beams causes not only different values of load and displacement at the peak, but also a different be-

haviour in the softening regime. Different values of load and displacement at peak can be expected as consequence of the different bearing capacity of the beams, and of the reduced overall stiffness of the sample. Different results in the softening regime indicate that the process of formation and propagation of macro-cracks is different in the two cases In this specific example, though the crack patterns at the peak are almost the same in the two analyses, they differ substantially in the post-peak regime. Figure 3.6(b) confirms this also. At the peak load, though in a different order, almost 100% of the beams that fail in one analysis also fail in the other analysis. In the post-peak regime this percentage decreases to 60% (at the end of the analysis, step 31718), and the final crack patterns are different: macro-cracks develop in the upper part of the specimen or in the bottom part when $h$=1 mm and $h$=0.5 mm, respectively (see Figure 3.7). The reason for the different cracks patterns has to be sought in the non-linear relation among the different contributions to the stiffness of the beams (axial, shear, bending, and torsional), which causes a different distribution of stresses among the different components and, as a consequence, removal of different elements in the lattice.

## 3.2.2  Heterogeneous lattice

So far attention has been focused on a lattice whose elements have all the same Young's modulus, $E_{beam}$. As particles are embedded in the lattice, the overall elastic properties will also depend on the particle content. To evaluate this dependence, the analysis conducted for the 3D homogeneous lattice were performed embedding particles with different densities. Then, the numerical results were compared with experimental and analytical results. Different grain distributions with a Fuller grading curve were generated, corresponding to an increasing density of the particles. The diameter of the particles is in the range of 2 mm to 14 mm. After the random positioning of particles, it was possible to reach the maximum density of aggregate beams $P_{k,latt} = 0.30$. Aggregate fractions smaller than 2 mm were neglected on purpose, as a finer mesh would have been required in this case. As usual in lattice analyses, it was assumed that the interfacial transition zone and the matrix have the same Young's modulus. Thus, only elastic properties of matrix and aggregate needed to be assigned. These properties were chosen accordingly to experimental results obtained by Anson and Newman [2], namely $E_m^* = 28.30$ GPa and $E_a^* = 69$ GPa for matrix and aggregate, respectively. The same Poisson's ration $v = 0.218$ was assigned to the two phases. The geometry and Young's modulus of the lattice beams were determined using the graphs in Figure 3.5. For the finest mesh ($s$=1 mm), and randomness $A/s$= 0.50, it was derived that $h/s = 0.2785$ and $E^*/E_{beam} = 0.1115$.

Different types of analytical models are available for predicting the elastic behaviour of a multi-phase medium. Such models are either based on effective medium theories [108], or on exact upper and lower bounds. Among the models based on upper and lower bounds, the Hashin-Shtrikman model [39] is considered here for comparison with the results from the lattice. The Hashin-Shtrikman model is based on the variational principles for non-homogeneous linear elasticity, in terms of the elastic polarization tensor, formulated by Hashin and Shtrikman [40]. The upper and lower bound of the bulk and shear modulus,
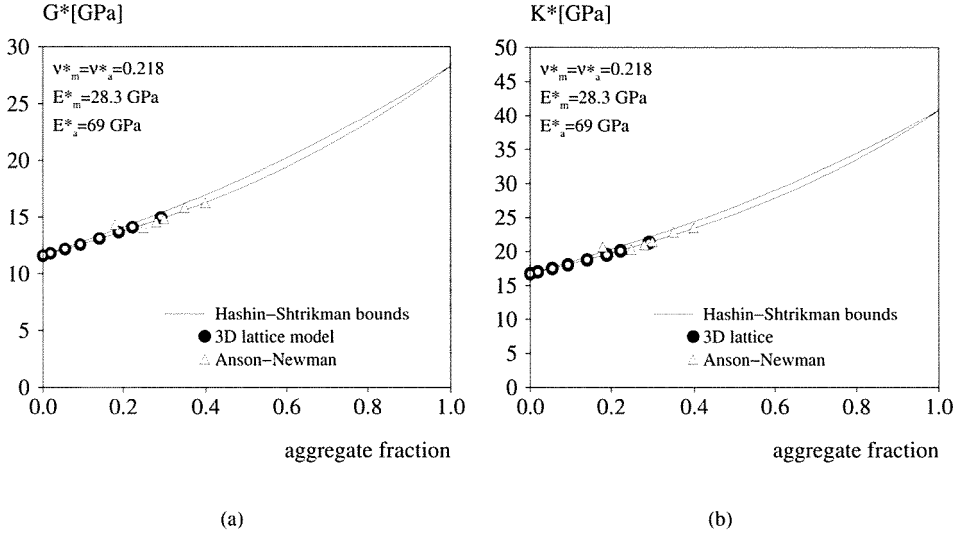
Figure 3.8: Comparison of results from a 3D lattice analysis, Hashin-Shtrikman analytical model and experimental results for the prediction of (a) the shear modulus and (b) the bulk modulus in a two-phase material.

$K^*$ and $G^*$, of a two-phase material are:

$$K^*_{bound,1} = K_1 + \frac{v_2}{1/(K_2 - K_1) + 3v_1/(3K_1 + 4G_1)}$$

$$K^*_{bound,2} = K_2 + \frac{v_1}{1/(K_1 - K_2) + 3v_2/(3K_2 + 4G_2)}$$

$$G^*_{bound,1} = G_1 + \frac{v_2}{1/(G_2 - G_1) + 6v_1/5G_1(K_1 + 2G_1)/(3K_1 + 4G_1)}$$

$$G^*_{bound,2} = G_2 + \frac{v_1}{1/(G_1 - G_2) + 6v_2/5G_2(K_2 + 2G_2)/(3K_2 + 4G_2)} .$$

(3.8)

The indices 1 and 2 in Equation 3.8 refer to the two phases with volumetric fractions $v_1$ and $v_2$, respectively. It is questionable whether concrete can be considered a two-phase material with respect to its elastic properties. The width and stiffness of the interfacial zone depend on the water/cement ratio, $w/c$. During the initial process of hydration and setting of the cement paste, the water migrates from the matrix to the surface of the aggregates. This produces a decrease in the stiffness of the interfacial transition zone, while the stiffness of the matrix increases. The global stiffness of the two phases (matrix and bond), considered as a whole, does not change when $w/c \cong 0.4$ [86]. In this case concrete can be considered as a two-phase material. However, for higher water/cement ratios, the loss of stiffness in the interfacial transition zone could prevail and result in a lower overall

stiffness of the system matrix-bond. As no extensive experimental data are available to quantify the Young's modulus of the interfacial transition zone, not much choice is left: consider concrete as a two-phase material (as in the analyses that are reported here), or perform a parametric study varying the Young's modulus of the interface. In Figure 3.8 the results obtained with the lattice model are compared with the results from the Hashin-Shtrikman model and with experimental results. The values of the bulk modulus and shear modulus calculated after loading the sample in the three different directions, $X$, $Y$ and $Z$, are indicated in Figure 3.8 with black dots, while their average is indicated with opaque circles.

It can be observed that, independently of the aggregate content, the lattice behaves like an almost-isotropic material. Furthermore, the prediction of the 3D lattice model is consistent with the values of $G^*$ and $K^*$ derived from the Hashin-Shtrikman analytical model. Though, while $G^*$ always falls between the lower and upper bound of the model, $K^*$ is always on the lower bound. Similar results were obtained for the 2D lattice in [101]. Also the deviation from the experimental results by Anson and Newman [2] is small.

## 3.3 Concluding remarks

The overall elastic properties of a 3D beam lattice depend on the geometry of the lattice and the density of the particles that are embedded in the lattice.

In *homogeneous* lattices, namely lattices whose elements have all the same Young's modulus, the overall Young's modulus $E^*$ depends on the ratio $h/s$ between diameter of the cross section and size of the lattice cell, and on the Young's modulus of the beams, $E_{beam}$. The Poisson's ratio $\nu^*$ depends on $h/s$ but also on the randomness.

The comparison between the elastic behaviour of 2D and 3D lattices shows that 3D lattices, though relatively coarse meshes are used, are less sensitive to directional effects when the elastic properties are computed considering the influence of the boundaries. Furthermore, the range of variation of $\nu^*$ with the randomness is smaller.

However, the upper bound found for the Poisson's ratio of a 2D beam lattice (1/3) differs from the upper bound found for a 3D beam lattice (1/4), which is consistent with the outcome from analytical analyses. The reason is that in the 2D beam lattice the equivalent continuum to the lattice can be considered under the two different conditions of plane stress and plane strain. Plane stress is the scheme which is always adopted and brings to the upper bound $\nu^* = 1/3$. If plane strain is considered instead, the upper bound would be $\nu^* = 1/4$. Therefore in a 2D beam lattice a different geometry should be assigned to the lattice depending on the assumption of plane stress or plane strain for the equivalent continuum, though the material to be schematized is the same. Due to the non-linear relation among the contributions to the stiffness of the beams (axial, shear, bending and torsional), this would also affect the fracture process.

Results obtained from *heterogeneous* lattices, which also embed particles, show to be consistent both with the results from analytical models and experiments, at least in the range of particle densities that was considered in this study. The assumption that concrete, as

it is modelled in the lattice, is a two-phase material with respect to the elastic properties does not contradict the experimental data that were found in literature.

# Chapter 4

# Effect of aggregate content on the fracture mechanism

Concrete is a composite material whose properties depend on the properties of the single components and their interactions. It is recognized that the interfacial transition zone (ITZ) plays a major role in the mechanical behaviour of normal strength concrete, as the ITZ represents the weakest link between particles, which are stiff and strong, and the matrix. Also the properties of matrix and particles have effects on the fracture mechanism in concrete. The relative strength of matrix and particles, as well as the size, shape and content of particles can have a considerable effect on some of the properties of concrete. Extensive experimental studies have been conducted to investigate the effect on the fracture mechanism of: type of aggregate ([51], [49], [111]), aggregate size ([116], [92]), coarse aggregate and ratio of coarse to fine aggregate ([115], [33], [35]), aggregate shape ([31]), total aggregate content ([1]).

In this chapter, results from lattice analyses conducted varying the particle content both in 2D and 3D lattices are reported. A similar study was already conducted with 2D lattices by van Vliet [101], who considered both the effect of the aggregate content and of the aggregate structure. The conclusion from this study was that the percentage of weak elements governs the lattice response. As the mesh adopted in this study was relatively coarse $l_{beam} = 1$ mm, small fractions of the particle distributions could not be represented and the maximum possible aggregate density was $P_{k,latt} = 0.48$, which was obtained from an initial particle density $P_k = 0.80$. As soon as the lattice model was implemented in a code for parallel computing [59], however, much finer meshes could be analyzed, and higher aggregate densities could be reached, up to $P_{k,latt} = 0.62$.

## 4.1  Effect of particle density on the 2D lattice response

### 4.1.1  Model

The model used for studying the effect of the particle density was a 2D triangular lattice with a square shape, with size $B =60$ mm (see Figure 4.1). The specimen was clamped at the bottom and top edge, and loaded with a uniform vertical displacement at the nodes of the top edge. The length of the lattice beams was $l_{beam}$=0.25 mm, resulting in a total number of elements equal to 200261. The height of the beam was chosen as $h =0.144$ mm, so that the overall Poisson's ratio of the lattice was $v^* \approx 0.20$, following Equation 3.1.
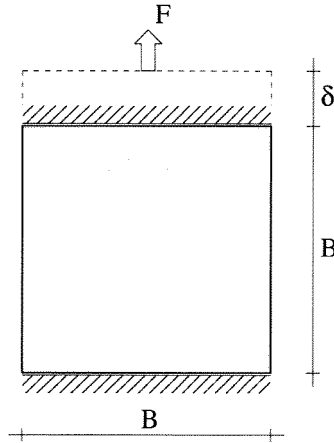


Figure 4.1: Model used for studying the effect of particle density in a 2D lattice.

The particle distribution consists of grains having a diameter in the range of 1 mm-12 mm, and a sieve curve as shown in Figure 4.3(a). This curve gives the percentage in volume (area in case of 2D) of aggregate passing through a sieve with a size of the square net equal to $d_a$. Starting from a relatively sparse distribution with volumetric density $P_k = 0.35$, see Figure 4.2(a), the surface occupied by the particle volume (surface in this case) was contracted until densities $P_k = 0.51$, see Figure 4.2(b), $P_k = 0.67$, see Figure 4.2(c) and $P_k = 0.83$ were reached. In the following, only results for $P_k = 0.35, 0.51, 0.67$ will be analyzed. In Chapter 2 it was already outlined that the particle density after positioning of the particles is smaller than the desired density, $P_{k,eff} \leq P_k$. The density is even smaller after overlaying the lattice on top of the particles ($P_{k,latt} \leq P_{k,eff}$). The values of particle density for the model analyzed in this chapter are reported in Table 4.1. The different phase fractions in the lattice are represented in Figure 4.3(b). Figure 4.3(b) shows that when the aggregate density increases also the fraction of bond increases, while the matrix fraction decreases.

| $P_k$ | $P_{k,eff}$ | $P_{k,latt}$ |
|------|------|------|
| 0.35 | 0.30 | 0.26 |
| 0.51 | 0.43 | 0.38 |
| 0.67 | 0.56 | 0.52 |

Table 4.1: Density of 2D aggregate lattice elements versus particle density.



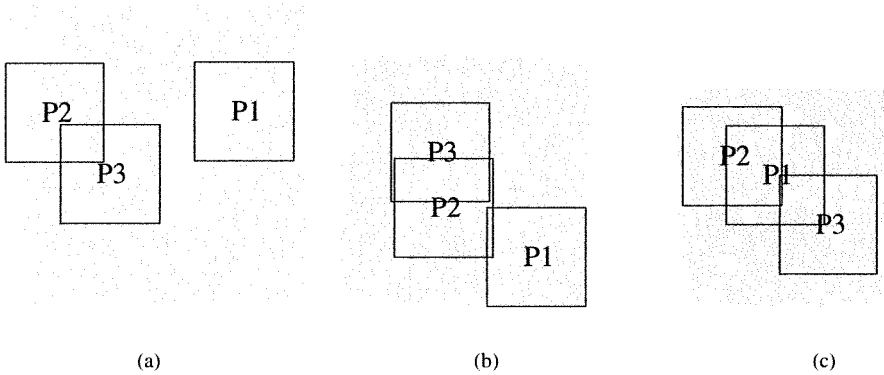(a)                    (b)                    (c)

Figure 4.2: 2D particle distribution.

The relative values of stiffness and strength assigned to the beams in the lattice were: $E_a/E_m = 70000/25000$, $E_m/E_b = 25000/25000$, $f_{t,a}/f_{t,m} = 10/5$ and $f_{t,m}/f_{t,b} = 5/1.25$. Due to the random structure of the material some scatter is to be expected in the results. For this reason, three different samples were considered for each particle density. These samples were obtained overlaying the lattice on top of the particles distribution at random positions, $P1, P2, P3$. After $P1$ was assigned, $P2$ and $P3$ were selected among all other possible positions to give approximately the same number of aggregate lattice elements as $P1$.

In the fracture criterion adopted in this analysis, according to previous 2D analyses, the contribution of the bending moment to the critical stress in the beam is taken into account by means of the coefficient $\alpha = 0.005$ [79, 103, 101].

## 4.1.2   Fracture mechanism

For understanding how the fracture mechanisms develop in the lattice, such mechanism will be analyzed in this paragraph in one of the specimens with particle density $P_k = 0.35$ (specimen $PK35\_P2$).

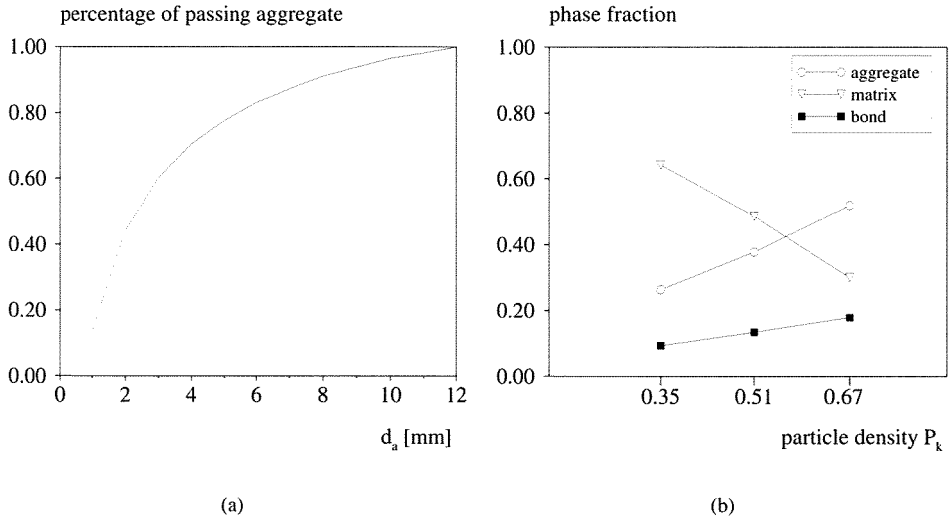Figure 4.3: (a) Sieve curve of the 2D particle distribution. (b) Phase fractions in the 2D lattice versus particle density.
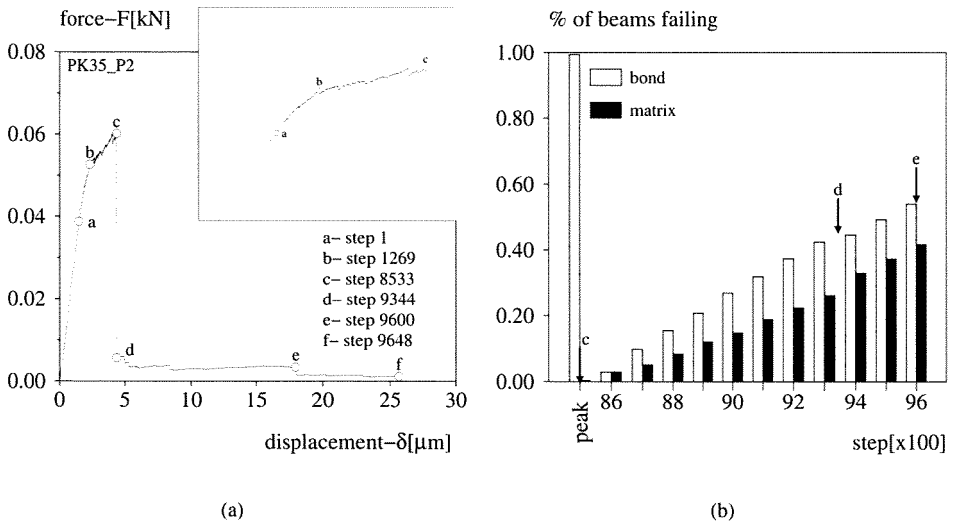


Figure 4.4: 2D lattice analysis of a specimen with $P_k = 0.35$. (a) Load-displacement diagram. (b) Percentage of bond and matrix beams, referred to the total number of beams failing between different loading stages. After the peak, intervals of 100 steps are considered.

The load-displacement diagram is shown in Figure 4.4(a). Different stages, which are indicated with different letters in the load-displacement diagram, can be identified in the fracture mechanism. In *a* the first element is removed from the mesh. In *c* the peak load is reached and the softening regime starts. After *c* the load exhibits a steep drop until *d*. After *d*, the structure can still carry some load, while undergoing relatively large displacements.

Figure 4.4(b) shows the percentage of the total number of beams removed in a steps interval. In Figure 4.4(b) the situation before and after the peak is considered. The first steps interval goes from step 1 to step 8533, which corresponds to the peak load. In this interval 99.5% of beams that fail are bond elements. After the peak, only 1115 steps are necessary to reach a vertical displacement of 25 $\mu$m, which is conventionally assumed in this analysis as point of structural failure. The 1115 steps interval is divided in sub-intervals of 100 steps, and the percentage of beams failing in each sub-interval is reported in Figure 4.4(b). Figure 4.4(b) suggests that, while only (or mainly) de-bonding occurs in the pre-peak regime, cracks start to propagate through the matrix in the post-peak regime. The crack patterns in Figure 4.5(a) and (b) represent the bond elements (in white) and matrix elements (in black) failing up to the point *b* of the load-displacement diagram and at peak, respectively. The extensive de-bonding preceding the peak corresponds to the hardening regime in the load-displacement diagram, from point *b* to point *c* in Figure 4.4(a). Two factors can contribute to the extensive failure of bond elements in the pre-peak regime:

1 The stress concentrations at the interface between aggregate and matrix, due to the high stiffness of the aggregate elements in comparison with bond and matrix elements;

2 The low strength of the bond elements.

After each beam is removed, the stresses in the specimen change and other bond elements fail at other locations, see Figure 4.5(a) and (b). The initial response of the specimen is nearly linear up to point *b* in the load-displacement diagram. However, as de-bonding progresses, the behaviour becomes non-linear: this corresponds to the pre-peak hardening in the load-displacement diagram (from point *b* to point *c* in Figure 4.4(a)).

When the stress distribution is such that no further sparse micro-cracking is possible anymore, cracks start localizing by propagating from particle to particle through the matrix. In the load-displacement diagram this corresponds to the peak load and to the steep drop of load after the peak. The crack pattern at the end of the load drop (point *d* in the load-displacement diagram) is illustrated in Figure 4.6(a). At this stage a relatively straight crack can cross the specimen through its complete width. The dashed box in Figure 4.6(a) indicates the zone where the crack localizes. Formation of the macro-crack results from propagation and coalescence of existing micro-cracks. Isolated micro-cracks still form, but always near the macro-crack. The elements failing during the steep load drop are drawn in Figure 4.6(b), which shows that beams fail both in the bond and matrix phase.

It is recognized that crack branching and bridging contribute to the residual bearing capacity of specimens loaded in tension during the tail of the softening regime. The bridg-
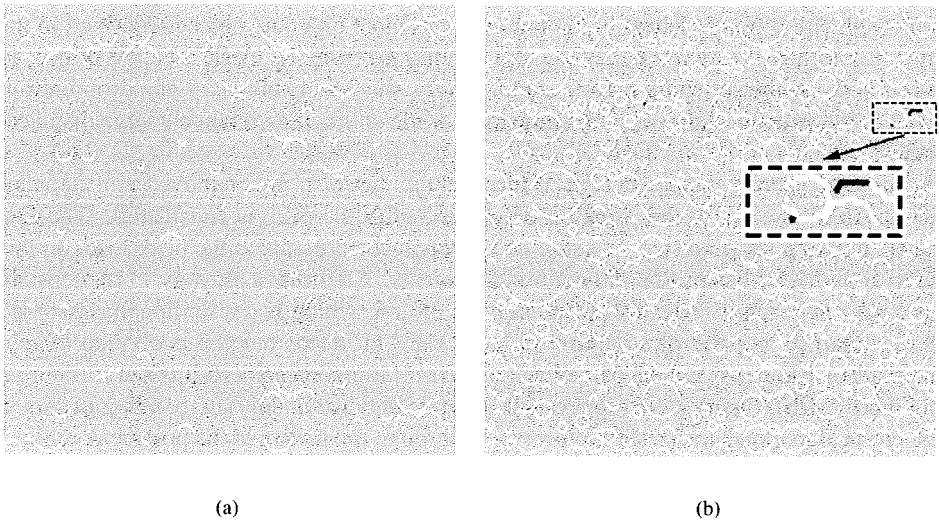
(a)                                                    (b)

Figure 4.5: 2D lattice analysis of a specimen with $P_k = 0.35$. (a) Crack patterns at step 1269 and (b) at step 8533 (points $b$ and $c$, respectively, in the load-displacement diagram of Figure 4.4(a)).

ing phenomenon occurs when adjacent cracks are still connected through pieces of intact material. Stresses are then transmitted mainly by rotation of these intact pieces. Crack branching and bridging may cause a tortuous crack path that depends on the texture of the material and contribute at this manner to increase the energy necessary to fracture the specimen. These phenomena, found experimentally [96], result also from lattice analysis. Examples of crack branching and bridging can be found in Figure 4.7. In Figure 4.7(a) and Figure 4.7(b) the crack is zoomed-in at stage $d$ and $e$ of the load-displacement diagram. It can be observed that during this loading stage the crack opening increases while the load level remains practically constant and nearly zero. As in $d$ the crack has already crossed the specimen, this has no other resources for bearing the load than branching and bridging mechanisms. In the tail of the softening, when also branching and bridging resources are almost exhausted, it is sufficient to remove only a few elements to obtain a large crack opening. In this example, only 48 elements fail between the points $e$ and $f$ in the load-displacement diagram.

(a)                                                          (b)
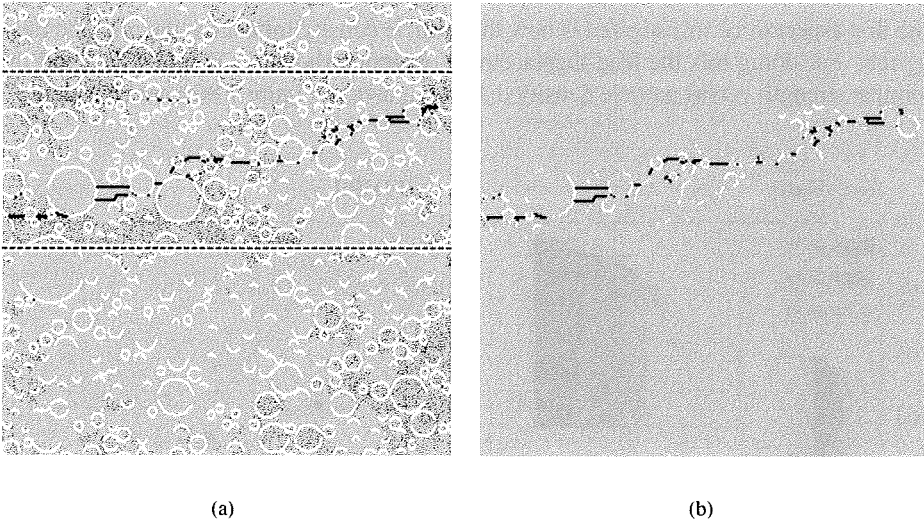
Figure 4.6: 2D lattice analysis of a specimen with $P_k = 0.35$. (a) Crack pattern at step 9344 (point $d$ in the load displacement diagram of Figure 4.4(a)). (b) Matrix and bond elements failed during the steep load drop beyond the peak (from point $c$ until point $d$ in the load displacement diagram of Figure 4.4(a)).



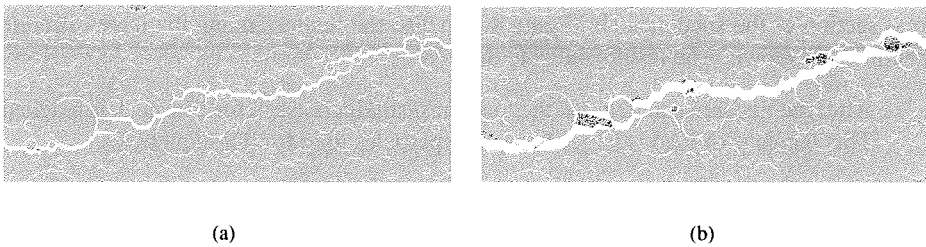(a)                                                          (b)

Figure 4.7: 2D lattice analysis of a specimen with $P_k = 0.35$. Detail of the crack shown in Figure 4.6: (a) at step 9300 and (b) at step 9600. The displacements are amplified by factor 150.

### 4.1.3    Results with different particle densities

**Pre-peak and peak regime**

The first aspect to be investigated is how the particle density influences the pre- and peak regime. For doing this the load-displacement diagrams shown in Figure 4.8(a) and the nominal strength versus particle density diagram drawn in Figure 4.8(b) are considered.
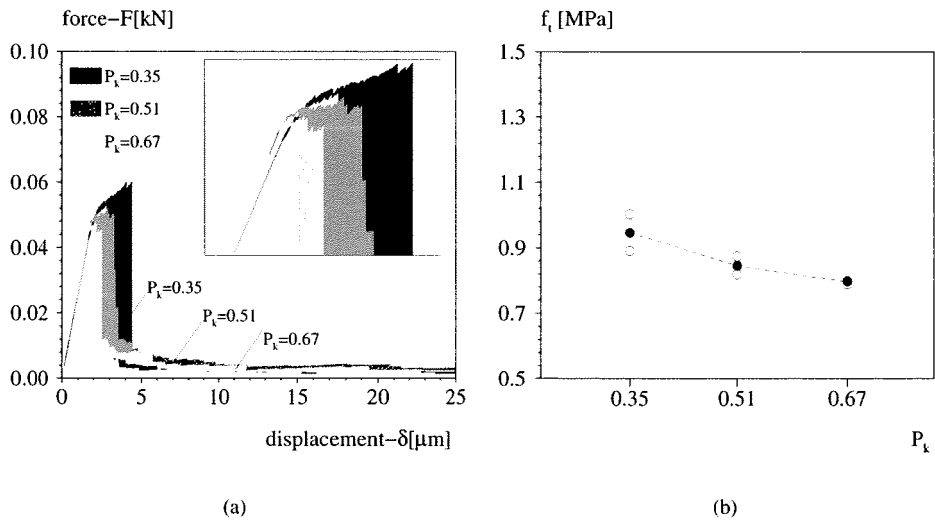


(a)

(b)

Figure 4.8: 2D lattice analyses with different particle densities. (a) Load-displacement diagrams. (b) Nominal strength versus particle density.

The nominal strength has been calculated dividing the load at the peak by the area of the cross section of the specimen. In Figure 4.8(a) also the scatter among the three different specimens is shown. The results indicate that:

- After the linear elastic regime, the load must still increase before the peak is reached. This increase of load is larger for sparse particles than for dense particles.

- The nominal strength decreases when the particle density increases. For denser particles the decrease in strength is more gradual. Based on these results, one could speculate that a critical value of particle density exists after which the strength reaches a constant value. This is a speculation, though, and more numerical analyses would be necessary to confirm this statement.

In order to have a better understanding of the mechanisms that cause the pre-peak non-linearity, the point where the load-displacement diagram becomes non-linear has been investigated. In Figure 4.9(a) it is sketched how this point, which is indicated with *b* in

Figure 4.4, has been identified in different load-displacement diagrams. The corresponding values of the load are drawn in Figure 4.9(b) as function of the particle density. Also the load which causes failure of the first beam and the peak load are indicated.

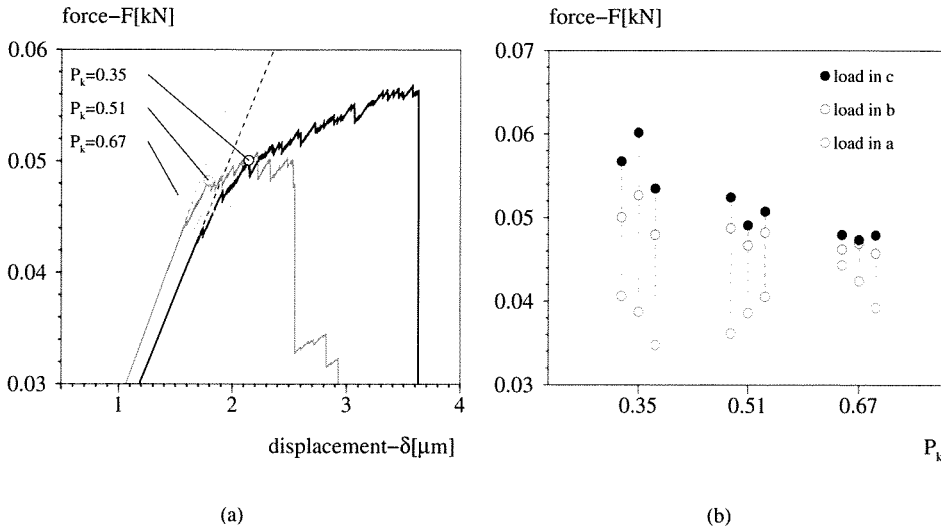

(a)                    (b)

Figure 4.9: 2D lattice analyses with different particle densities. (a) Transition from the linear to the non-linear regime before the peak load. (b) Characteristic load levels in the pre-peak regime (see Figure 4.4).

A clue to the different pre-peak responses is given by the crack patterns. The crack patterns in some of the specimens are drawn in Figures 4.10, 4.11 and 4.12 for two different levels of load: at the end of the linear elastic regime, and at the peak load. In these figures the fractured elements that belong to the ITZ are drawn in white. If matrix elements fail, these are drawn in black. In the pre-peak regime, fracture is basically de-bonding and the crack morphology has a specific character: it is distributed over the whole area of the specimen if the particle distribution is sparse, it is localized in regions if the particles are denser. Clearly it is the mutual distance of the particles, or of the interface regions surrounding them, to determine the structural response. As long as the stress levels prevent cracks from propagating through the matrix, these remain confined in the interface regions. As a consequence, sequential failure occurs at relatively far locations if the particles are sparsely distributed. Due to its distributed character, quite an extensive micro-cracking develops in the specimen before starting to coalesce and a relatively high load can be reached. On the contrary, when particles are densely distributed, the mutual distance of the micro-cracks decreases and coalescence occurs at an earlier loading stage. Initially, damage in the specimen is still limited and the specimen behaves linearly elastic, see Figures 4.10(a), 4.11(a) and 4.12(a). As cracking progresses, the structural response

becomes non-linear. The different pattern of micro-cracks corresponds to a difference in the load-displacement diagram: the more distributed are the micro-cracks, the higher are the loads that can be reached and the more extended is the non-linear pre-peak branch of the load-displacement diagram. It should be remarked that the spatial distribution is important and not the number of elements failing. It might be expected that, if more elements fail, the non-linear part of the load-displacement diagram in the pre-peak regime becomes longer. A simple comparison of Figure 4.10(b) and Figure 4.12(b) can demonstrate the opposite. These figures show the crack patterns whose load-displacement diagrams are shown in Figure 4.9(a). The number of elements that fail until the peak load is in this case comparable.

Also the distribution of crack lengths is not influencing the pre-peak behaviour. For sake of simplicity, the cracks have been measured after they have been projected in the horizontal direction. Figure 4.13(a) and Figure 4.13(b) report the distribution of crack lengths for a sparse and a dense particle distribution, respectively. In both cases the majority of cracks have length $\leq 2$ mm and only a few cracks of 4 mm are found.



(a)                                                                           (b)

Figure 4.10: 2D lattice analyses of a specimen with particle density $P_k = 0.35$. Crack pattern (a) at the beginning of the non-linear pre-peak regime and (b) at peak.

(a) (b)

Figure 4.11: 2D lattice analyses of a specimen with particle density $P_k = 0.51$. Crack pattern (a) at the beginning of the non-linear pre-peak regime and (b) at peak.
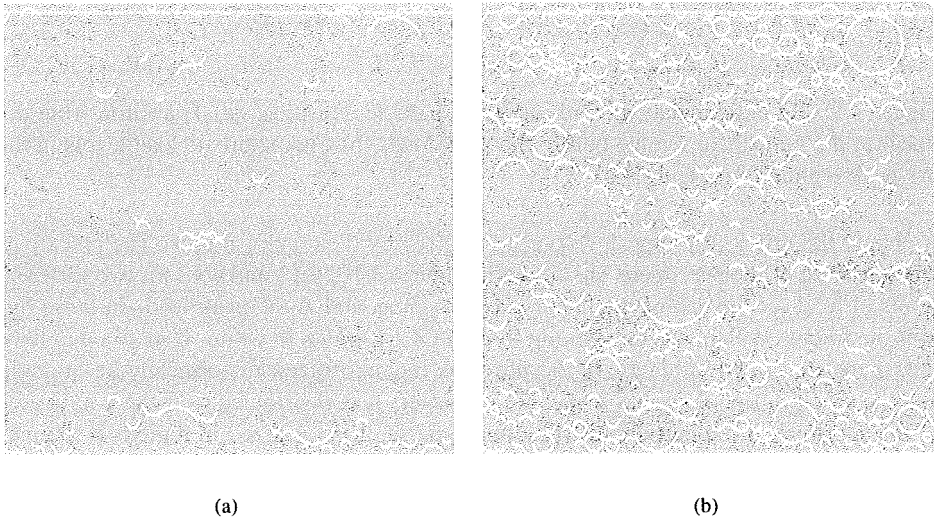




(a) (b)

Figure 4.12: 2D lattice analyses of a specimen with particle density $P_k = 0.67$. Crack pattern (a) at the beginning of the non-linear pre-peak regime and (b) at peak.
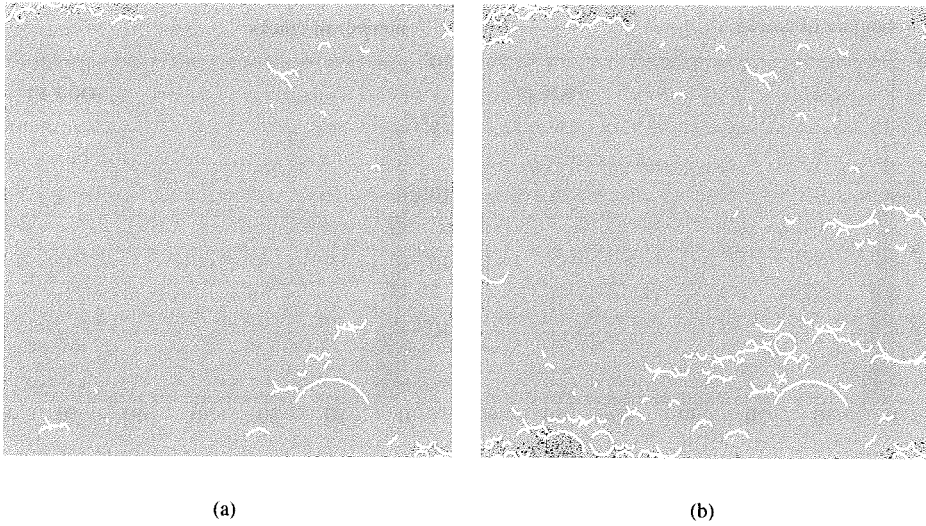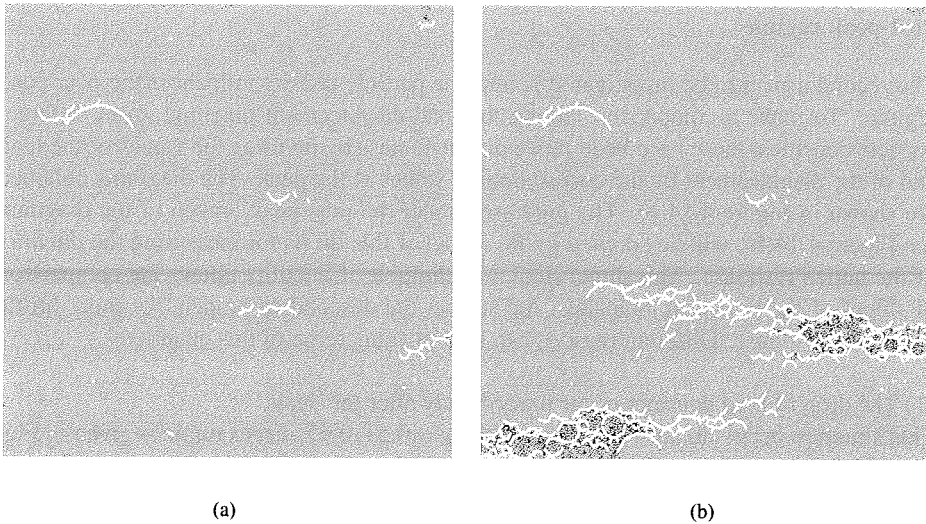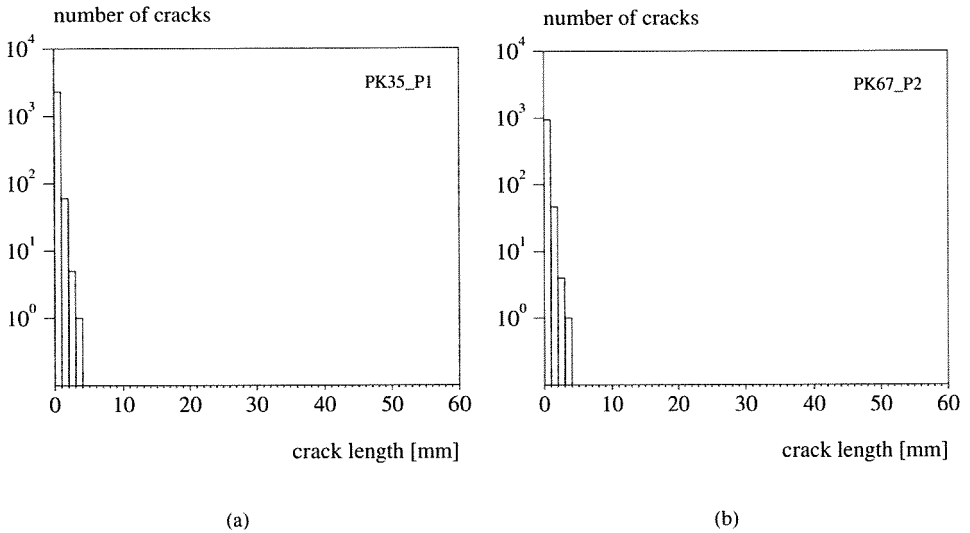
Figure 4.13: 2D lattice analyses with different particle densities. Distribution of crack lengths at peak for a specimen with (a) $P_k = 0.35$ and (b) $P_k = 0.67$.


**Post-peak regime**

The second aspect to be investigated is how the particle density influences the post-peak regime. To make a comparison among the load-displacement diagrams from different particle densities, these have been made dimensionless by dividing the values of the load and of the displacement by the corresponding values at the peak. The diagrams obtained are shown in Figure 4.14(a). The grey area under the post-peak branch of the diagram, see Figure 4.14(b), will be adopted in the sequel of this thesis for measuring the *ductility* of the lattice response. This dimensionless definition of ductility allows the comparison of slopes of the post-peak branches: the steeper the descending branch, the more brittle the lattice response. Different reasons can lead to an increase of this quantity.

(1) The drop of load does not occur immediately after the peak.
This situation occurs in all simulations with $P_k = 0.51, 0.67$. An example is given in Figure 4.14(b), where the responses of a lattice with $P_k = 0.35$ and $P_k = 0.51$ are compared. In the lattice with $P_k = 0.35$ the load drops immediately beyond the peak while in the lattice with $P_k = 0.51$ there is first a decrease of load with increasing displacement before the steep drop. The reason of such behaviour is that in the specimens with denser particles a more extensive micro-cracking at peak must occur before cracks can start to coalesce. This phenomenon is illustrated in Figure 4.15 for one of the specimens with $P_k = 0.51$.

(a)  (b)

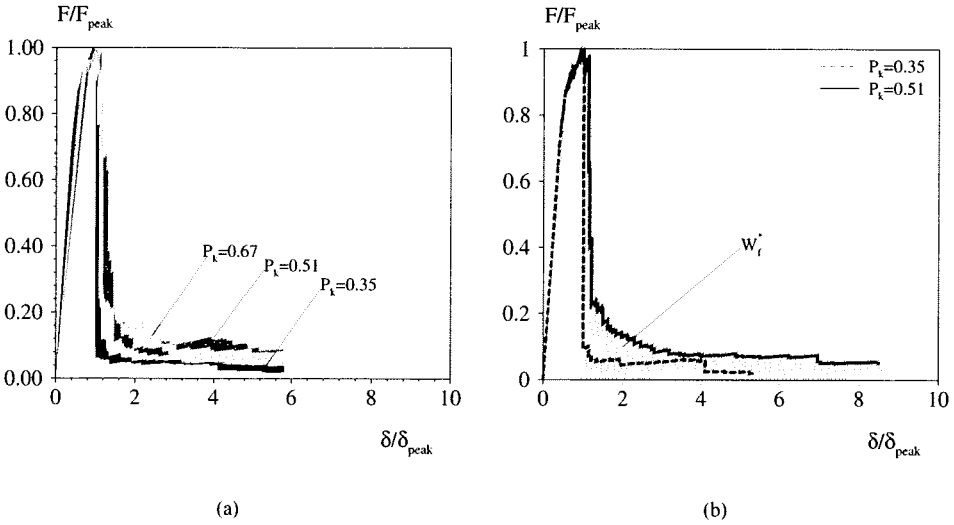Figure 4.14: 2D lattice analyses with different particle densities. (a) Dimensionless load-displacement diagrams. (b) The area under the post-peak branch of the dimensionless load-displacement diagram indicates the brittleness of the lattice response.
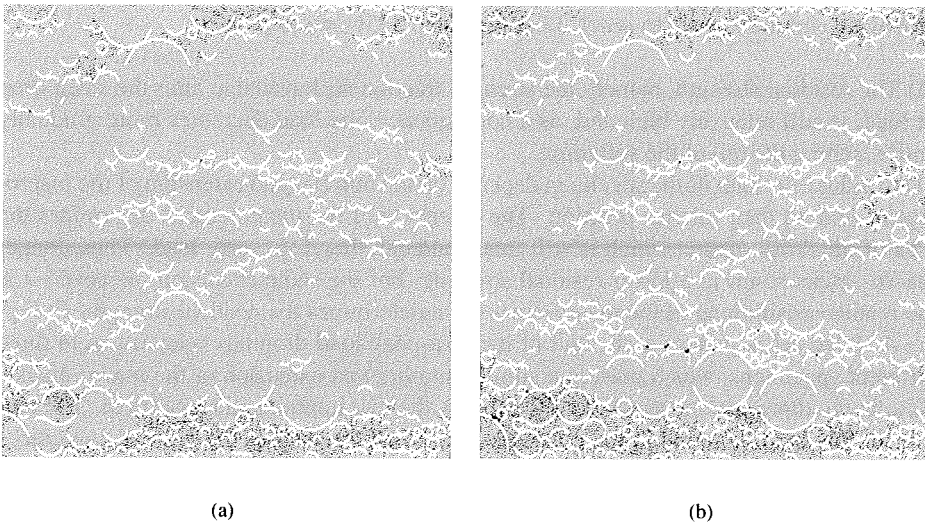


(a)  (b)

Figure 4.15: 2D lattice analyses of a specimen with particle density $P_k = 0.51$. Cracks (a) at peak and (b) at the onset of the steep post-peak load drop.

(2) The steep load drop after the peak exhibits a zigzag shape.

It has already been outlined that during the steep load drop after the peak micro-cracks coalescence to form macro-cracks. An example how the macro-cracks form and propagate in a specimen with sparse particle density is given in Figure 4.16. In order to filter the macro-crack(s), the crack pattern is represented by means of the deformed shape of the specimen, with the displacements amplified by a factor 150. Only the part of the specimen where macro-cracks are located is represented in the figure. The cracks have been detected at three different load levels, which are indicated in the load-displacement diagram with the corresponding step number. In this specimen only one continuous macro-crack forms and propagates from the left to the right side of the specimen.

Rather than one macro-crack propagating through the width of the specimen, more macro-cracks can form and propagate. Such mechanism can be quite complex both in the manner it evolves in time as well in space. Pre-existing macro-cracks can temporarily arrest or propagate simultaneously to new macro-cracks, which have formed at different distances from the previous. In this process, if micro-cracking still occurs before new macro-cracks form, or pre-existing macro-cracks propagate, an increase of load can be registered. In the load-displacement diagram this corresponds to a zigzagging where the vertical portions correspond each time to formation of a new macro-crack. To elucidate this concept, the evolution of macro-cracks in one of the specimens with $P_k = 0.51$ has been drawn in Figure 4.17. In this case four different macro-cracks form at different load-levels. After the first two macro-cracks have formed, they arrest while new micro-cracks form. At step 4931 a third macro-crack starts to form at a relatively far distance from the previous macro-cracks. Bewteen step 4931 and step 5433 this and the second of the first two cracks (*crack* 2) propagate. In a similar manner, a fourth crack will form at step 5756, which will propagate simultaneously to *crack* 3 between step 5756 and step 5871.

(3) The residual strength, namely the strength fraction still available after the steep drop of load, is still relatively high and, as a consequence, the load decreases more gradually until reaching the tail of the softening.

The residual strength of the specimen depends on the number and extension of the macro-cracks, and on their relative position. The extension of the macro-cracks determines the area of the cross section which is still intact and can therefore carry load. Thus, longer macro-cracks result in a lower residual strength. For the same extension, however, it is the relative positioning of the macro-cracks that determines the residual strength. In Figure 4.18 the crack pattern at the end of the post-peak load drop has been drawn in three different specimens, which present a similar number and extension of the macro-cracks. Among the three specimens, *PK*51_*P*1 exhibits the maximum residual strength. The reason for this is to be found in the crack lay-out. In all three cases the pre-existing cracks should propagate or new cracks should form in order to generate one crack running from side to side of the specimen. In the specimens with *PK*35_*P*2 and *PK*51_*P*3 the necessary extension of existing macro-cracks is relatively short and coalescence into one crack can occur without the pre-existing cracks deviate too much from their current direction. On the contrary, for reaching complete failure of the specimen *PK*51_*P*1 either it will be necessary that one of the existing cracks propagates through nearly half of the specimen,
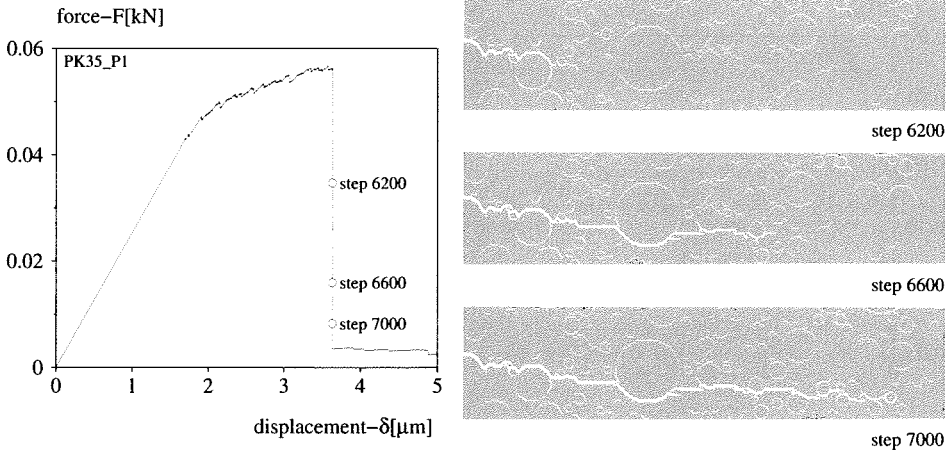
Figure 4.16: 2D lattice analyses of a specimen with particle density $P_k = 0.35$. Crack propagation in the post-peak regime. The displacements are amplified by factor 150.
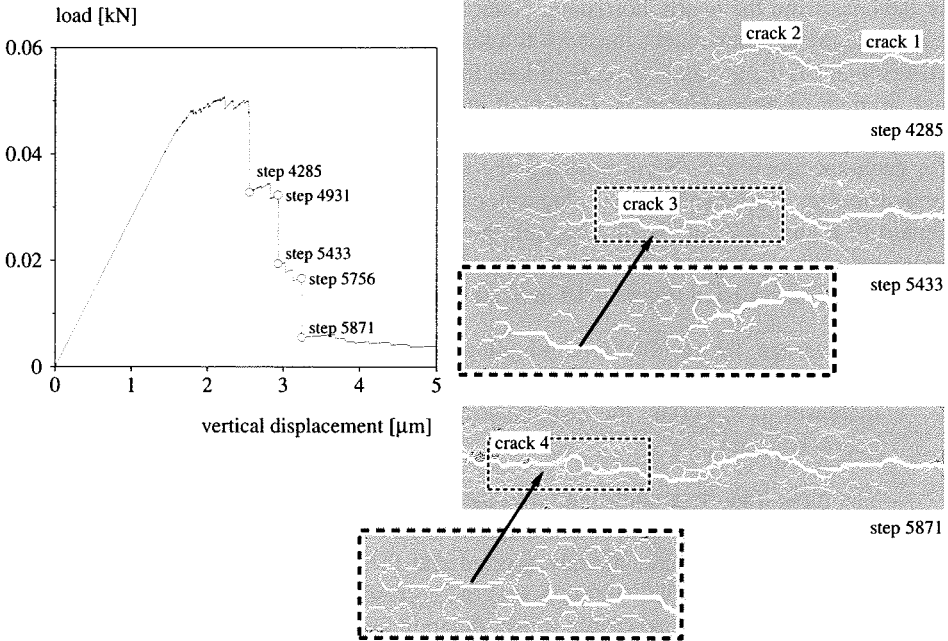


Figure 4.17: 2D lattice analyses of a specimen with particle density $P_k = 0.51$. Crack propagation in the post-peak regime. The insets show details of *crack* 3 and *crack* 4 at steps 5000 and 5700, respectively.
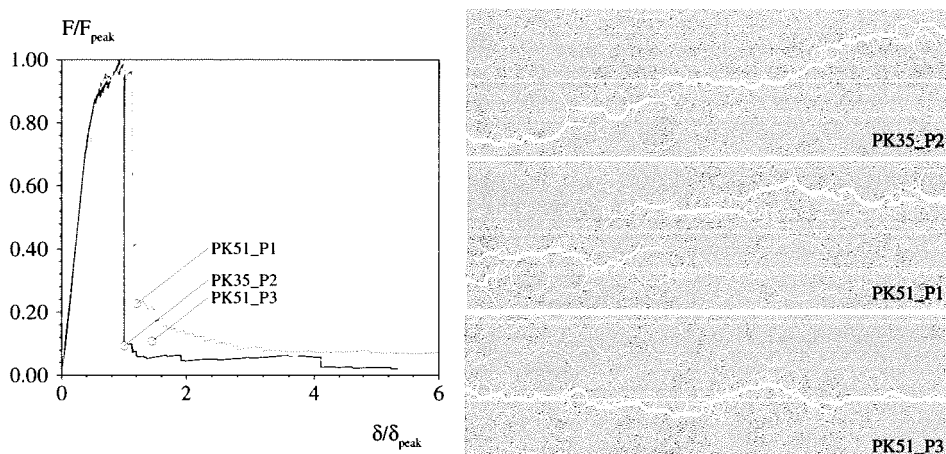
Figure 4.18: 2D lattice analyses with different particle densities. Macro-crack patterns at the end of the steep post-peak load drop in specimens with different particle density.

or deviates from the nearly horizontal pattern to coalesce with the other cracks. In both cases, the pre-existing cracks must cover a long distance before the specimen fails, which corresponds to the gradual decrease of load in the tail of the softening regime. The residual strength of all specimens is presented in Figure 4.19(a). The black dots connected with dashed line represent the average value while with the white dots the values obtained for each specimen have been represented. The area under the post-peak branch of the dimensionless load-displacement diagram, calculated at the value $\delta/\delta_{peak} \approx 6$, is represented in Figure 4.19(b). In the diagram the different contributions to the total area are indicated with different gradations of grey. The black dots represent the average value. The results illustrated in Figure 4.19 indicate that:

- On average, the residual strength after the steep post-peak drop of load increases when the particle density increases from $P_k = 0.35$ to $0.51$. If the particle density increases to $P_k = 0.67$ the residual strength does not increase further but remains nearly constant.

- The most important contribution to the area under the post-peak branch of the dimensionless load-displacement diagram is given by the tail of the softening, after the macro-cracks have already formed and the load has dropped from the peak value. As the residual strength, also the corresponding fraction of the area under the dimensionless load-displacement diagram increases, and when the particle density increases to $P_k = 0.67$, it appears even to decrease. However, this decrease might be consequence of the scatter in the results only.

All the results obtained show that the fracture mechanism is affected by the increasing density of particles, until *a critical value* is reached. When the particle density increases,

the mutual distance between the particles decreases and clusters of particles can form.



(a)                                    (b)
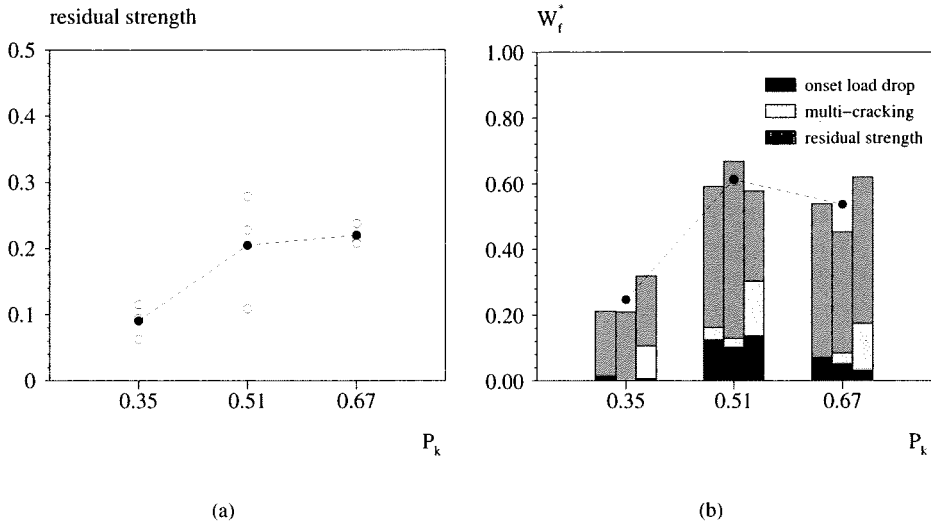
Figure 4.19: 2D lattice analyses with different particle densities. (a) Strength fraction measured at the end of the steep post-peak load drop. (b) Area under the post-peak branch of the dimensionless load-displacement diagram: contribution of different crack mechanisms.
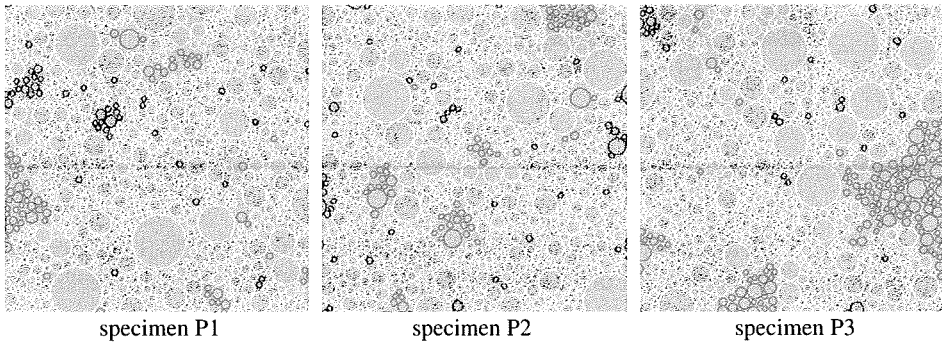


Figure 4.20: Patterns of interface elements in specimens with $P_k = 0.67$: percolated interface elements are represented in light grey; not percolated clusters of interface elements are represented in dark grey.

The interfacial transition zone surrounding the particles can then form continuous paths whose length depends on the size of the clusters. Eventually, the length of these paths can

extend to the whole width of the specimen. This situation is known as *percolation* of the bond phase. In normal concrete, where cracks develop through interface and matrix but not through aggregates, clusters of bond elements are preferential locations for formation of cracks. It might be expected in case of percolation that the crack develops completely through the interfacial transition zone, without crossing the small portions of matrix. This is well possible but depends also on the relative position of the particles in the cluster. If the path is too tortuous the crack would probably choose a straighter way through the matrix. This occurs for example in the specimens with $P_k = 0.67$. The clusters of bond elements in the three specimens are shown in Figure 4.20, where the percolated elements are represented in light grey, while the not percolated elements are represented in dark grey . Though in all three specimens one continuous path of bond elements with length 60 mm can be found, the crack detected at the end of the numerical experiment crosses the specimen passing through the matrix connecting the path of percolated bond elements with other clusters.
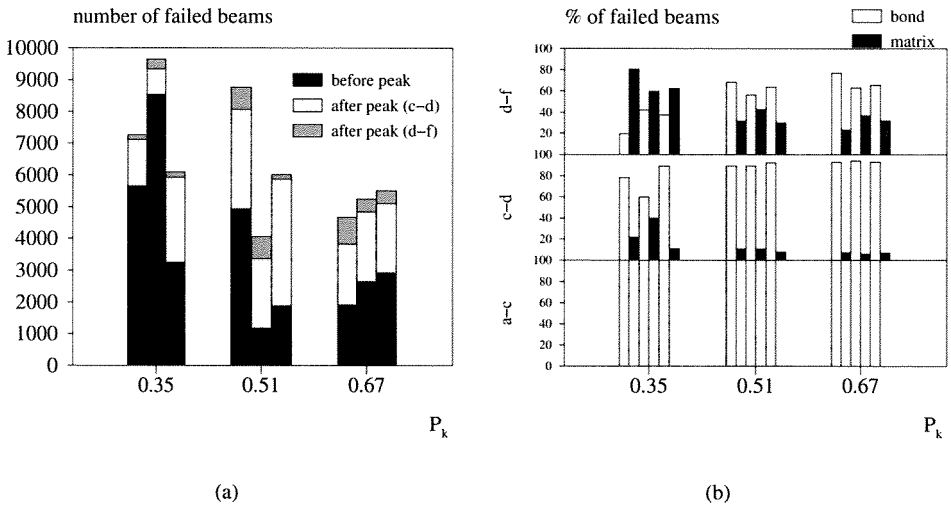
Figure 4.21: 2D lattice analyses with different particle densities. (a) Total number and (b) percentage of the number of beams that fail between different loading stages (see Figure 4.4).

Figure 4.21(a) illustrates how the number of failing elements varies with the different particle densities. Figure 4.21(b) represents the different fractions failing in the pre-peak and post-peak regime. In the specimens with low particle density the largest fraction of elements is removed before the peak, while in the specimens with denser particles the number of elements removed in the post-peak regime is comparable to (in the case of $P_k = 0.67$), if not bigger (in the case of $P_k = 0.51$) than the number of elements removed in the

pre-peak regime. In any case, the number of elements removed in the tail of the softening curve represents a negligible part in comparison with the post-peak load drop, which suggests that the crack branching and bridging is very limited in this analysis. There is no correlation between the total number of elements failing and the particle density. This suggests that to govern the overall fracture response is the way cracks distribute over the specimen. And this depends not only on the particle density, but also on the particle distribution. As a matter of fact, if particles all of the same diameter but with the same density would be considered, a different overall response would probably be found again, which would also depend on the spatial distribution of the particles, namely on the degree of disorder of their packing. In Figure 4.21(b) the fractions of the different phases failing at different loading stages, namely up to the peak $(a - c)$, in the post-peak load-drop $(c - d)$ and in the tail of the softening $(d - f)$, have been represented. The numbers in the diagram indicate the percentages of beams failing during each of the loading stages, which belong to the matrix or to the bond, respectively. The histogram shows that only de-bonding occurs in the pre-peak. Immediately after the peak cracks propagate in the matrix but the largest fraction of beams that fail are still bond elements, especially in the specimens with denser particles. In the tail of the softening regime cracks occur mainly in the matrix in specimens with sparse particles, while it is still failure of bond elements to prevail in the specimens with denser particles.

## 4.2    Effect of particle density on the 3D lattice response

### 4.2.1    Model

A similar study as in the 2D lattice was conducted using the 3D lattice model. By analogy with the 2D case, the model used was a cube. In order to limit the computational time, the size of the cube was chosen imposing that the number of degrees of freedom of the 2D and 3D model was about the same, namely 201300, which corresponds to a 32x32x32 nodes 3D lattice, and 235179 elements. If the same cell size as in the 2D model would have been chosen ($s$=0.25 mm), the size of the cube would have resulted insufficient for inserting particles in it. For this reason it was decided to increase the size of the cell to $s$=0.75 mm, so that the final size of the cube became $B$=24 mm (see Figure 4.22). The boundary and loading conditions were the same as in the 2D case: the cube was clamped at the bottom and top and a vertical uniform displacement was imposed to the nodes of the top face.

A 3D random lattice with randomness $A/s$=0.001 was adopted in these analyses. In this case the average length of the beams was $l_{avr}$=0.95 mm. The height of the beam was chosen $h$=0.577 mm in analogy to previous 3D analyses ([57]), which corresponds to the ratio $h/l_{avr}$ for which the Poisson's ratio is independent of the randomness (see Figure 3.5). Note that the ratio $h/l_{avr}$ has about the same value in the 3D case and in the 2D case, which has been discussed in this chapter ($h/l \approx 6$).
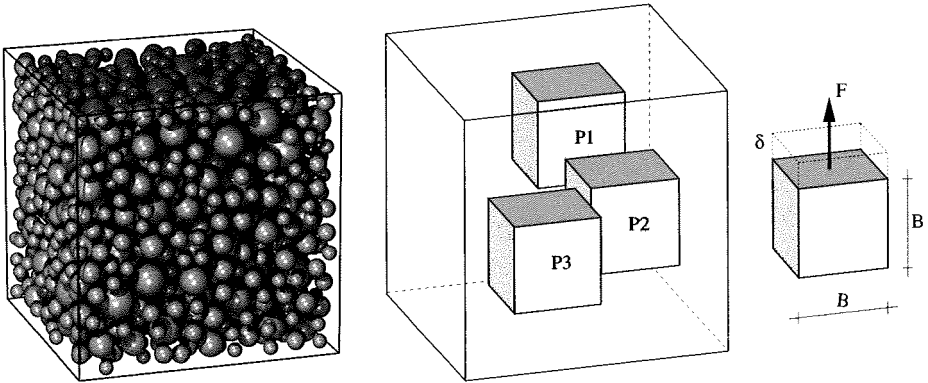


Figure 4.22: Model used for studying the effect of particle density in a 3D lattice.

In this case the smallest fractions of the particle distribution were disregarded, because these fractions could not be modelled in a lattice with the adopted beam length. Following the rule that the minimum diameter of the particles should be $l_{beam} \leq d_{a,min}/3$, a particle distribution with diameter in the range 4 mm-12 mm was chosen, with a sieve curve as shown in Figure 4.23. As in the 2D case, denser particle distributions were obtained by contracting an initially sparse distribution, which was contained in a cube of 72 mm size. For each particle density, the sample was positioned at a random position $P1$ in the
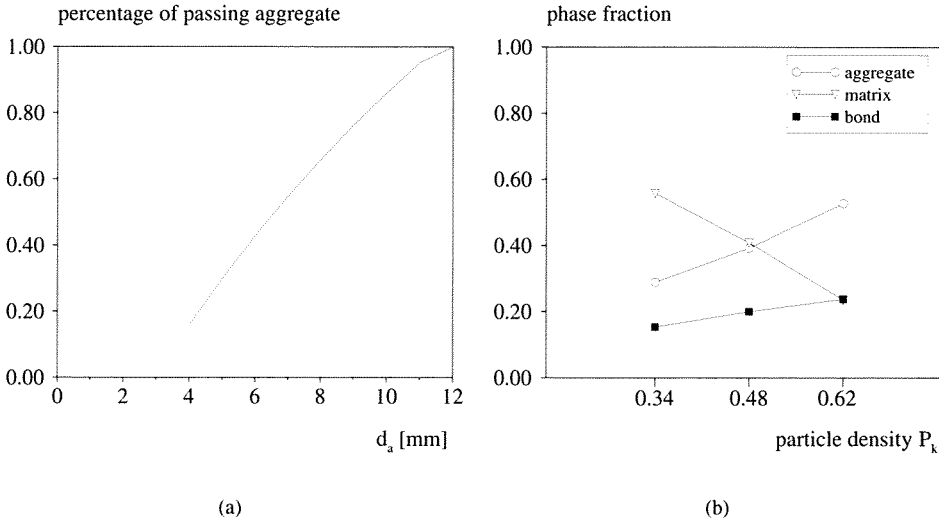
Figure 4.23: (a) Sieve curve of the 3D particle distribution. (b) Phase fractions in the 3D lattice versus particle density.

particle distribution, and, among all other random positions, two were chosen ($P2, P3$) with approximately the same number of aggregate beams as $P1$. The particle densities considered in the following are $P_k = 0.34, 0.48, 0.62$. The corresponding effective and lattice densities are reported in Table 4.2, which shows that the adopted lattice densities are similar to the lattice densities considered in the 2D study.

| $P_k$ | $P_{k,eff}$ | $P_{k,latt}$ |
|-------|-------------|--------------|
| 0.34 | 0.34 | 0.29 |
| 0.48 | 0.48 | 0.39 |
| 0.62 | 0.60 | 0.53 |

Table 4.2: Density of 3D aggregate lattice elements versus particle density.

The different phase fractions are represented in Figure 4.23(b).
The relative values of stiffness and strength assigned to the beams in the lattice are as in the 2D case, namely: $E_a/E_m = 70000/25000$, $E_b/E_m = 25000$, $f_{t,a}/f_{t,m} = 10/5$ and $f_{t,b}/f_{t,m} = 1.25/5$. Differently than in the 2D case, in the 3D case the contribution of the bending moment to the fracture criterion is neglected ($\alpha = 0$), in agreement with the results described in Chapter 2.

## 4.2.2    Results with different particle densities

**Pre-peak and peak regime**

The load-displacement diagrams obtained for different particle contents are shown in Figure 4.24(a). Also the scatter in results among the three specimens is indicated. The nominal strength is represented in Figure 4.24(b).



(a)                                                                    (b)
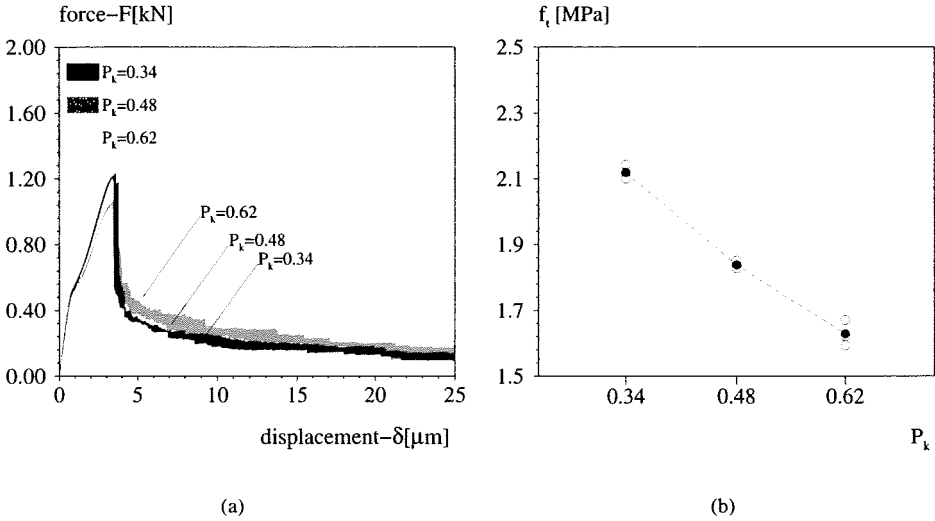
Figure 4.24: 3D lattice analyses with different particle densities. (a) Load-displacement diagrams. (b) Nominal strength versus particle density.

Already in the 2D analyses it was observed that the nominal strength decreases when the particle density increases. While in 2D an asymptotic value of the nominal strength was reached already at $P_k = 0.67$, in 3D the nominal strength decreases monotonically. Also the absolute values of the nominal strength in the 2D and 3D analyses differ, as the nominal strength in the 3D model is higher than in the 2D model. Another interesting difference between the 2D and 3D analysis is in the pre-peak regime. In the 2D analysis it was found that the load-displacement diagram was nearly linear until a high value of the load and, after it became non-linear, the peak load was reached relatively soon. Furthermore, only bond elements were failing in the pre-peak regime, and matrix elements started to fail only after the peak. The pre-peak behaviour is remarkably different in 3D, as the load-displacement diagram exhibits a kink. Also, failure of matrix elements starts already in the pre-peak.

(a) (b)
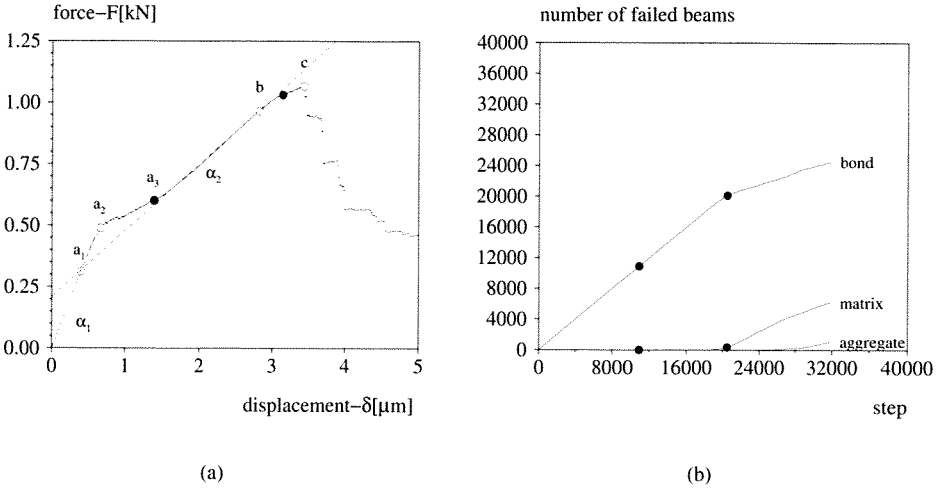
Figure 4.25: 3D lattice analysis of a specimen with particle density $P_k = 0.48$. (a) Detail of the load-displacement diagram in the pre-peak regime. (b) Number of failed beams versus number of steps.

This is illustraded in Figure 4.25(a), which shows the load-displacement diagram up to peak for a specimen with $P_k = 0.48$. Figure 4.25(b) also illustrates, for each phase, the number of beams failing versus the number of steps. In these diagrams the different loading stages are indicated with different letters:

$a_1$ indicates failure of the first beam. This occurs at a load which varies between 20% of the peak load for $P_k = 0.34$ up to 40% of the peak load for $P_k = 0.62$. After this point the load-displacement diagram remains linear, with slope $m_1 = tg\alpha_1$.

$a_2$ starting from $a_2$ the behaviour becomes highly non-linear. This occurs at a load level that is about 50% of the peak load.

$a_3$ in $a_3$ the diagram becomes linear again, with a slope $m_2 = tg\alpha_2 \leq m_1$. During this loading phase the first matrix beam fails, at about 60% of the peak load. Failure of the first matrix beam is indicated by the first of the two black dots in Figure 4.25. In this specific example failure of the first matrix beam and onset of the linear regime coincide.

$b$ in $b$ the non-linear regime which precedes the peak starts. In all specimens considered in the analyses this occurs at about 90% of the peak load. In the 2D analyses it was found that the extent of this non-linear part of the load-displacement diagram was depending on the particle density, while in 3D it does not. During the non-linear pre-peak regime also matrix elements start to fail extensively. The be-

ginning of such phenomenon is indicated in the diagram with the black dot located at $95 \div 99\%$ of the peak load.

$c$  identifies the peak load.
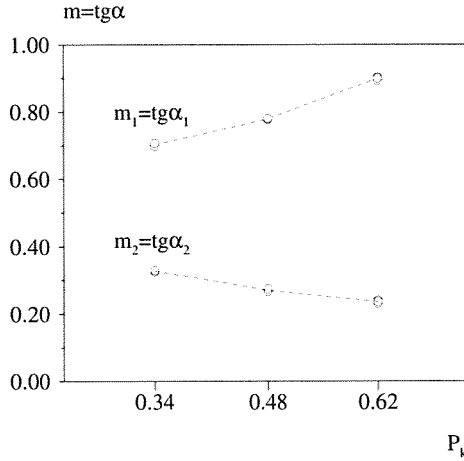


Figure 4.26: 3D lattice analyses with different particle densities. Slope of the load-displacement diagram in the pre-peak regime, see Figure 4.25(a).

It is interesting to observe that the variation of slope from $m_1$ to $m_2$ depends on the particle density. The larger the particle content, the higher is the initial slope, which is due to the bigger amount of stiffer elements. However, in the second of the two linear regimes, the slope becomes smaller when the particle content is larger. This is illustrated in Figure 4.26, which shows the variation of the slope $m$ versus the density of the particle content. For understanding the reason of the different behaviour it is necessary to analyze the crack pattern, as a different length or layout of the cracks can be expected when the particle density varies.

Visualization of cracks in 3D lattices is not straightforward. The method adopted here mimics the method used in impregnation technique: the specimen is sliced and cracks are visualized in each of the slices. The crack pattern at the onset of the first pre-peak non-linear regime (point $a_2$ in the load-displacement diagram) is represented in Figure 4.27 for two specimens with $P_k = 0.34$ and 0.62, respectively. The slices have been cut along the $Z$ direction and the cracks are shown at the faces and in the middle of the specimen, by indicating the beams that were removed, in white or in black depending if these elements are bond or matrix elements. At this level of load cracks are very sparse, as isolated bond elements fail everywhere in the specimen. Looking at more slices in the $Z$ direction as well as in the $X$ direction similar crack patterns as those shown in Figure 4.27 would still be observed. In the 2D analysis it has been observed that the way cracks distribute over the area of the specimen depends very much on the particle density: cracks are distributed

PK34_P1 – step 1296

PK62_P2 – step 984

Z=24 mm                    Z=12 mm                    Z=0 mm
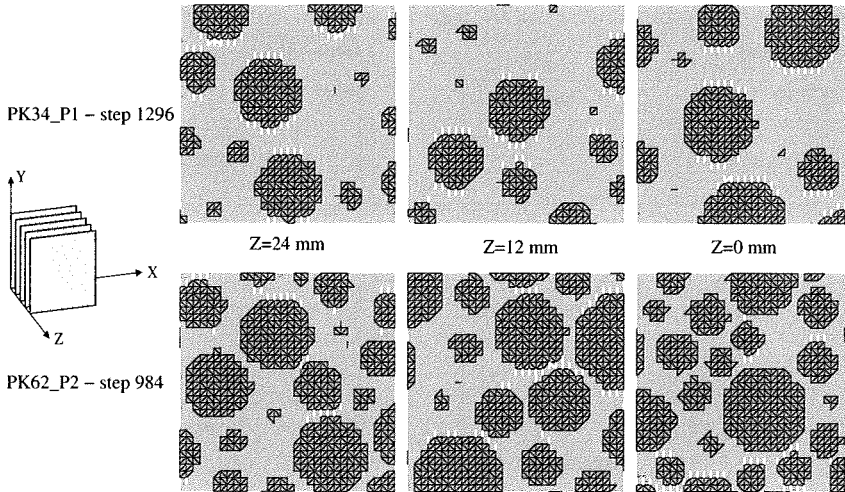
Figure 4.27: 3D lattice analyses with different particle densities. Crack patterns at the onset of the first pre-peak non-linear regime (point $a_2$ in Figure 4.25(a)) in specimens with $P_k = 0.34$ and $P_k = 0.62$.

in specimens with sparse particle density, while they form clusters in specimens with high particle density. Such difference is not observed in 3D. The different response of the 2D and 3D lattice could be induced by the different texture in the 2D and 3D specimens. In the 2D specimens the size of the largest aggregates was $1/5$ of the specimen size and the assigned particle density was reached by means of many particles with small diameter. In the 3D specimen the largest aggregate is $1/2$ of the specimen size and a similar density as in 2D is reached with a smaller number of big particles. To study how cracks develop during loading, the specimens $PK34\_P1$ and $PK62\_P2$ are considered as example. The load-displacement diagrams for these two specimens are shown in Figure 4.28. The crack patterns in the two specimens have been detected at three loading levels, namely at the points $a_3$, $b$ and $c$ of the load-displacement diagram, see Figure 4.25(a). Each specimen has been cut in 5 slices, first in the $Z$ direction, then in the $X$ direction. The cracks, detected on each slice, are shown in Figures 4.29, 4.30, 4.31. For a more clear visualization, all displacements have been amplified by factor 60. Though purely from a qualitative point of view, these pictures allow for some considerations:

- In the pre-peak regime cracks form around the particles. The length of these cracks depends on the size of the particles and on their mutual distance. On average, the particles in the 3D specimens are bigger than in 2D and also the cracks developing in the pre-peak regime are longer. Furthermore, due to the large size of the particles in comparison with the specimen, also the portion of the specimen which is damaged is larger in proportion. This might lead to the wrong conclusion that the nominal strength in 3D should be smaller. The third dimension plays here an
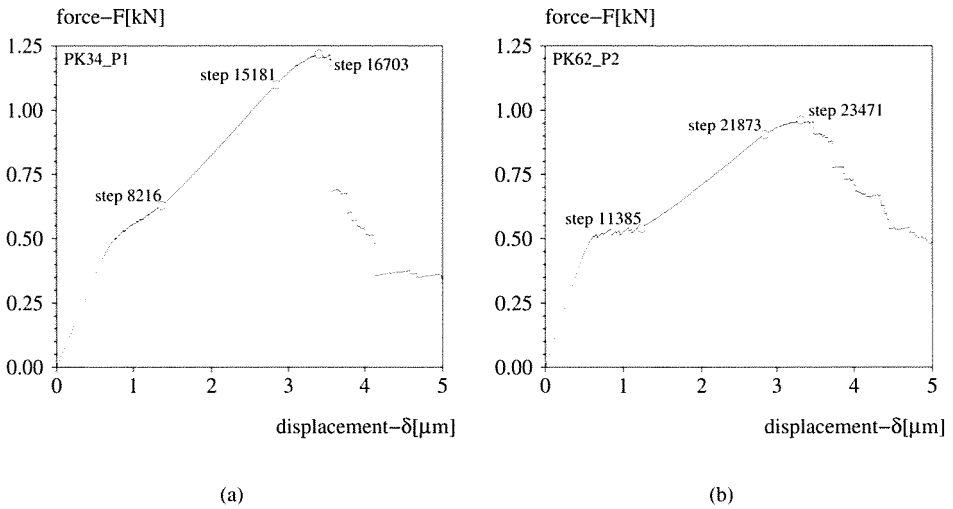
Figure 4.28:  3D lattice analyses with different particle densities.  Pre-peak load-displacement diagrams for specimens with (a) $P_k = 0.34$ and (b) $P_k = 0.62$.

essential role. Looking at the cracks it can be noticed that neighbouring cracks are still separated by intact links, though these are represented sometimes by one layer of beams only. However, this does not occur only on a plane, but in all directions. Therefore, if a crack on the plane normal to $Z$ is considered, it can be seen that this crack will penetrate only for a small extent into the depth of the specimen. However, many of these cracks can be found inside the specimen. This is also reflected in the details of the numerical simulation, because the number of steps necessary to break the specimens is in the order of 1000 in 2D, while in 3D is in the order of 10000.

- A comparison between the crack pattern in the specimens with different particle densities shows that, as a result of the smaller relative distance, cracks forming around neighbouring particles coalesce already in the early loading and longer cracks form in the specimens with denser particles. Also the number of cracks increases. This obviously affects the total stiffness of the specimen, which becomes softer as the particle density increases. In the load displacement diagram this affects both the kink and the second of the two linear regimes. The kink corresponds essentially to the formation of continuous cracks at the interface between particles and matrix. If the particle distribution is sparse, during this phase the specimen carries an increasing load while its deformation increases non proportionally, see Figure 4.28(a). However, if the particle distribution is dense, this part of the load-displacement diagram resembles a plateau, see Figure 4.28(b). The amount and

length of cracks has as effect also the reduction of the nominal strength. In 2D it was observed that the distribution of crack lengths was the same in the specimens with different particle density and it was only the way cracks were distributed over the specimen which determined the nominal strength. In this manner, in specimens with sparse particles also the cracks were sparse. On the contrary, in specimens with dense particles the cracks were localizing in some portions of the specimen, creating spots weaker than in the other specimens. Once again it should remarked that the 3D response, which differs in several aspects from the 2D lattice response, can be consequence of the specific model adopted in this study, and that the fracture behaviour would resemble more the 2D case when larger specimens with smaller lattice beams and a particle distribution including also small particles would be considered.

The presence of a kink in the pre-peak regime has not been detected in these analyses for the first time. Earlier 2D analyses showed that a similar kink could be obtained by reducing the bond strength [79]. Then, the kink was related to the fact that ...*if the bond strength is decreased, the onset of cracking takes place earlier, i.e. the point in the ascending branch where the curve starts to deviate from linearly is earlier.* It has already been mentioned that the kink corresponds to formation of continuous cracks around the particles after isolated beams fail sparsely in the specimen. Though, the reason for the formation of a second linear regime before the peak load is not clear. More insight in this can be obtained by comparing the crack patterns at the end of the first linear regime ($a_2$) and at the beginning of the second linear regime ($a_3$). An example is given in Figure 4.32 and 4.33 for the specimens $PK34\_P1$ and $PK62\_P2$, respectively. In both cases sections normal to the $Z$ axis have been considered. For comparing the crack patterns the elements removed between the two different loading levels have been drawn with a thicker line. These crack patterns show that still the weak bond elements surrounding the particles are the elements that fail during the second pre-peak linear regime. Either these are elements still intact after failure of adjacent elements (for example diagonal elements connected to elements that were earlier removed), or they are elements at the sides of particles that are already de-bonded at the top or at the bottom. Some elements can fail also in parts of the specimen not yet damaged, and in this case completely new cracks form. For example, this can be observed around the *small particles*. Speaking in this case of *small particles* means not necessarily particles of small diameter, but the portion of particle which is intersected by the plane on which the crack pattern is considered. In all cases it appears that the major cracks had already formed during the kink and, after the kink, no remarkable variation of crack length or crack density occurs to induce non-linearity in the load-displacement diagram. In Figure 4.32 and 4.33 also the elements failing during the non-linear regime immediately before the peak load have been shown. In this case elements fail at the ends of existing cracks or in the still intact material between adjacent particles. This indicates that cracks start to propagate into the matrix and indeed the percentage of matrix elements reaches up to 50% of the total number of elements failing during the non-linear pre-peak regime.
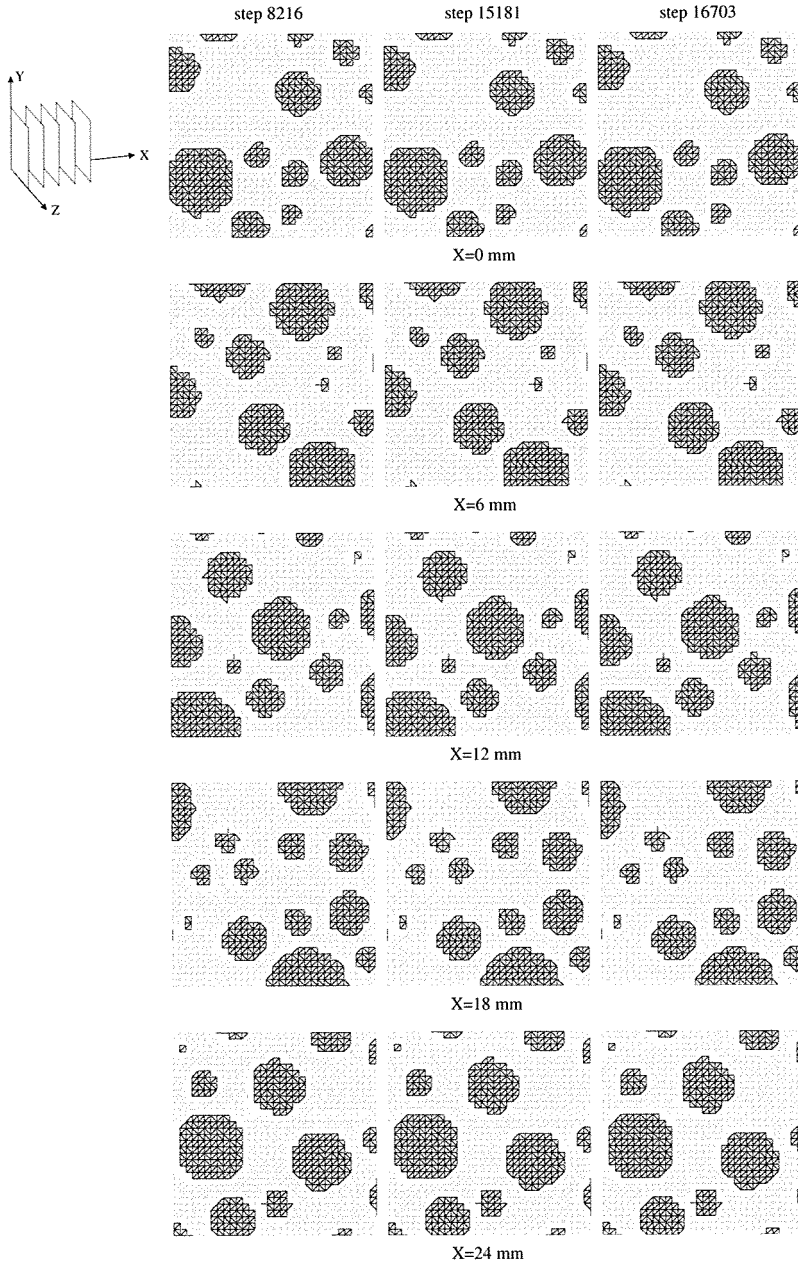
Figure 4.29: 3D lattice analyses of a specimen with $P_k = 0.34$. Crack patterns at different loading stages in the pre-peak regime, see Figure 4.28(a).
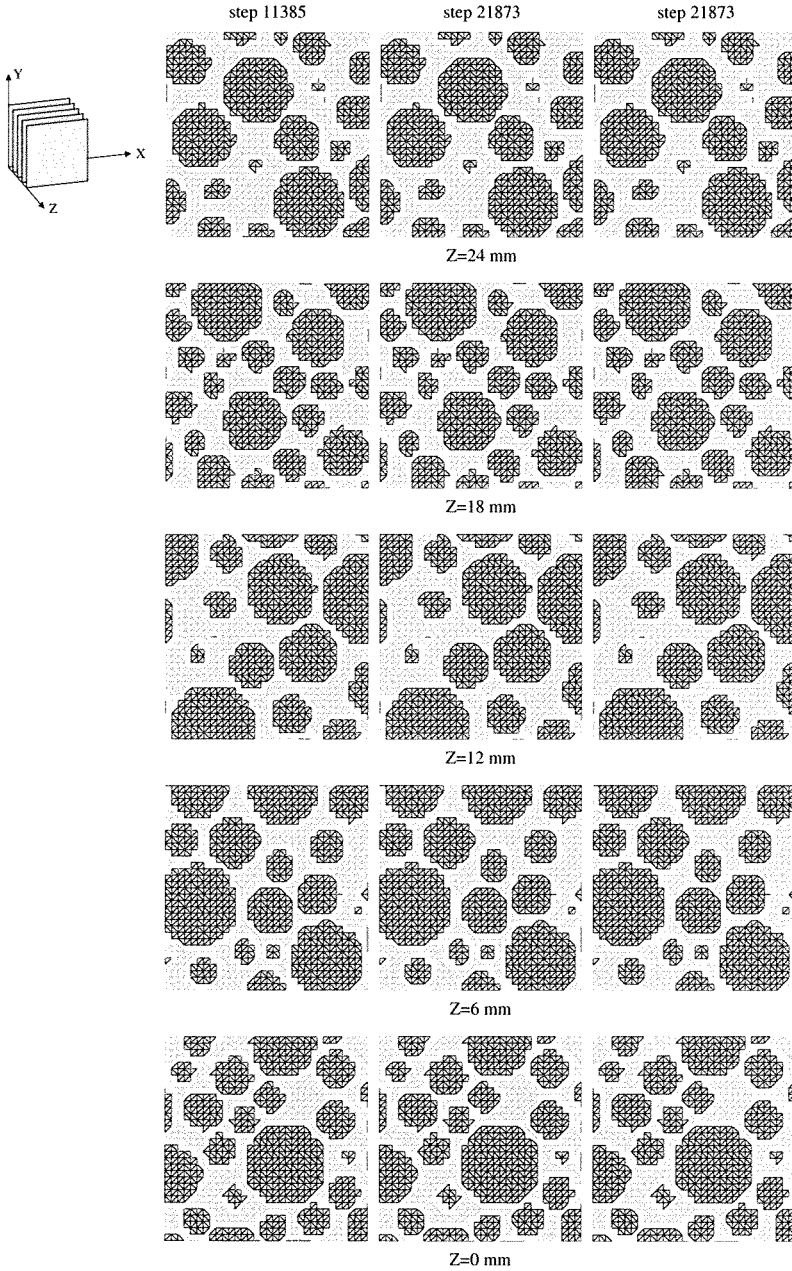
Figure 4.30: 3D lattice analyses of a specimen with $P_k = 0.62$. Crack patterns at different loading stages in the pre-peak regime, see Figure 4.28(b). The specimen is sliced along $Z$.
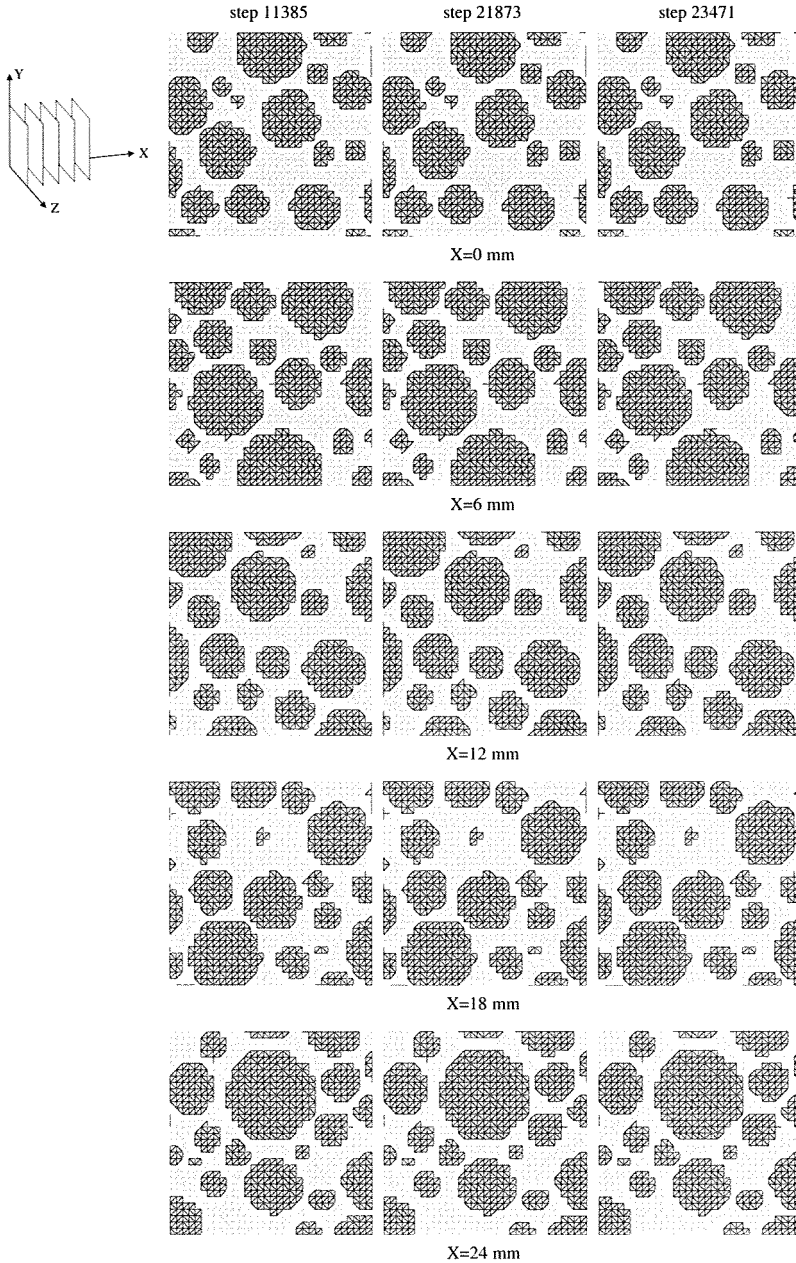
Figure 4.31: 3D lattice analyses of a specimen with $P_k = 0.62$. Crack patterns at different loading stages in the pre-peak regime, see Figure 4.28(b). The specimen is sliced along $X$.
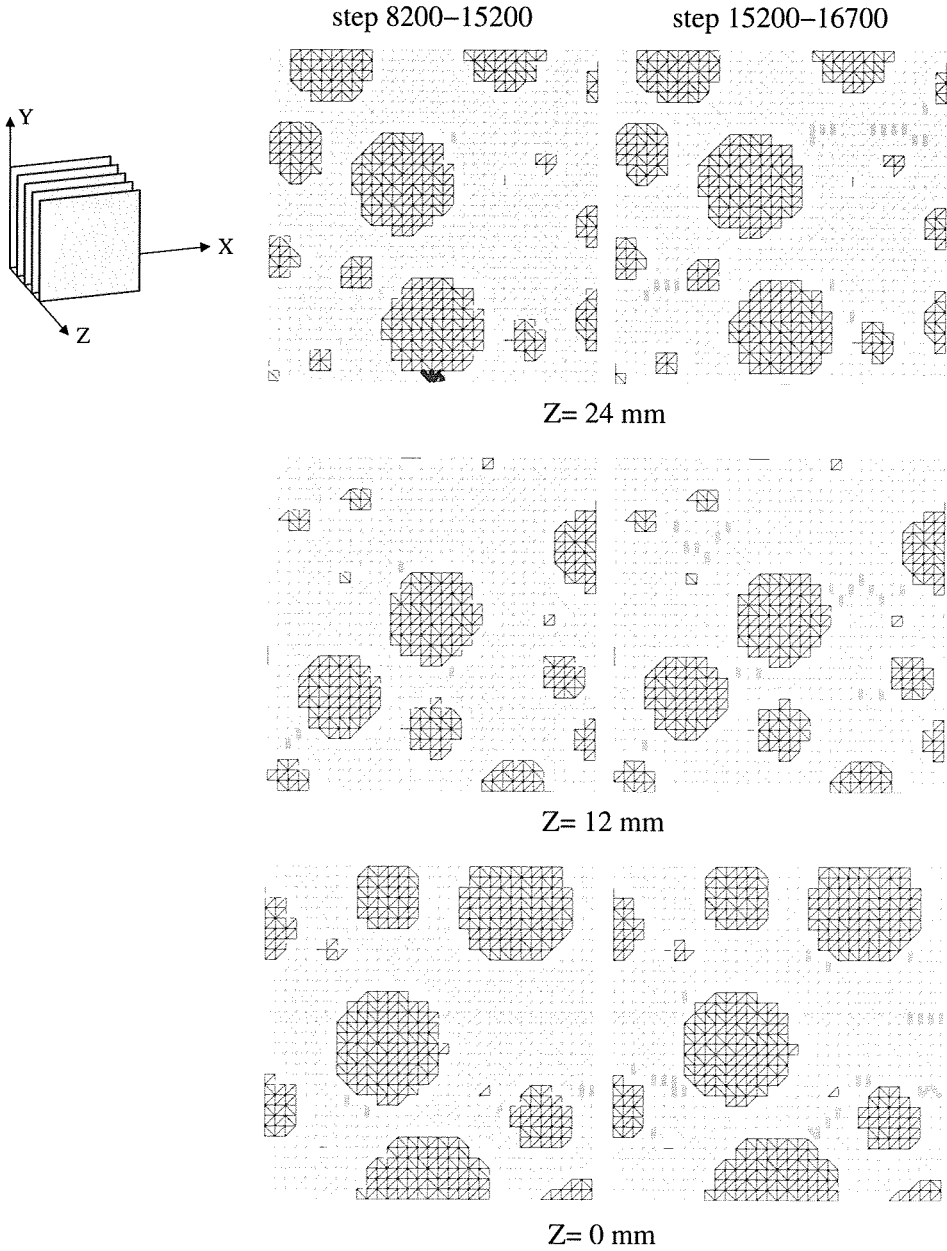
Figure 4.32: 3D lattice analysis of a specimen with $P_k = 0.34$. Crack formation (left) in the linear regime after the kink and (right) in the non-linear regime before the peak. The failed beams are represented with thicker lines.

Z=24 mm

Z=12 mm

Z=0 mm
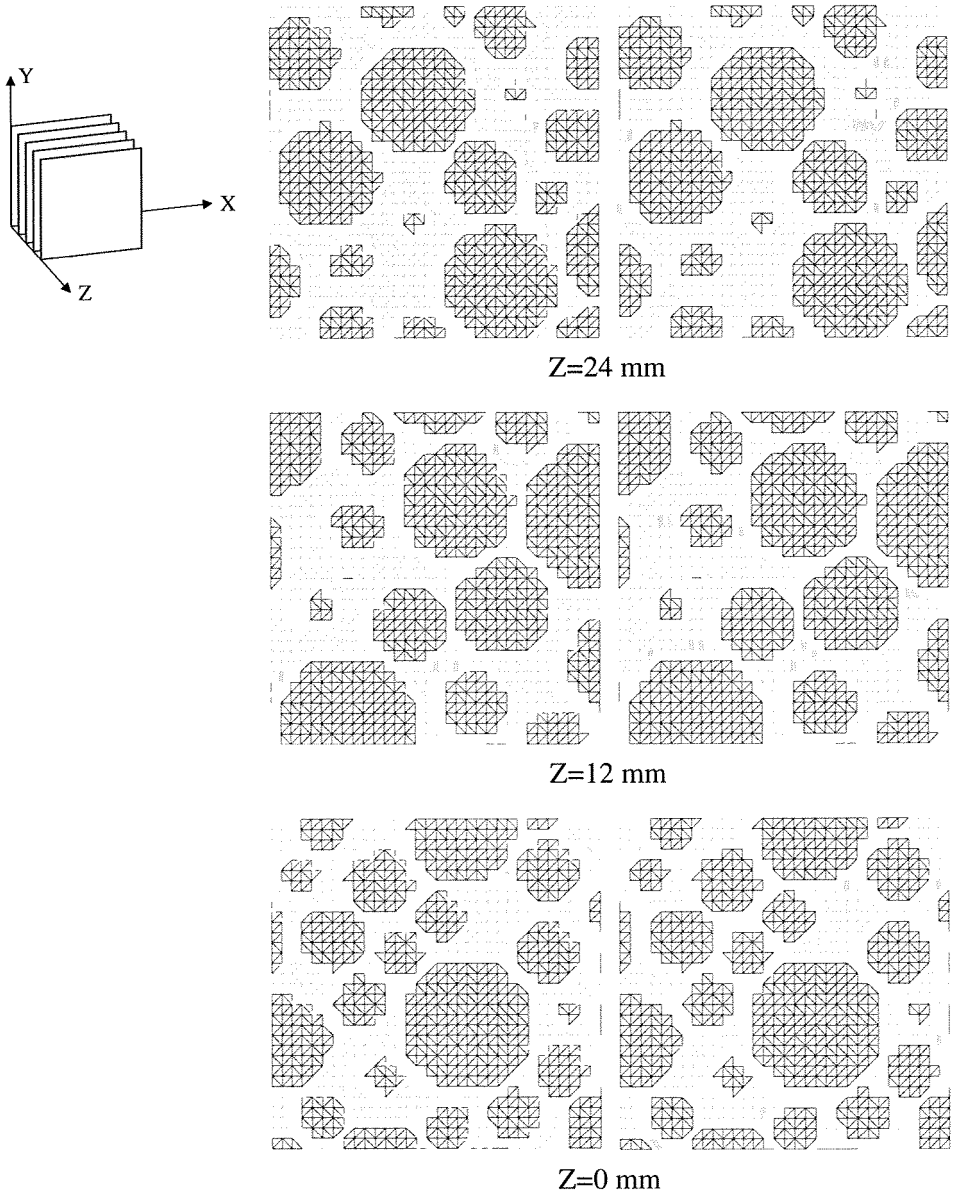
Figure 4.33: 3D lattice analysis of a specimen with $P_k = 0.62$. Crack formation (left) in the linear regime after the kink and (right) in the non-linear regime before the peak. The failed beams are represented with thicker line.

(a)

(b)
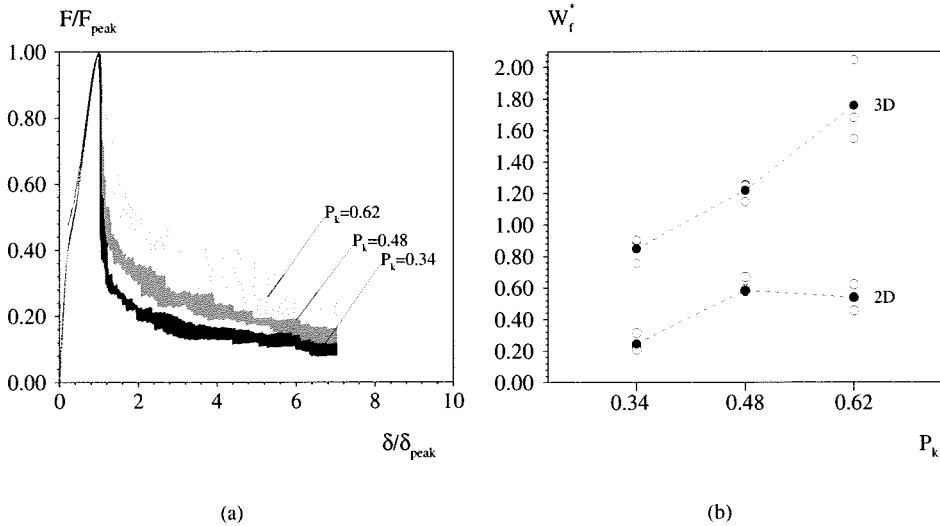
Figure 4.34: 3D lattice analyses with different particle densities. (a) Dimensionless load-displacement diagrams. (b)Comparison between 2D and 3D results: the diagram gives the area under the post-peak branch of the dimensionless load-displacement diagrams, $W_f^*$.

**Post-peak regime**

The most interesting 3D results are those obtained in the post-peak regime. The dimensionless load-displacement diagrams are shown in Figure 4.34(a) and the area under the post-peak branch of the dimensionless load-displacement diagram is shown in Figure 4.34(b), where 3D results are also compared with 2D results. Already in the 2D analyses it has been stressed that the *ductility* of the lattice response depends on the crack layout after the post-peak steep load drop. This is even more evident in the 3D analyses, which exhibit in general a more gradually descending post-peak branch than the 2D analyses, with a residual strength after the peak reaching values of 0.30-0.60, against 0.10-0.22 in the 2D analyses. As in the 2D analyses, the area under the post-peak branch of the dimesnionless load-displacement diagram increases with increasing particle density. For the nominal strength such increase is monotonic in 3D, while in 2D it shows even a slight decrease for the densest particle distribution. The 3D crack propagation is also in this case the key to understand the difference between 3D and 2D results. Two specimens of sparse and dense particle density (*PK34_P1* and *PK62_P1*) are considered as example. For each of the two specimens the crack patterns on sections normal to the Z axis have been drawn at different load levels (see Figure 4.36 and Figure 4.37). The first load level is at about half of the post-peak load drop. The second load level is at the end of the post-peak load drop. The other load levels correspond to a displacement $\delta$=10 mm

and $\delta$=25 mm, respectively. The corresponding points on the load-displacement diagrams are indicated in Figure 4.35.

To characterize the post-peak regime in the 3D analysis is not only the high ductility of the lattice response, but also the scatter in results, which depends on the particle density. The scatter is very small for the sparsest particle density and increases when the density of the particles increases. The small scatter in the specimens with low density of particles is surprising in itself. Given the small size of the specimen, and the relatively large size of the aggregates, a much larger scatter could be expected, as a consequence of the influence of the specimen's texture on its structural response. The explanation is to be found in the different crack layout.

In the specimens with the sparsest particle density failure is caused by one macro-crack which runs relatively straight through the specimen. If the particles are differently located, probably the crack will form in another position in the specimen but will remain still relatively straight, without significant branching, because of the large mutual distance among the particles. For this reason it can be expected that a different particle layout will not affect the corresponding load-displacement diagram, which will exhibit a small scatter. This can be observed in Figure 4.36. The major crack forms at the bottom of the specimen from coalescence of two macro-cracks that form during the post-peak load drop. Though the cracks run through the depth of the specimen, some intact links still prevent the specimen from failing. Even at a relatively large value of the displacement, $\delta$=25 mm, when the 2D specimens where practically broken, these intact links still allow the specimen to carry load.

In specimens with dense particle distributions, on the contrary, the scatter in results is very large. This is not surprising, as the crack pattern is in this case much more complex. The small inter-particle distance causes the formation of more macro-cracks during the post-peak load drop. Though the specimen is in this case more damaged, there are still intact links between the macro-cracks that preserve its bearing capacity. In this manner the specimen will have still a high residual strength after the peak. Furthermore, depending on the relative distance of the macro-cracks, bridging can occur in all directions with the result that the residual strength of the specimen is still relatively high even at large values of the displacement. This can be seen for example in Figure 4.37 which shows clearly two macro-cracks. The first macro-crack is in the top half, while the second is in the bottom half of the specimen. Though these cracks propagate through the depth of the specimen, bridging of large particles prevents them from coalescing in the middle of the specimen. As a result, the residual strength at $\delta$=25 mm is still about 0.20. However, if a different particle layout would be considered, the size of the bridge could be larger or smaller. This would affect the softening regime of the load-displacement diagram, resulting in a larger or smaller scatter of the results. To conclude, it is the relatively large size of the specimen in comparison with the particle size which produces the large scatter in the post-peak results in case of dense particle distributions.

Finally, to complete the comparison with the 2D analyses, it is necessary to look in which proportion beams belonging to different phases fail (see Figure 4.38). The first difference with the 2D results is in the total number of beams failing during each loading phase, namely up to peak, immediately after the peak, and in the tail of the softening regime. In

force−F[kN]

force−F[kN]

PK34_P1

PK62_P1

step 19994

step 26100

step 27815

step 22034

step 23628

step 32975

step 38722

step 25449

displacement−δ[μm]

displacement−δ[μm]

(a)

(b)
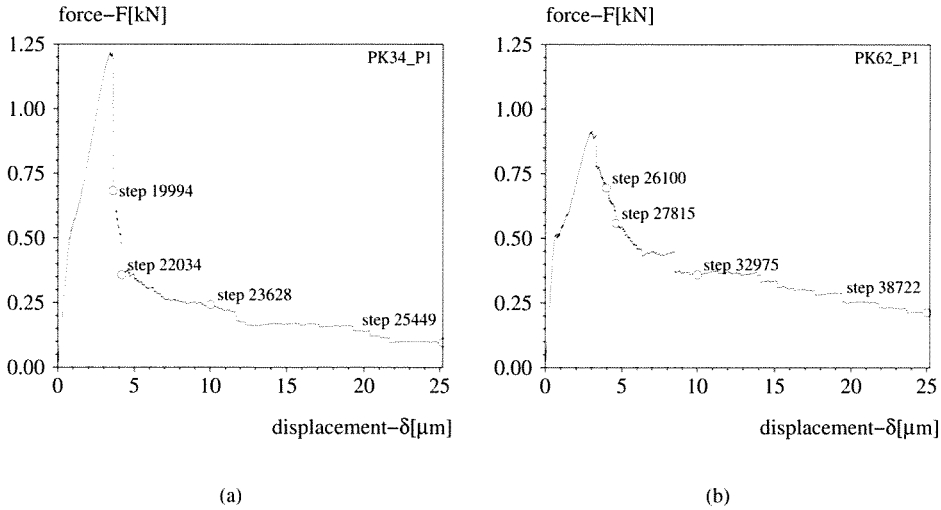
Figure 4.35: 3D lattice analyses with different particle densities. Load-displacement diagrams for the same specimens as in Figure 4.28: particle density (a) $P_k = 0.34$ and (b) $P_k = 0.62$.

2D no correlation was found with the particle density, while in 3D obviously the number of beams failing increases with the density of particles. It has previously been observed that the number of steps necessary to reach a certain load level is in 3D about ten times bigger than in 2D. This has also an effect on the load-displacement diagram, as this is much smoother in 3D. Also the fraction of failing beams is of interest. Though failure of bond elements is prevailing in the pre-peak regime, also matrix elements start to fail in the proximity of the peak load. In the drop after the peak, matrix or bond failure prevails, depending on the particle density: more matrix elements fail if the particle distribution is sparse, more bond elements fail in case of dense particles. The same happens in the tail of the softening regime. The role of bond failure in the post-peak regime is of major importance, as this corresponds to a more extensive crack branching/bridging of cracks and, as a consequence, to a more ductile structural response.
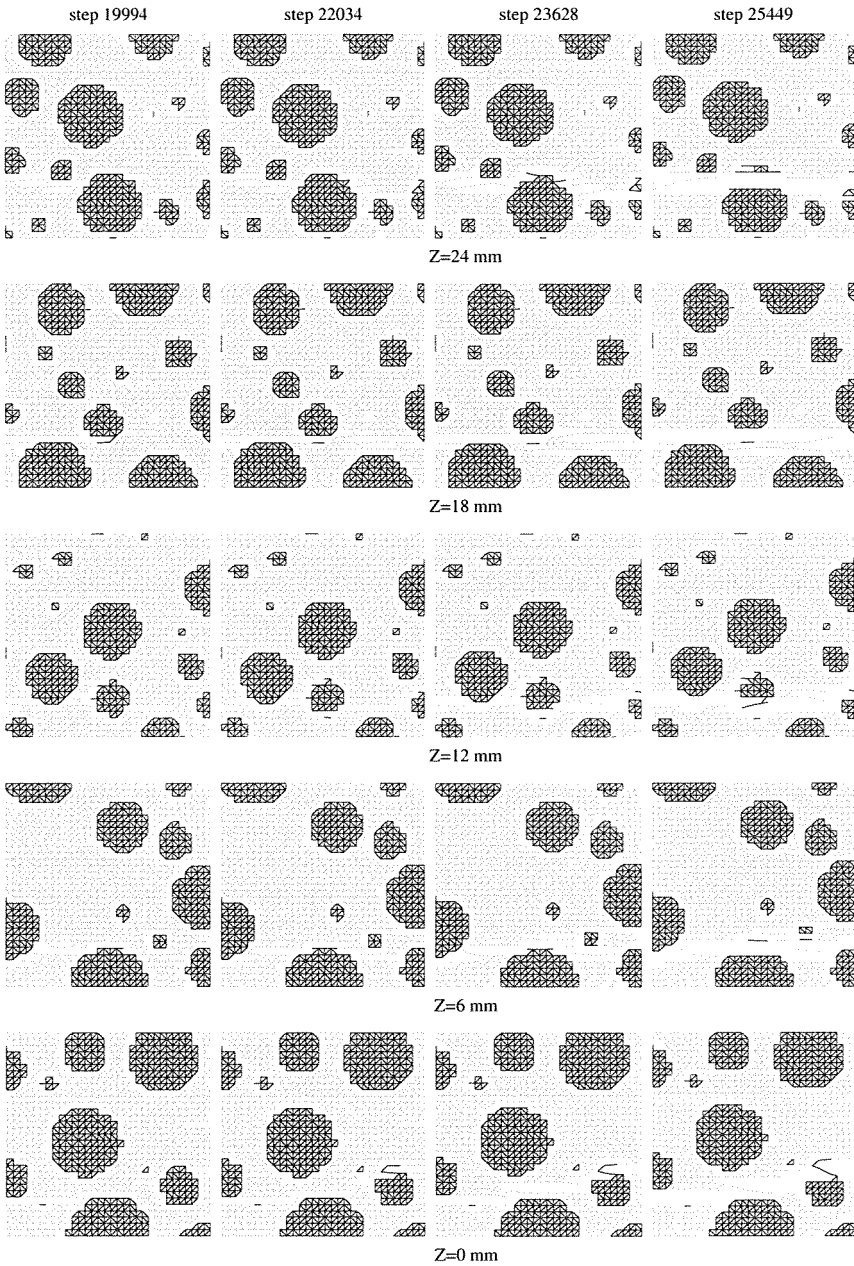
Figure 4.36: 3D lattice analyses of a specimen with $P_k = 0.34$. Crack patterns at different loading stages in the post-peak regime, see Figure 4.35(a).
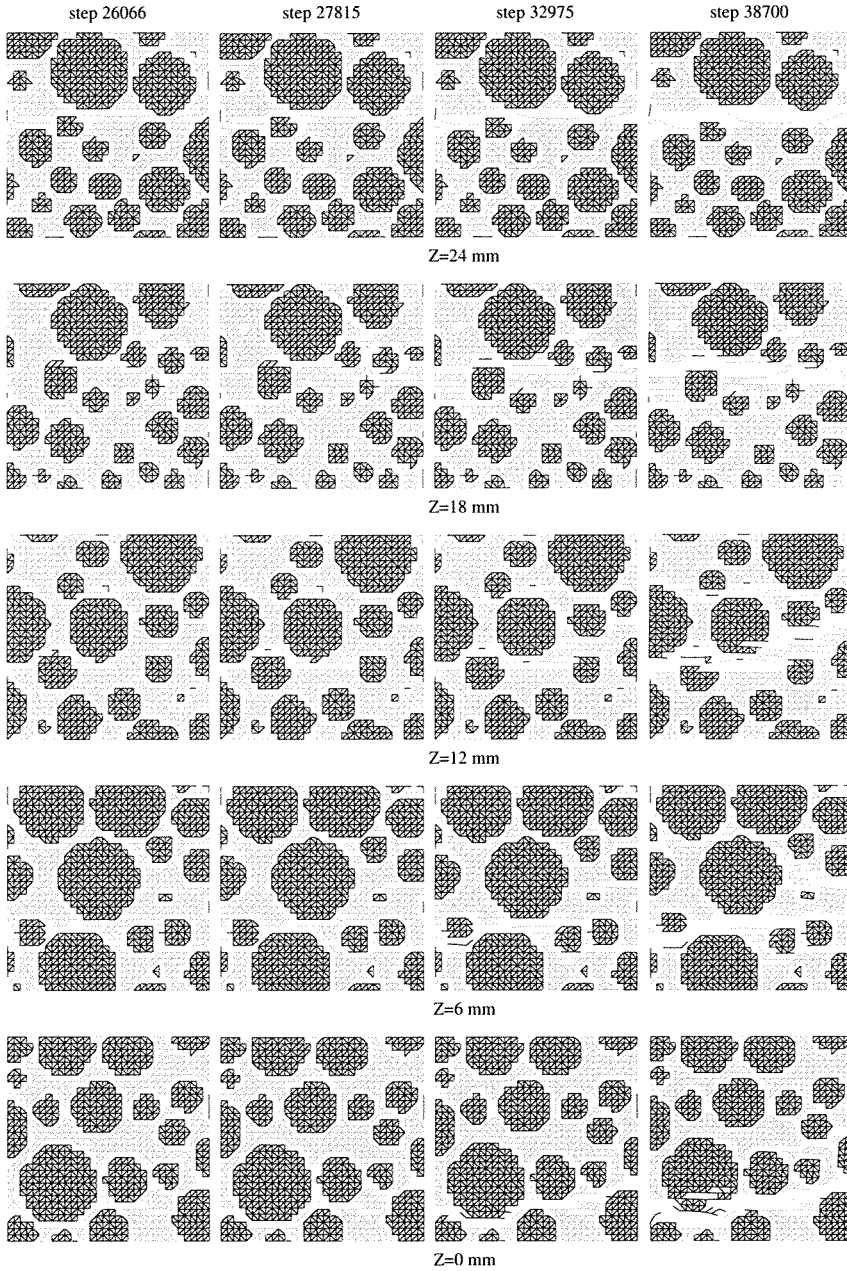
Figure 4.37: 3D lattice analyses of a specimen with $P_k = 0.62$. Crack patterns at different loading stages in the post-peak regime, see Figure 4.35(b).
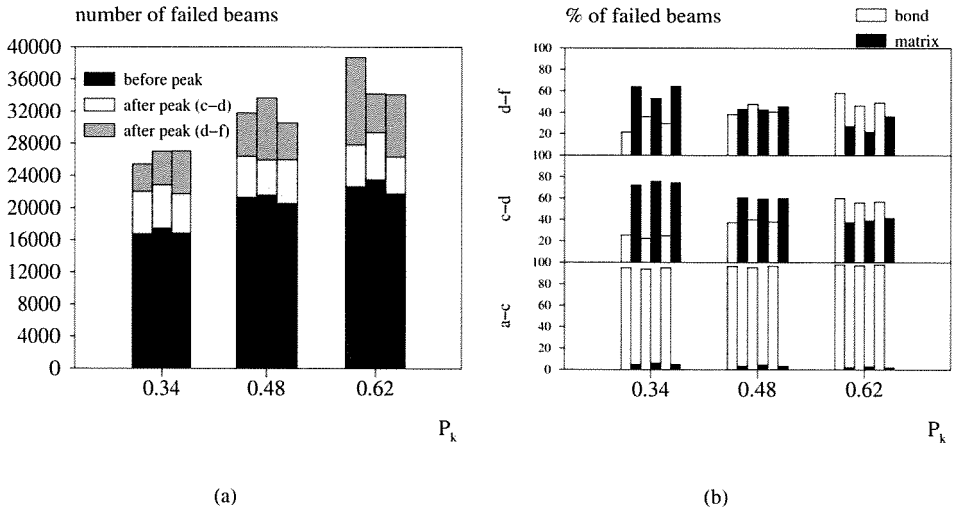
Figure 4.38: 3D lattice analyses with different particle densities. (a) Total number and (b) percentage of the number of beams that fail between different loading stages.

## 4.3   Experimental results

In literature not many articles are available with experimental results on effect of parti-cle content on fracture behaviour of concrete. A selection of articles on the subject has been listed at the beginning of this chapter; among these articles, the work of Amparano and Roth [1] reports results from experiments conducted on concrete beams subjected to three-point bending, with increasing volume fraction of aggregate in the range 0.45-0.75, and the volume of coarse aggregate twice the volume of fine aggregate. These results show that the compressive strength decreases with increasing volume fraction of aggre-gate. The explanation of this result is based on the ITZ: with higher aggregate content more interfaces form, and the strengthening effect of the aggregates is offset by the weak-ening effect of the interface. The fracture energy, computed using the size effect method [10], was found to decrease with an increasing aggregate content and reach a minimum value by $P_k = 0.65$, after which it starts to increase.

More experimental results were necessary for comparison with the numerical analyses. For this reason, laboratory experiments were designed using the cable tensile test set-up developed by van Mier and Shi [100]. In these experiments the load was applied via a cable which, having a low flexural stiffness, allowed the specimen to rotate freely at the ends. By varying the length of the cable a varying stiffness of the testing machine could be reproduced. Independently of the stiffness of the machine, stable crack propagation could be obtained by controlling the experiments with an appropriate feedback signal. The material used in these experiments was a *model concrete* made of mortar and glass
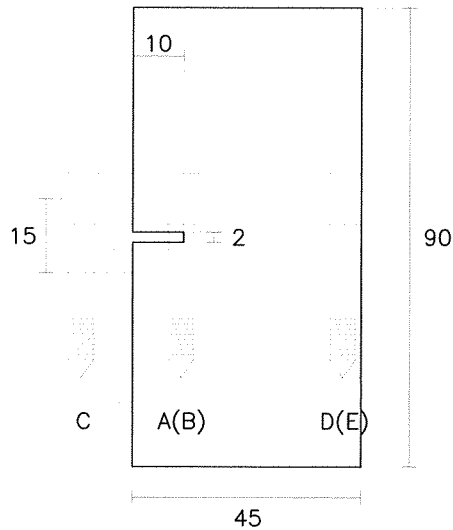
Figure 4.39: Geometry of the specimen and location of the LVDTs.

spheres. The glass spheres, of diameter $d_a$=1, 2, 4, 6 mm, were distributed according to a Fuller sieve curve. Three different mixtures were prepared, with volume fractions of the spheres $P_k = 0.30$, $0.45$, $0.60$, respectively. The specimens were prisms with 90 mm length, 45 mm width, 10 mm thickness, and a 10 mm depth notch (see Figure 4.39). The specimen was glued on platens that were connected to the frame through cables of 10 cm length. In this way the exact position of the load in the specimen was known throughout the test. In order to avoid out-of-plane eccentricities before crack onset, a special device was adopted to centre the specimen between the loading platens. The tests were conducted in displacement control, using the displacement measured with a LVDT placed over the notch (position C in Figure 4.39) in the close loop control. Four additional LVDTs were located on the surface of the specimen (see Figure 4.39) for measuring the relative displacement and rotation of the sections at each side of the specimen surface. A long distance optical microscope was used in some of the tensile tests in order to monitor the crack propagation. More details on these experiments can be found in [55]. Obviously these experiments do not form a basis for direct comparison with the numerical simulations, as the shape and size of the specimen, as well as the boundary conditions and the dimensions of the particles are different. However, the experiments conducted in the laboratory show a tendency similar to that of the numerical experiments, i.e. a decrease of the peak load and an increase in ductility, with increasing particle density.
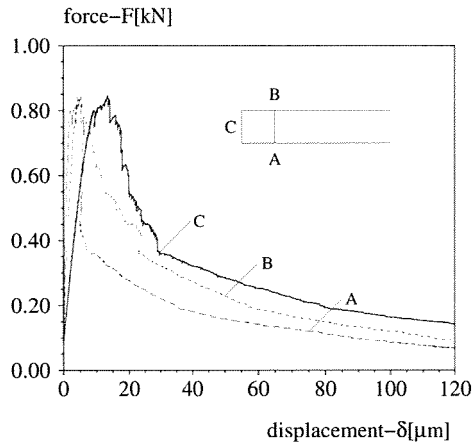
Figure 4.40: Experimental results. Load deformation diagrams for a specimen with 30% particle content. The curves give the deformations measured by the LVDTs located at the notch mouth, (C), and at the notch tip, (A) and (B).


## 4.3.1   Results

For each mixture at least three specimens were tested. In Figure 4.40 a typical load-deformation curve is presented. The curves give the displacements measured with the LVDT placed at the notch mouth (position C in Figure 4.39) and at the notch tip (positions A and B in Figure 4.39). The deformations of LVDT A and LVDT B are very similar until the peak load, since the transverse eccentricity is negligible. After the crack onset an out-of-plane rotation can be observed, which causes a 3D crack propagation.

The nominal strength was computed as ratio between the peak load and the area of the cross section (350 mm$^2$). Thus, the contribution of the bending moment resulting from the in-plane eccentricity induced by the presence of the notch at one side was not taken into account. Figure 4.41 shows the nominal strength computed for each of the specimens and, for each particle content, the corresponding average value (black dots connected by the dashed line). The results show that the average nominal strength decreases with increasing content of glass spheres. Results obtained from one test on specimens with $P_k = 0.30$ and 0.60, respectively, are plotted in Figure 4.42(a). The corresponding dimensionless diagrams, where load and deformation are divided by the values at the peak, are shown in Figure 4.42(b). These diagrams display a more brittle behaviour of the mix with $P_k = 0.30$, which exhibits a post-peak branch lower than the mix with $P_k = 0.60$. The crack pattern detected at the microscope in a specimen with $P_k = 0.45$, at 65 $\mu m$ deformation, is depicted in Figure 4.43. Such figure shows a mosaic of the images taken with the microscope, containing each 768x512 pixels. Normally the crack became visible only after a displacement of 25 $\mu m$, which corresponds approximately to the end of the steep branch in the softening regime. At this stage a relatively long macro-crack appeared to
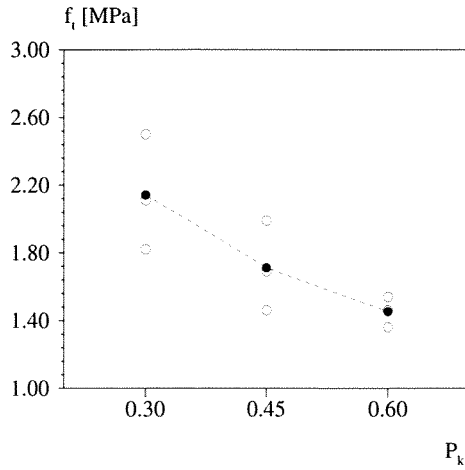
Figure 4.41: Experimental results. Nominal strength versus particle content.



(a)

(b)
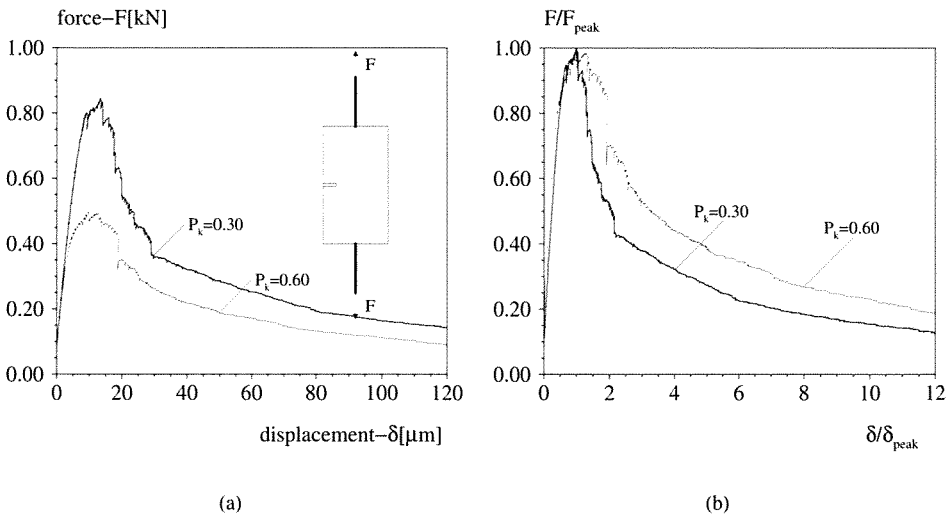
Figure 4.42: Experimental results. Load displacement diagrams for specimens with different particle content: (a) absolute and (b) dimensionless values.
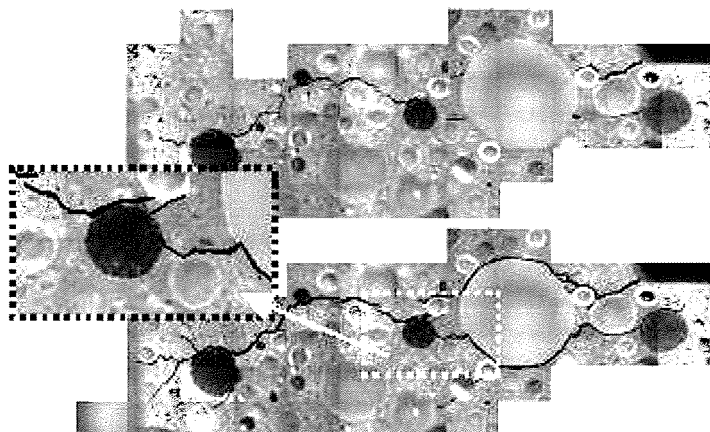
Figure 4.43: Experimental results. Crack pattern at 65 $\mu$m displacement in a specimen with 45% particle content. The crack pattern is filtered after (upper) and before (lower) creation of the mosaic.

have propagated from a corner of the notch to the opposite side of the specimen (see Figure 4.43). The crack path showed a tendency to bend around the aggregates, propagating in the plane of the specimen surface if the sawed bead was bigger than half a sphere, or in the transversal plane if the bead was smaller, as schematically represented in Figure 4.44. As an example, Figure 4.43 shows the occurrence of such phenomenon when the crack encounters a big grain near the notch. In this case, however, the initial part of the crack is double-branched. It is questionable whether the crack indeed branches or, rather, a second, isolated crack is present. The latter possibility seems to be confirmed by the inset in Figure 4.43, which displays two cracks that are bridged by the grain. However, the opening of such cracks at the upper and bottom side of the grain is negligible in comparison with the opening of the main crack(s). As a matter of fact, these cracks could be detected only after magnification of the mosaic of images. Thus, the conclusion may be drawn that only one macro-crack was present, which developed and opened not uniformly along the thickness of the specimen, due to presence of the grain. Such crack passes indeed behind the grain and the de-bonding cracks that appear on the surface of the specimen are a result of 3D bridging. The images taken with the microscope show that the main crack does not propagate from a particle to an adjacent one following a straight path in the matrix, but deviates towards neighbouring particles, like shown in the detail of Figure 4.43. In fact, the crack is attracted to the locations with lower strength (ITZ), where high stress concentrations occur due to the relatively high stiffness of the aggregate in comparison with the matrix. As a result, the crack pattern is more or less tortuous, depending on the bond and matrix strength and stiffness, as well as aggregate dimension and content.
The experimental results show the same trend as the numerical analyses. Though, validation of the 3D lattice analysis requires more extensive laboratory experiments. A problem
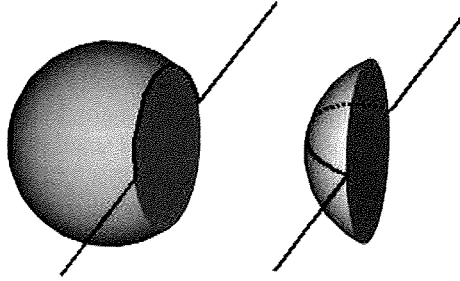
Figure 4.44: Crack propagation in the plane of the specimen surface and in the transversal plane.

encountered in the experiments is that it was impossible to achieve the same workability in specimens with different particle content, as consequence of the different specific surface of the aggregates. As a consequence, also the strength of the matrix was not constant in all specimens. This makes difficult to give an objective interpretation of the experimental results, and to isolate the effect of the particle density, especially in the specimens with high particle content.

## 4.4 Concluding remarks

The fracture behaviour of a heterogeneous material such as concrete depends on the properties of its constituents and on their interaction. In normal strength concrete the strength of the system matrix-ITZ governs the strength of the whole material. Being the weaker component in the system, the ITZ plays a significant role in the fracture mechanisms of concrete. The amount of ITZ present in concrete depends, among others, on the content of particles. For an assigned composition of the particle distribution and thickness of the ITZ, the volume of ITZ can be increased by increasing the total volume of particles contained in a unit volume, namely by increasing the particle density.
The effect of increasing particle density has been studied in this chapter using a 2D and a 3D lattice. The numerical results, validated by experiments, indicate that:

- the nominal strength decreases with increasing particle density;

- the *ductility* increases with increasing particle density.

Both in the 2D and 3D lattice analyses the fracture process exhibits three distinct phases:

- de-bonding in the pre-peak regime;

- crack propagation through the matrix in the regime immediately after the peak, which causes coalescence of micro-cracks and formation of macro-cracks;

- crack bridging in the tail of the softening regime.

The nominal strength, as well as the ductility of the fracture response, is a result of the crack details.

In the 2D analyses the pre-peak cracks are uniformly distributed over the surface of the specimen if the particle distribution is sparse; if the particle distribution is dense then cracks localize in a small region of the specimen, at a small mutual distance which depends on the inter-particle distance. The effect of the localization is to weaken the specimen, which will exhibit a lower strength than the specimens where the damage is distributed. In the 3D analysis the amount of cracks rather than their spatial distribution determines the strength of the specimen. Due to the larger number of particles, more cracks form in the pre-peak regime in the specimens with a dense particle distribution. Furthermore, as in these specimens the inter-particle distance is smaller, longer cracks can form by coalescence of neighbouring small cracks.

The post-peak response in the 2D as well as in the 3D analyses is governed by the tortuosity of the crack patterns. In specimens with sparse particles macro-cracks can propagate straight. One or a few straight cracks will suffice to bring the specimen to failure, requiring for this a relatively small energy supply. In specimens with high particle content the particles function as crack arrestors. As a result more macro-cracks form, which are bridged by the particles. In this case failure of the specimen occurs when all bridges break, which requires a higher energy supply.

Though qualitatively similar, the 2D and 3D analyses differ in the following aspects:

- The 3D analyses show not only a higher nominal strength, but also a much higher *ductility* than the 2D analyses.
  The 3D crack propagation is essential to explain the difference between 2D and 3D analyses. In the 2D analyses crack(s) propagate through the depth of the specimen at one step and only in-plane bridging is possible. In the 3D analyses, on the contrary, cracks propagate and are arrested by particles in all directions. The result is that bridging occurs also along the depth of the structure. As a consequence, not only the nominal strength but also the ductility increases.

- In the 3D analyses the variation of the nominal strength and *ductility* with the particle density is monotonic while in 2D an asymptot is reached.
  When the density of the particle distribution is increased, continuous paths of bond elements can form. This is known as *percolation* of the bond phase. The complementary situation of percolated matrix can be obtained removing the ITZ. Both these conditions will be analyzed in detail in the next chapter. It is worth to anticipate that if percolation occurs, neither the nominal strength nor the ductility will be affected by the particle density. The different behaviour of the 2D and the 3D lattice indicates that bond is percolated in the 2D specimens with denser particle distribution but not in the 3D specimens.

Finally it should be remarked that the details of the numerical analyses can have contributed to the different response of the 2D and 3D lattice. In the 2D specimens the particle distribution includes the smallest fractions and the size of the specimen is $\approx 5$ times

the size of the biggest particle; in the 3D specimens, only for computational reasons, the smallest particle fractions have been removed and the size of the specimen is $\approx 2$ times the diameter of the biggest particle. A more objective comparison between the 3D and 2D lattice should be made assigning to the 3D lattice similar characteristics as the 2D lattice (same beam length, same grading of particles). The only limitation to this is imposed by the limited computer capacity.

# Chapter 5

# Effect of the ITZ on the fracture mechanism

The existence of an *auréole de transition* around the aggregates, with a different mineralogy and micro-structure than the cement paste, was for the first time recognized in 1956 [32]. Since then many researchers have studied the interfacial transition zone (ITZ) and, though the mechanisms of formation are not yet completely clear, it is generally accepted that the ITZ is a very porous and weak shell up to 100 $\mu$m thick, whose properties vary gradually from the inner to the outer boundary until merging with those of the bulk cement paste. Optical microscopy observations conducted on model systems as well as on real concrete show that the poor physical and mechanical properties of the ITZ are induced by: deficient content of cement particles due to *wall effect* [34]; high content of preferentially oriented calcium hydroxide crystals [47], that exhibit a low strength between cleavage planes, and of ettringite; low content of calcium silicate hydrates [15, 114]. It is known that pozzolanic materials like silica fume and fly ash improve the properties of the ITZ. The effect of such materials is both physical and chemical: micro-filling due to the small size of the particles, and pozzolanic reaction both contribute to a denser and stronger micro-structure of the ITZ. Also the precipitation of calcium hydroxide crystals and their preferential orientation seem to be affected by silica fume and fly ash [61, 78, 70, 37, 22]. Not only the cementitious matrix, but also the aggregate geochemistry plays a role in the formation of the ITZ [93]. Physical interaction between aggregates and cement paste is also important. An example is given by the different strength of the ITZ in lightweight aggregates, which depends on the absorption capacity of the aggregates [107].

Besides the relative difference in properties between ITZ and bulk paste, another parameter leading to different physical and mechanical properties of concrete is the volume fraction and connectivity of the ITZ regions (percolation) [89]. The effect of increasing volume of ITZ has already been investigated in Chapter 4, where the amount of interfacial zone was increased by increasing the particle volume. In this chapter, the variation of ITZ volume is obtained by varying the thickness of the ITZ, for a given particle density. The

85

effect of interface strength and stiffness are also studied.

# 5.1   Effect of the ITZ thickness

## 5.1.1   Model

The model used for studying the effect of the ITZ thickness is the same 2D lattice as described in Chapter 4, with particle density $P_k = 0.35$. In this model the ITZ is enlarged by increasing the diameter of each particle in steps of 0.25 mm. Each time, a layer of bond elements is defined according to the procedure described in Chapter 2, and added to the layer of bond elements found in the previous step. In this manner the ITZ is sequentially enlarged from one to more layers of lattice elements, as depicted in Figure 5.1.



    (a)               (b)               (c)               (d)
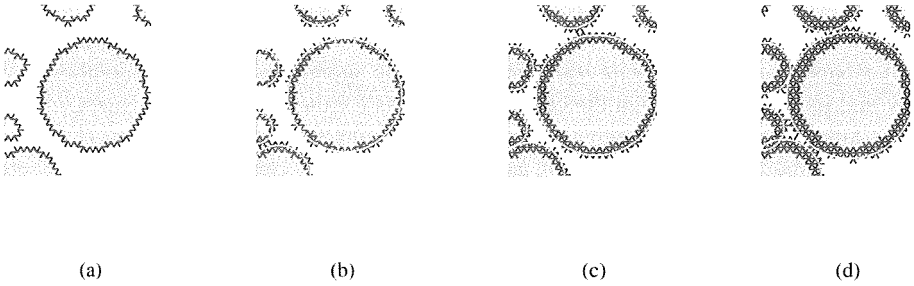
Figure 5.1: Model used for studying the effect of the ITZ thickness (2D lattice). (a) The original ITZ thickness is 0.25 mm. The ITZ region is enlarged by increasing the initial diameter of the particles by: (b) 0.25 mm, (c) 0.50 mm, (d) 0.75 mm.

Due to this type of construction, the thickness of the ITZ is not uniform around the aggregates, as probably is also in reality. For example, when the particle diameter is increased by 1 mm, see Figure 5.1(d), the layers of bond elements are only three in the radial direction, while there are four layers in the horizontal direction. In the sequel ITZ thickness will be meant as the maximum thickness. By increasing the ITZ thickness, continuous paths of ITZ elements can form, as shown in Figure 5.1. The different phase fractions corresponding to each ITZ thickness (maximum value) are represented in Figure 5.2, which shows that for a thickness of 1 mm the volume of bond and matrix elements is almost the same. The fractions indicated in this diagram are those obtained after overlaying of the lattice, therefore the aggregate density is lower than $P_k=0.35$ (see Chapter 2). For each ITZ thickness, analyses were conducted on three different specimens, for a total of 12 numerical experiments, that include the analyses already reported in Chapter 4, where the ITZ thickness was kept constant (ITZ=0.25 mm).
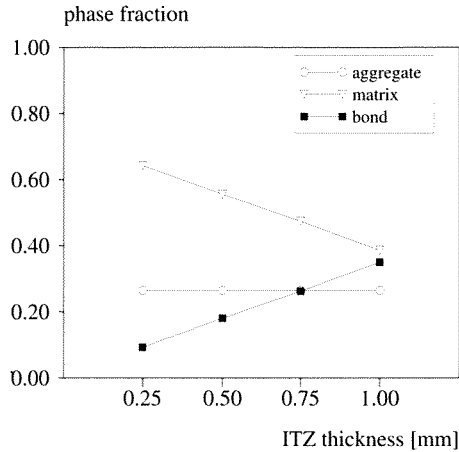
phase fraction



Figure 5.2: Phase fractions versus ITZ thickness.

## 5.1.2   Results

**Pre-peak and peak regime**

The load-displacement diagrams obtained for each interface thickness, and the scatter among the three different numerical experiments are represented in Figure 5.3(a). In black is the diagram obtained for a thickness of 0.25 mm; the other diagrams are represented in a gradation of grey which is lighter as the thickness of the interface increases. The nominal strength, obtained dividing the load at the peak by the area of the cross section of the specimen, is represented in Figure 5.3(b).

The load-displacement diagrams show quite a sharp peak for thick interfaces. In the analyses with only one layer of interface elements (see Chapter 4) the peak is preceded by a non-linear regime, whose extension depends on the distribution of micro-cracks, which can be sparse or locally concentrated in the specimen. In the specimens with sparsest particle distribution (that are those considered in the analyses with varying ITZ thickness), the non-linear regime begins at about 90% of the peak load, while the first lattice beam fails at about 70% of the peak load. When the interface becomes thicker, the first lattice beam fails at an average value of 90% of the peak load and, even when the first failure occurs at lower loading levels (75% in the last of the three specimens, for example), the load-displacement diagram remains straight up to the peak. Furthermore, only a few steps are necessary to reach the peak load. This can be concluded from Figure 5.4(b), where, for each of the twelve specimens, the number of beams failed at the peak is represented. In this figure a logarithmic scale has been adopted because the number of failed elements ranges from thousands in the specimen with only one layer of ITZ elements down to about ten in the specimens with thicker interface. As no aggregate beams fail up to peak, only the matrix and the bond phases have been considered. The bond phase is in turn
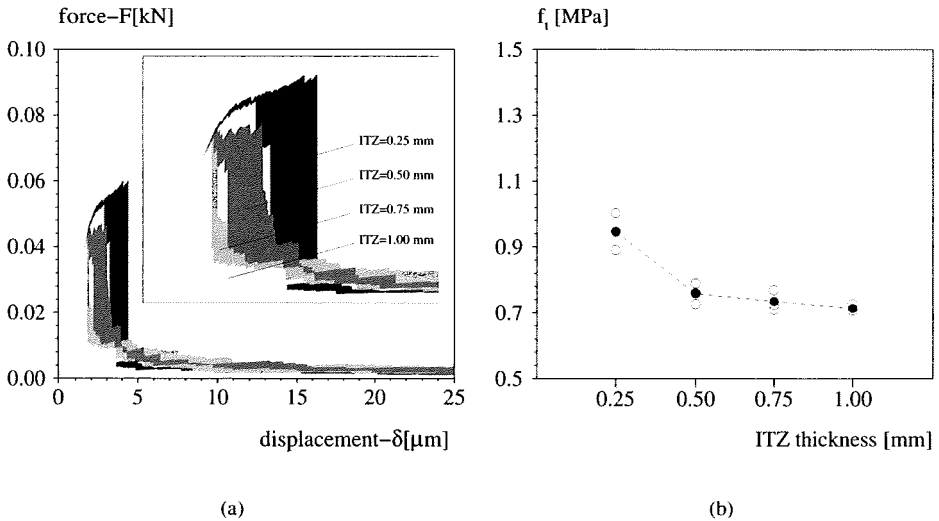
Figure 5.3: 2D lattice analyses with different ITZ thickness. (a) Load-displacement diagrams. (b) Nominal strength versus ITZ thickness.

divided into *inner* and *outer* bond elements, as described in Figure 5.4(a). In Chapter 4 it was stressed that the characteristic phenomenon of the pre-peak regime is aggregate de-bonding. Failure of bond elements prevails in the pre-peak regime also when the ITZ thickness is increased. However, in this case failure occurs not necessarily in the inner layer of the ITZ. As a matter of fact, failure in the outer layer proceeds simultaneously with failure in the inner layer, and the total number of beams failing, which belong to each of the two sub-phases, is at the end comparable, see Figure 5.4(b). This forces to reconsider the role that the relative stiffness of aggregate and bond/matrix plays in the onset of cracks in the pre-peak regime. Due to the different stiffness between aggregate and bond elements, it could have been expected that the stress concentrations at the edge of the aggregates induce first an extensive failure of bond elements in the inner part of the ITZ, before propagating towards the outer part and then in the matrix. The fact that this does not happen suggests that the low strength of the ITZ plays the major role as crack trigger in the pre-peak. However, as the circumference of the particle is not nicely round, there can be fluctuations in the stress distribution around the particles. The direction of the lattice elements can have an influence too, which might drive first fractures away from the immediate interface.

It has already been mentioned that in the specimens with a thick interface only a few steps suffice to reach the peak load. A typical example of crack patterns at peak is given in Figure 5.5. The arrow in Figure 5.5(b) points to the position where the macro-crack will form. The crack pattern in Figure 5.5(a) is the only case among all those analyzed

(a)                                                            (b)
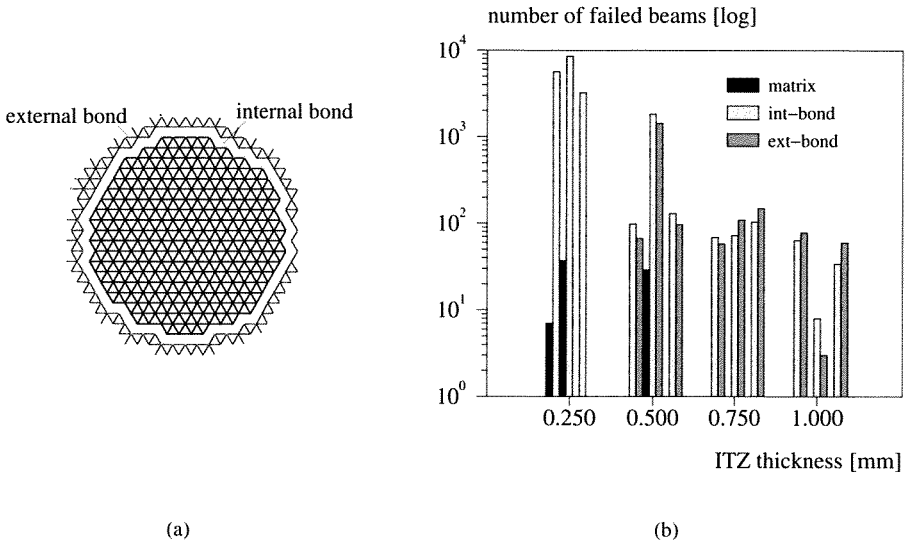
Figure 5.4: 2D lattice analyses with different ITZ thickness. (a) Layout of the different phases in the 2D lattice with thick ITZ: outer layers of bond elements are added to the original, inner layer. (b) Number of beams failing in the pre-peak regime.

where extensive pre-peak cracking occurs in a specimen with *thick* interface. The fact that when the thickness of the ITZ is doubled (from 0.25 mm to 0.50 mm) the peak load is reached sooner implies that also a lower nominal strength can be developed in these specimens. However, if the ITZ becomes more than twice thicker, the nominal strength remains constant. This indicates that the crack mechanism does not change any longer after a certain critical value of the interface thickness. An asymptotic value of the nominal strength (and of the area under the post-peak branch of the dimensioless load-displacement diagram) was also reached increasing the particle density. In Chapter 4 it was speculated that the asymptotic value was reached once a continuous path of bond elements formed through the depth of the specimen. However, it was also shown that the final cracks were not necessarily developing along this path. The same type of behaviour is now detected in the specimens with thicker ITZ. Also in this case a continuous path of bond elements is not always found, unless the interface is very thick. Rather, clusters of particles whose size increases with the ITZ thickness are found. Figure 5.6 gives an example of a specimen with relatively thick interface (0.75 mm) where the ITZ is not yet percolated.

The peak load is reached as soon as the stress distribution leads to formation of macro-cracks, and the value of the peak load depends on the layout of the micro-cracks. In the specimens with thick interface micro-cracking is very limited and sometimes completely

(a)                                        (b)
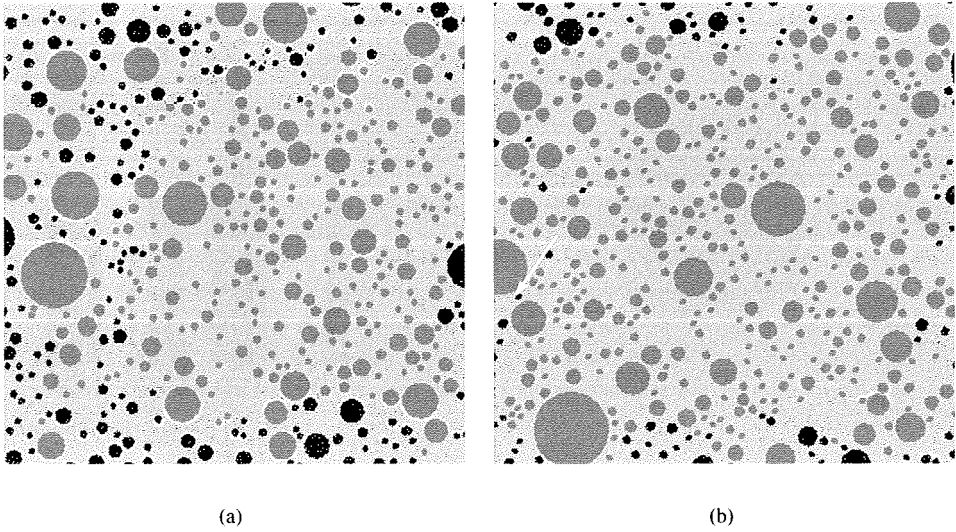
Figure 5.5: 2D lattice analyses with different ITZ thickness. Crack pattern at peak in a specimen with (a) 0.50 mm and (b) 0.75 mm thick ITZ. The arrow points to the location where the macro-crack will form.
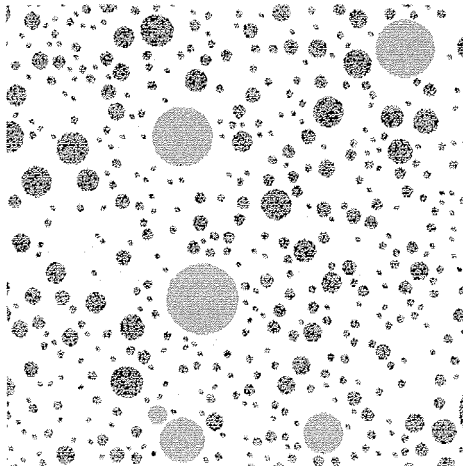


Figure 5.6: Example of a lattice with 0.75 mm thick ITZ.

47 steps after peak

147 steps after peak

247 steps after peak

347 steps after peak
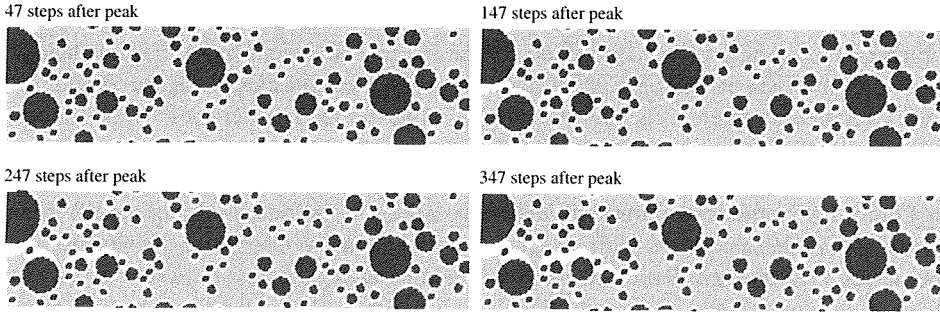
Figure 5.7: 2D lattice analyses with different ITZ thickness. Crack development in in the immediate post-peak regime in the specimen shown in Figure 5.5(b).

absent. Macro-cracks begin to form not necessarily from coalescence of existing micro-cracks. An example of this phenomenon is given in Figure 5.7, which shows the formation of macro-cracks in the specimen with a 0.75 mm thick interface, which was already shown in Figure 5.5(b). In Figure 5.7 the displacements are amplified by a factor 1500 to make cracks visible. Clearly, the region where the crack will form is still intact at peak, see Figure 5.5(b). However, as soon as one element fails in this region, elements start to fail in a row, in a process which cannot be arrested anymore.

It should be questioned if the different crack development in the specimens with *thin* and *thick* interface depends on the length of the bond elements in each layer, which is about ten times longer that the real ITZ. One could speculate that, if much thinner ITZ layers would be adopted, pre-peak micro-cracking might occur. In this case, of course, the combined effect of ITZ thickness and particle density should be taken into account, as the condition of percolation would be achieved with different ITZ thicknesses for different particle densities.

### Post-peak

The numerical results in the post-peak regime are summarized in Figure 5.8(a) and 5.8(b). The first figure represents the dimensionless load-displacement diagrams up to a value of $\delta/\delta_{peak} \approx 6$. The second figure contains two diagrams: in the upper diagram, the area under the post-peak branch of the dimensionless load-displacement diagram is given as function of the ITZ thickness for each of the three meshes, with the thicker line indicating the average value; in the lower diagram the total number of lattice elements failing during the post-peak load drop and in the tail of the softening regime, respectively, has been indicated.

These results are similar to the results obtained with varying particle density. Also in that case it was found that the area under the post-peak branch of the dimensionless load-displacement diagram increases first, and reaches afterwards an asymptot (see Figure 5.8(b), upper diagram). As already shown in Chapter 4, the largest fraction of energy is used also in this case to form continuous cracks from shorter macro-cracks that formed

during the post-peak load drop. Furthermore, the post-peak results present a large scatter, which is consequence of the dependence of the fracture behaviour on the particle layout. Examples of crack patterns are given for each of the three meshes in Figures 5.10, 5.11 and 5.12. In each figure, it is indicated where in the specimen the crack is going to form and the crack patterns at the bottom of the post-peak load drop and at a displacement $\delta = 25\ \mu m$.

In Figure 5.8(b) the total number of elements failing in the post-peak regime has been drawn. As in the specimens with increasing particle density, also in the specimens with increasing ITZ thickness lattice elements fail mainly during the post-peak load drop. The diagram in Figure 5.8(b) also shows that there is a direct relation between the total number of elements failing in the post-peak regime and $W_f^*$. In fact, if the number of elements failing in the post-peak regime increases, also $W_f^*$ does, and vice versa. This might seem trivial at first sight: indeed, if all elements have the same strength, the energy spent for fracturing the specimen would be proportional to the number of failed elements; however, the lattice elements have different strengths, and the energy is in this case depending also on the relative number of elements failing in each of the three phases.

The fractions of different phases failing in the post-peak regime are represented in Figure 5.9. This figure shows that the fraction of matrix elements and internal bond elements failing in the post-peak regime decreases when the ITZ is thicker, while the fraction of external bond elements increases. This means that also in this type of specimens the relative energy spent in the post-peak regime for fracturing the specimen increases because of branching and bridging effects, and that these phenomena occur mainly in the external portions of the ITZ. The cracks, rather than proceeding straight through the matrix, deviate towards neighbouring weak regions. An example is the crack labelled with $a$ in Figure 5.10 , which shows a detail of the crack pattern for a specimen with 0.25 mm and 0.75 mm thickness. In the case of *thin* interface, after de-bonding has occurred, cracks propagate straight through the strong matrix rather than deviating towards neighbouring weak elements. In fact these are too far and, for deviating from its original trajectory, the crack would require much more energy. As counteracting effect, there is the probability that continuous straight paths of interface elements form when the ITZ becomes thicker. An example of straight crack propagating through weak bond elements is given in the crack labelled with $b$ in Figure 5.10. Between the two effects, the first prevails anyhow on the second, which depends also on the alignment of the particles. The effect of crack deviation is shown also in Figures 5.11 and 5.12, where it is evident that the final crack is obtained by coalescence of shorter cracks, which form a very tortuous pattern. Even, as an extreme situation, cracks can arrive to propagate nearly vertically (for example, see the specimen with 0.50 mm thick ITZ in Figure 5.12).

It has already been mentioned that the large scatter in results in the post-peak regime depends on the random mutual position of the particles in the specimen. In the specimens with different particle densities this caused a standard deviation of $W_f^*$ up to 0.12, This value rises to 0.29 in the specimens with different ITZ thickness and indicates that the scatter in results is in this case even bigger. The scatter in results is also reflected in the random formation of the final cracks, whose position in the specimen and pattern vary for the same specimen when the ITZ becomes thicker (see Figures 5.11 and 5.12).

(a)                                    (b)
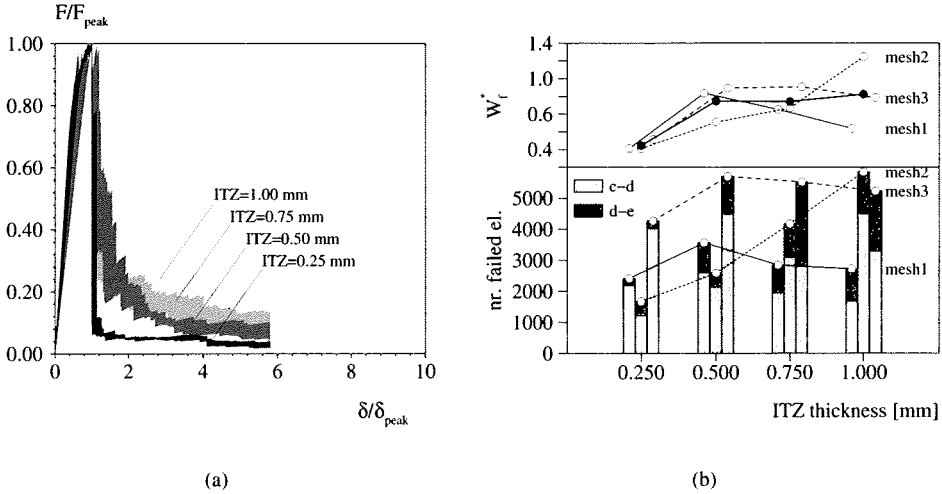
Figure 5.8: 2D lattice analyses with different ITZ thickness. (a) Dimensionless load-displacement diagrams. (b) In the upper diagram: area under the post-peak branch of the dimensionless load-displacement diagrams, $W_f^*$. In the lower diagram: number of beams that fail in the post-peak regime, between different loading stages ($c - d$ is the steep load-drop; $d - e$ is the tail of the softening branch, until $\delta/\delta_{peak} \approx 6$).
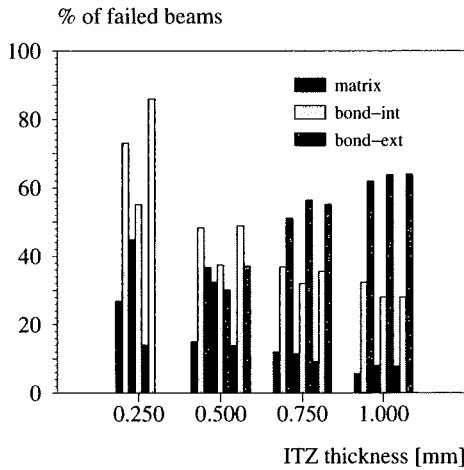


Figure 5.9: 2D lattice analyses with different ITZ thickness. Fraction of the number of beams failing in the post-peak regime.
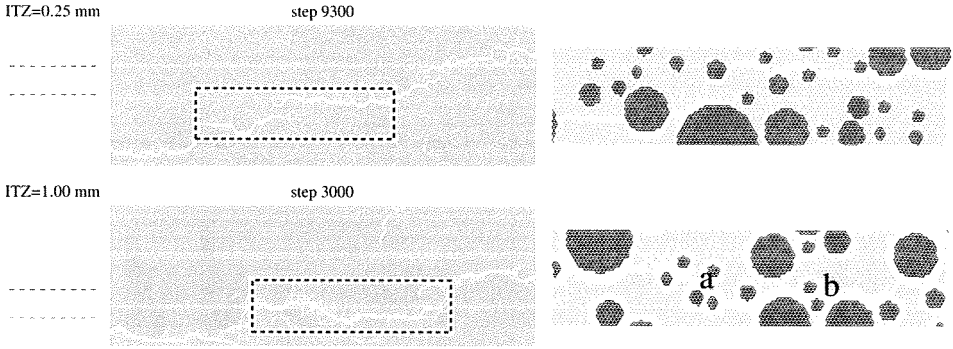
Figure 5.10: 2D lattice analyses with different ITZ thickness. (Left) Macro-crack patterns at the end of the steep post-peak load drop in a specimen with $P_k = 0.35$ (specimen PK35_P2) and different interface thickness. (Right) Details of the macro-crack.
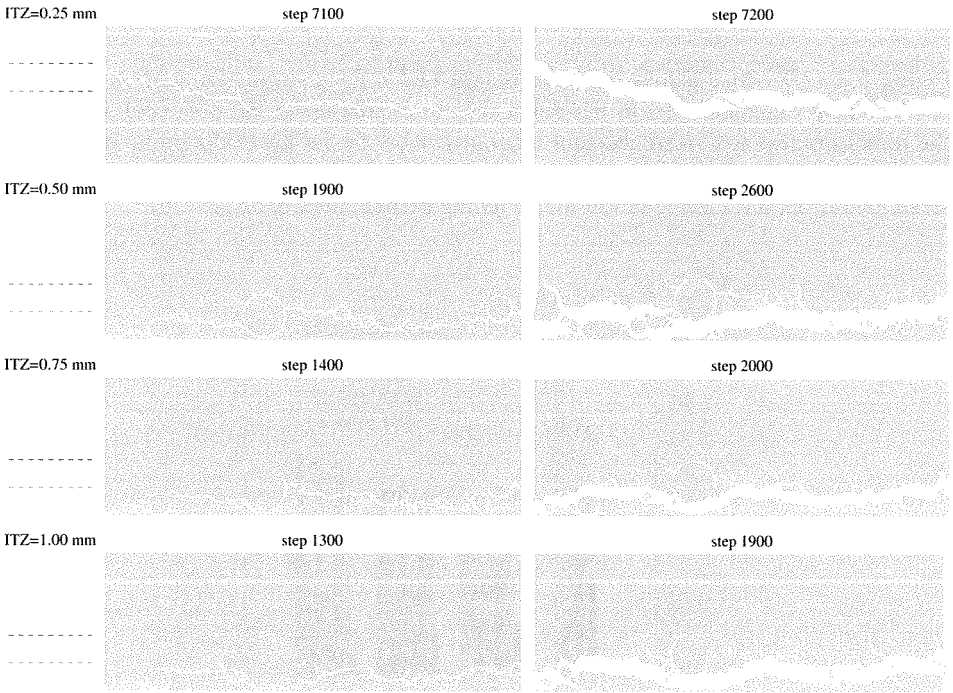


Figure 5.11: 2D lattice analyses with different ITZ thickness. Macro-crack patterns in a specimen with $P_k = 0.35$ (specimen *PK35_P1*) and different interface thickness. The crack patterns are shown (left) at the end of the steep post-peak load drop and (right) at $\delta = 25\ \mu$m.
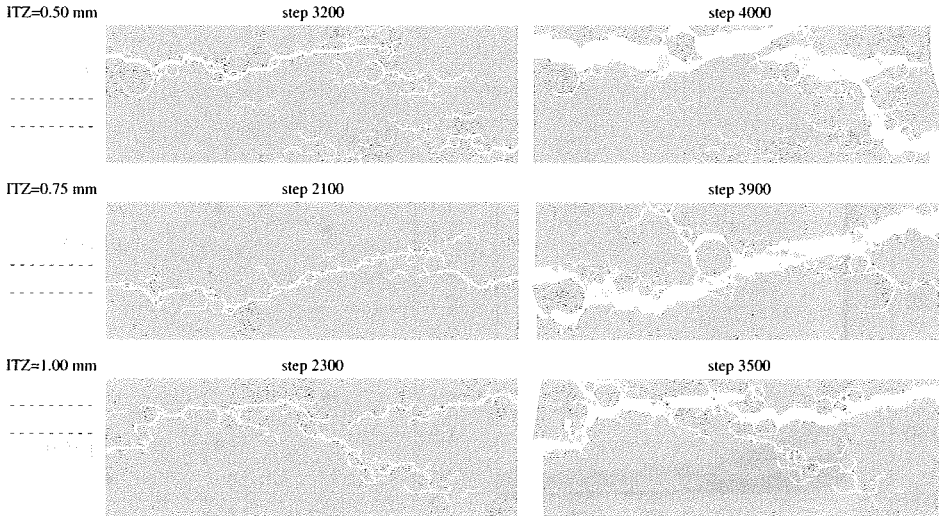
Figure 5.12: 2D lattice analyses with different ITZ thickness. Macro-crack patterns in a specimen with $P_k = 0.35$ (specimen *PK35_P3*) and different interface thickness. The crack patterns are shown (left) at the end of the steep post-peak load drop and at $\delta=25$ $\mu$m.

## 5.2  Effect of the ITZ strength

The results from lattice analyses described so far show that the ITZ determines the fracture mechanisms. Being the weakest link in the whole system, cracks start and propagate in the ITZ during the pre-peak regime. In the post-peak regime, when cracks coalesce through the matrix, the particles operate as crack arrestors, and fracture progresses, once again, through the ITZ. Therefore it has to be expected that a change in the ITZ strength affects the fracture process. It is generally recognized that the strength of the material can be increased by improving the strength of the ITZ, at costs of the ductility. *High strength concrete* is an example, though there are opposing views on the effect of making the interface denser in such material. Some claim that in this case the next weakest spot to fail first will be the calcium-hydroxide, which is directly in contact with the aggregate. In order to evaluate the response of the lattice to a change in ITZ strength, the 3D analyses already conducted for varying particle density were repeated assigning to the interface the same strength as the matrix, namely $f_{t,b}=5$ MPa.

### 5.2.1  Results

The results of the analyses are summarized in Figure 5.13. In the diagrams representing the nominal strength and the area under the post-peak branch of the dimensionless load-displacement diagram versus the particle density (Figure 5.13(b) and (d) also the results obtained from the analysis with $f_{t,b}=1.25$ MPa have been added for comparison.

(a)

(b)



(c)

(d)
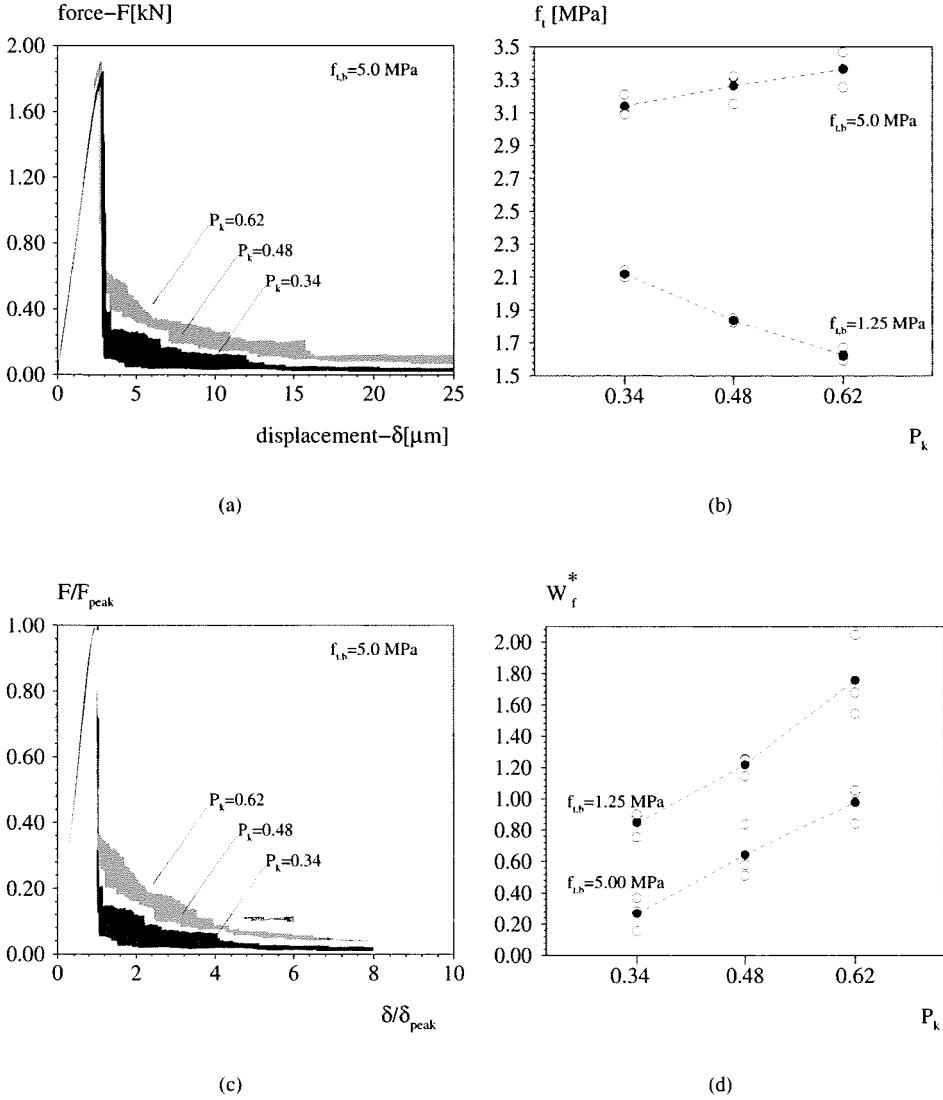
Figure 5.13: 3D lattice analyses with ITZ strength $f_{t,b}$=5.0 MPa. (a) Load-displacement diagrams; (b) nominal strength: comparison with the case $f_{t,b}$=1.25 MPa; (c) dimensionless load-displacement diagrams; (d) area under the post-peak branch of the dimensionless load-displacement diagrams, $W_f^*$: comparison with the case $f_{t,b}$=1.25 MPa.

The most significant difference between the case of *weak* and *strong* interface is in the pre-peak regime:

- The analyses conducted with $f_{t,b}$=1.25 MPa showed a kink in the pre-peak branch of the load-displacement diagram, with the first lattice beam failing at a load level of about 10% of the peak load. In the analyses conducted with $f_{t,b}$=5.00 MPa the diagram is straight up to peak and the first beam fails at a load which is $50 \div 70\%$ of the peak load. The nominal strength, rather than decreasing with the particle density, even exhibits a slight increase (7% increase against the 20% decrease in the analysis with $f_{t,b}$=1.25 MPa). The absolute value of the nominal strength increases of 50% in the specimens with sparse particle distribution up to 100% in the specimens with dense particle distribution.

In the post-peak regime, the results from the analyses with $f_{t,b}$=5.00 MPa are consistent with the results obtained with $f_{t,b}$=1.25 MPa:

- The area under the post-peak branch of the dimensionless load-displacement diagram increases with the particle density. However, in the case of *strong* ITZ, $W_f^*$ is only about 50% of $W_f^*$ in the case of *weak* ITZ.

In summary, by strengthening the ITZ the lattice becomes much stronger but also more brittle. Notice that similar results were obtained in [80]. In that case the analyses were conducted varying the ITZ strength in a 2D coarse lattice mesh, with only one sparse particle distribution. The different way in which fracture progresses in the weak and strong material is elucidated in the following by means of the histograms in Figure 5.14 and by means of the crack patterns in Figures 5.15, 5.16 and 5.17. Figure 5.14 shows the total number of elements failing at each loading stage, see Figure 5.14(a), and the fractions of different phases failing at peak, in the post-peak load drop and in the tail of the softening, see Figure 5.14(b), (c), and (d). These diagrams can be compared directly with the diagrams shown in Figure 4.38 in Chapter 4. The comparison highlights the following similarities/differences:

- The total number of elements failing increases with the particle density. However, when $f_{t,b}$=5.00 MPa the number of steps necessary to reach a vertical elongation of the specimen $\delta = 25$ $\mu$m reduces to half of the value needed in the analysis with $f_{t,b}$=1.25 MPa. In the latter case, the highest percentage of elements was failing in the pre-peak regime, and these were bond elements. In the case of strong interface, on the contrary, only a small percentage of the total number of steps is sufficient to reach the peak load and the largest portion of beams fails in the post-peak regime, during the post-peak load drop. A comparable number of elements fails also in the tail of the softening regime when the particle distribution is denser. The elements failing in the pre-peak regime are in this case also matrix elements: the percentage of matrix elements failing is larger than the bond elements in the specimens with sparse particle distribution and decreases when the density of the particle distribution increases. However, not only matrix and bond elements fail in this phase of loading, but also aggregate elements. Though, these are just a few.

(a)

(b)

(c)

(d)
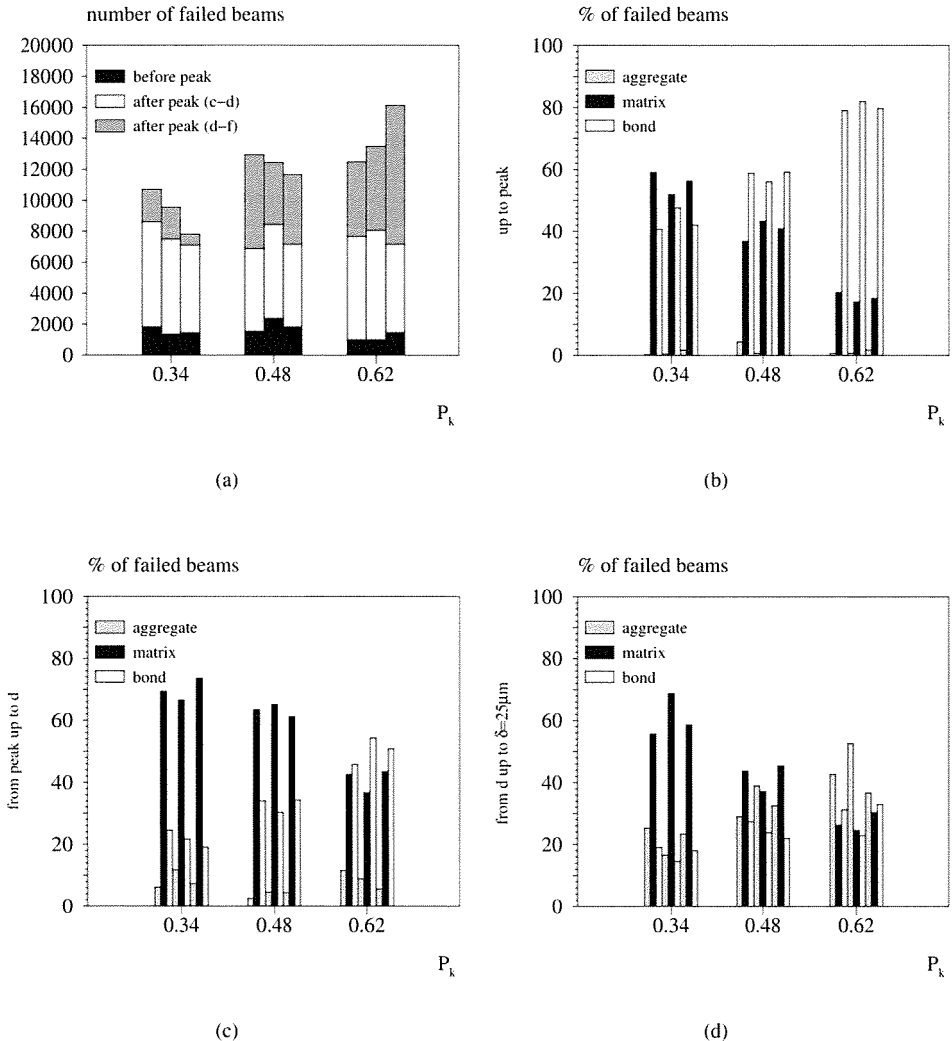
Figure 5.14: 3D lattice analyses with ITZ strength $f_{t,b}$=5.0 MPa. Number of beams that fail between different loading stages: $c$ is the peak load, $c - d$ is the steep post-peak load drop, $d - e$ is the tail of the softening branch, until $\delta$=25 $\mu$m. (a) Total number and (b),(c),(d) percentage of the number of beams failing between different loading stages.

- In the post-peak regime, the percentage of matrix elements failing both in the immediate post-peak as well as in the tail of the softening regime decreases with the particle density, while the percentage of bond elements increases. However, also

the percentage of aggregate elements failing at these stages increases and becomes even comparable with the bond elements.


Figures 5.15, 5.16, 5.17 show the crack patterns in two specimens that are representative for the complete series. In Figure 5.15 the crack pattern is represented using the elements that failed in the pre-peak regime, the matrix in black and the bond in white. In Figure 5.16 and 5.17 the crack patterns are those at the end of the post-peak load drop and at 25 $\mu$m vertical displacement. It was mentioned previously that the nominal strength of specimens with strong ITZ is up to 100% bigger than in specimens with weak interface. The reason, quite straightforward, is the higher strength of the single lattice elements. However, it is quite curious that the nominal overall strength and the strength of the ITZ elements do not increase proportionally. This could have been expected if the crack patterns in the specimens with weak and strong interface were similar. However, the crack patterns are different, because in the specimens with strong interface the initial cracking occurs sparsely and randomly in the ITZ and in the matrix. Rather than continuous short cracks at the edge of the aggregates, isolated elements, failing until the peak is reached, are observed. The effect of the isolated cracking on the load-displacement diagram is that this remains linear up to the peak.

In the analyses conducted with a weak interface the peak was reached when the stress situation did not allow for more de-bonding, and the short cracks around the particles coalesced propagating through the matrix. The different density of the short cracks was indicated as cause for the different nominal strength: the higher the micro-crack density, the lower the nominal strength. In the specimens with strong ITZ, the micro-cracks are replaced by isolated elements that fail, and the peak is reached when, starting from these elements, other elements start to fail in a row, to form macro-cracks. Though the mechanism is similar, the initial crack scenario is different.

The formation and interaction of macro-cracks is the phenomenon governing the post-peak regime, and the structural ductility depends on the tortuosity of the cracks. If the particle distribution is sparse, relatively long cracks can propagate between particles. On the contrary, if the particle distribution is dense, more and shorter cracks form. Failure of the specimen will require in the second case more crack bridging, and, as a consequence, more energy. Already in Chapter 4 and earlier in this chapter it has been underlined that the spatial distribution of the particles is in this stage of loading determinant for the structural response, for example determining a very large scatter of the results. In the specimens with high strength of the ITZ the particle density still affects crack development in the post-peak regime, though the response of the specimens is less ductile than the response of the specimens with weak interface. Figures 5.16 and 5.17 show that in this case there is an additional factor to cause more straight cracks: crack propagation through the aggregates. Though the aggregates are twice as strong, cracks do not deviate towards the weaker matrix but proceed straight. This mechanism is typical of a high strength concrete, where particles and matrix have comparable strengths. Obviously, the absence of weaker elements around the particles prevents cracks from deviating from the straight path, independently on the relative matrix/aggregate strength.
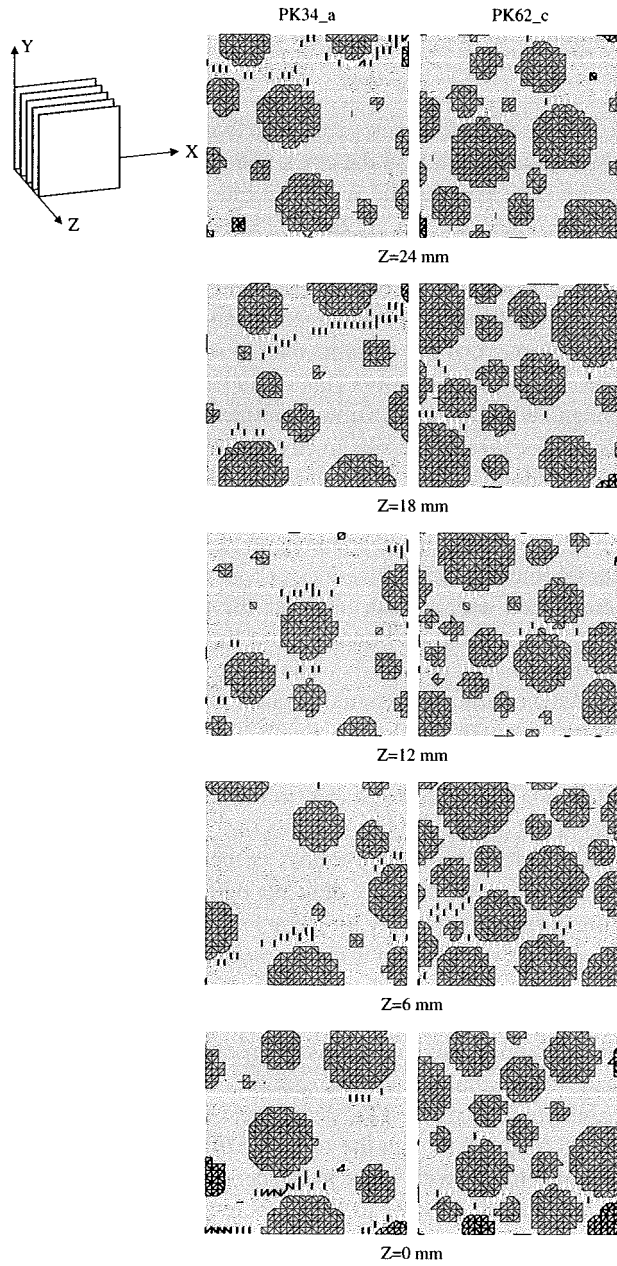
Figure 5.15: 3D lattice analyses with ITZ strength $f_{t,b}$=5.0 MPa. Crack patterns at peak in specimens with $P_k = 0.34$ and $P_k = 0.62$.
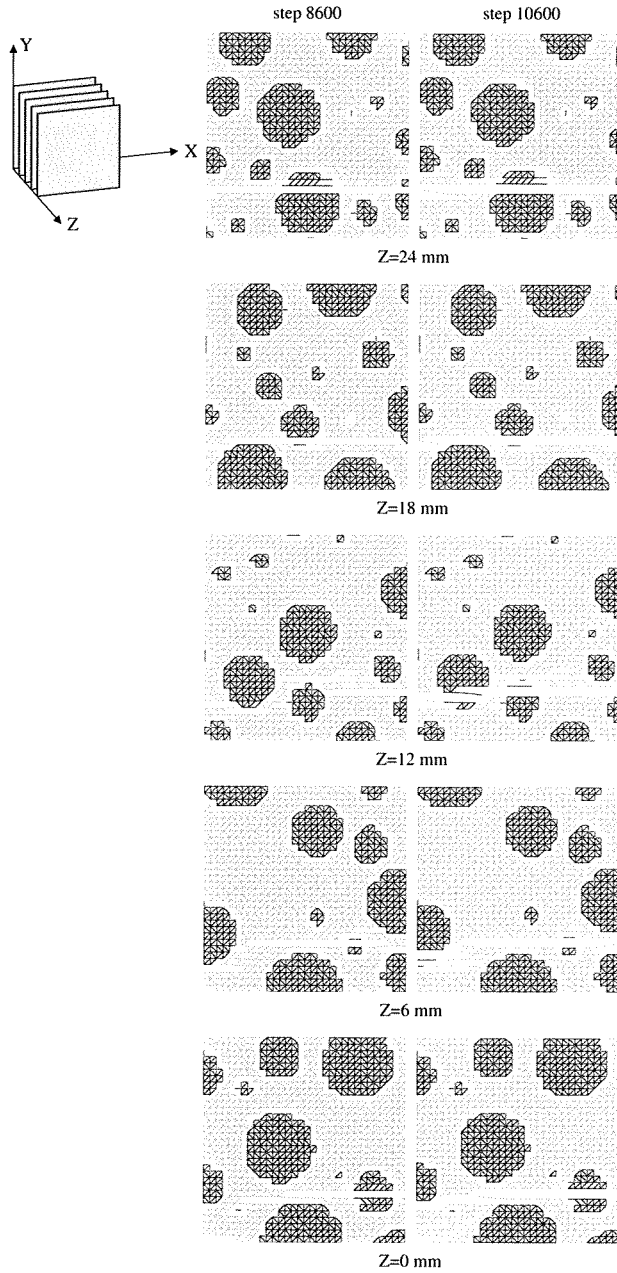
Figure 5.16: 3D lattice analyses of a specimen with $P_k = 0.34$ and $f_{t,b}$=5.0 MPa. Crack patterns in the post-peak regime: (a) at the end of the steep post-peak load drop; (b) at $\delta$=25 $\mu$m.
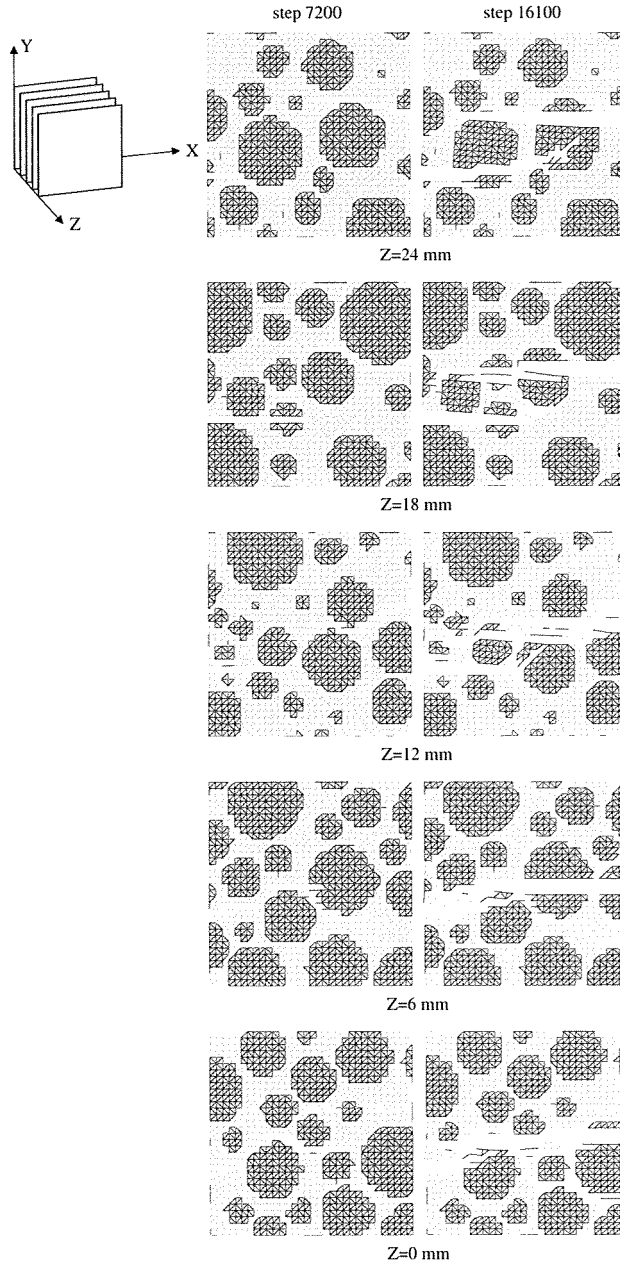
Figure 5.17: 3D lattice analyses of a specimen with $P_k = 0.62$ and $f_{t,b}$=5.0 MPa. Crack patterns in the post-peak regime: (a) at the end of the steep post-peak load drop; (b) at $\delta$=25 $\mu$m.

# 5.3 Effect of the ITZ stiffness

One of the tenets concerning the ITZ is that it is very porous. Due to the high porosity, a lower stiffness of the ITZ should be expected in comparison with the matrix phase. Nevertheless, in all analyses reported in this thesis the same Young's modulus has been assigned to matrix and bond elements, consistently with earlier simulations. The effect of the ITZ stiffness in compact splitting tests on single grain concrete specimens was studied in [103], where it was concluded that the ITZ stiffness hardly affects the results, while the choice made for the ITZ strength has a strong effect. Though this conclusion might not be generally applicable to all lattice simulations, especially when more and denser particles are considered, it seems the only possible within the already rough schematization of the ITZ in the lattice model. In addition to this, no sound measurements are available of the stiffness of the ITZ to suggest a different choice for this parameter. Nevertheless, it is interesting to check if the assumption of equal stiffness in the matrix and in the ITZ holds also for the 2D analyses conducted with varying particle density. For this purpose, the single bond element has been considered as a system of 3 beams connected in series, see Figure 5.18(a). The length of each beam of the system is determined by the fraction of the total length of the system that falls inside the aggregate, the matrix, or the ITZ ($l_a$, $l_m$ and $l_b$, respectively). It is assumed that the overall strength of the system coincides with the strength of the weakest element in the series, and the overall stiffness is determined following:

$$\frac{l}{E_{b,eq}} = \frac{l_a}{E_a} + \frac{l_b}{E_b} + \frac{l_m}{E_m} \tag{5.1}$$

The equivalent Young's modulus adopted in the analyses was computed assuming that $E_b = 1/3 \, E_m$ and that $l_b = 50 \, \mu$m. For each particle distribution ($P_k = 0.35, 0.51, 0.67$) the specimen was randomly positioned at 2000 different locations in the computer generated particle distribution (see Chapter 4). Then, the number of bond elements and their equivalent Young's modulus was determined for each of these positions. In this manner it was found that $17800 \leq E_{b,eq} \leq 33000$. Figure 5.18(b) shows the distribution of $E_{b,eq}$ in a specimen with $P_k = 0.67$. The results obtained for the two extreme values of $P_k = 0.35$ and $P_k = 0.67$ are illustrated in Figures 5.19, 5.20, 5.21, 5.22, 5.23. Figure 5.19 contains the load-displacement diagrams and, in the insets, the dimensionless load-displacement diagrams. In Figure 5.20 the average nominal strength and the area under the post-peak branch of the dimensionless load-displacement diagram versus particle density have been represented for each specimen, together with the corresponding average value (dashed lines connect the averaged values). Qualitatively, the results of these analyses are consistent with the outcome from the analyses conducted with $E_b = E_m$. Though different values are found both for the nominal strength and the $W_f^*$, these fall within the scatter of results that is due to the material randomness. In the specimens with a sparse particle distribution, the dimensionless load-displacement diagrams are practically overlapping, while a larger scatter is observed in the post-peak regime results, in case of dense particles, which is also consistent with the previous results. Though the cracks form and propagate in a similar manner, however the location of the cracks in the specimen can

(a)                                                    (b)
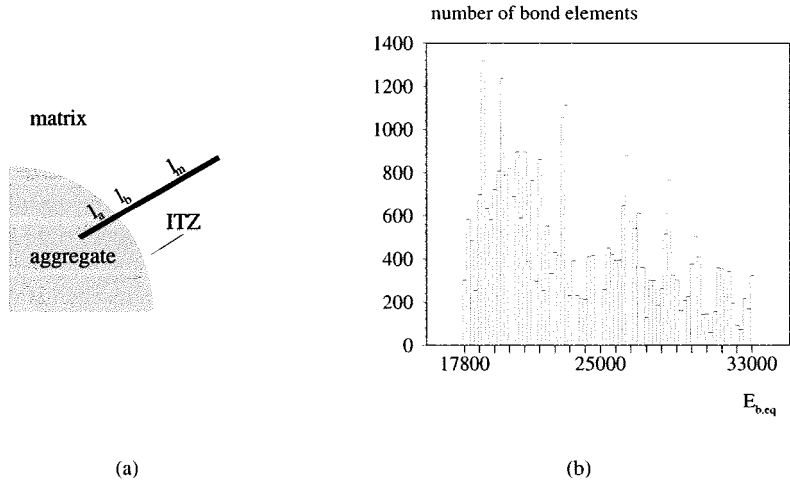
Figure 5.18: Model used for studying the effect of the ITZ stiffness (2D lattice). (a) The ITZ beam is schematized with a series model; (b) distribution of Young's moduli $E_{b,eq}$ in a specimen with $P_k = 0.67$.



(a)                                                    (b)
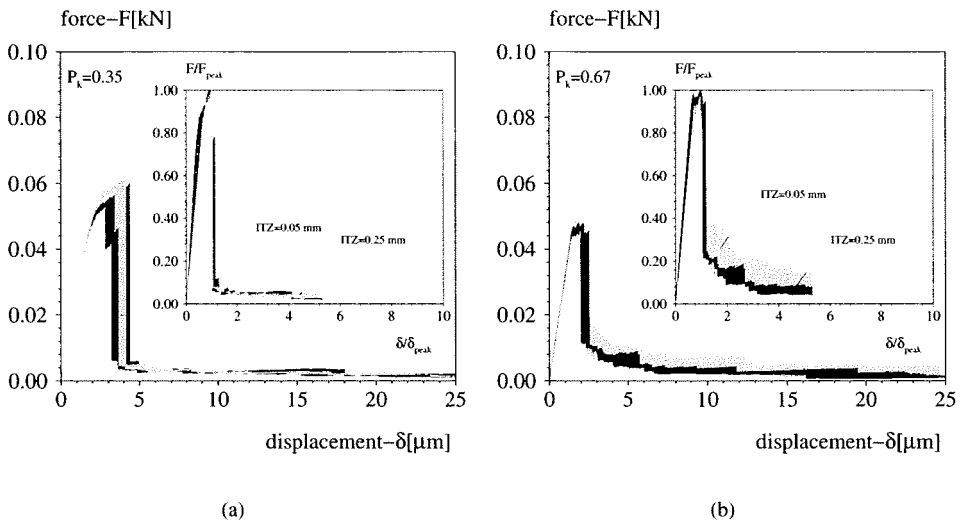
Figure 5.19: 2D lattice analyses with different stiffness of the ITZ. (a) Load-displacement diagrams for specimens with (a) $P_k = 0.35$ and (b) $P_k = 0.67$. The dimensionless diagrams are in the insets.

differ as a consequence of a different stress map induced by the different stiffnesses of the elements.



(a)  (b)
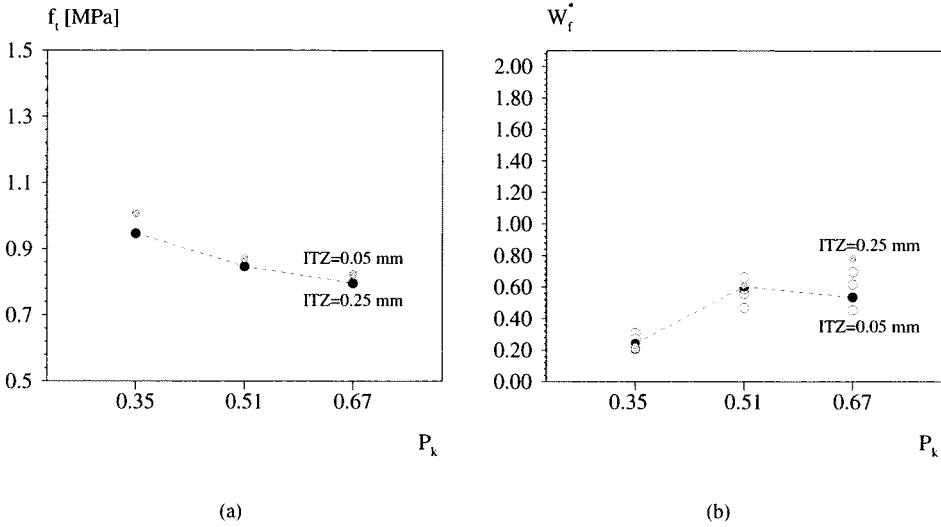
Figure 5.20: 2D lattice analyses with different stiffness of the ITZ. (a) Nominal strength. (b) Area under the post-peak branch of the dimensionless load-displacement diagrams, $W_f^*$.



(a)  (b)
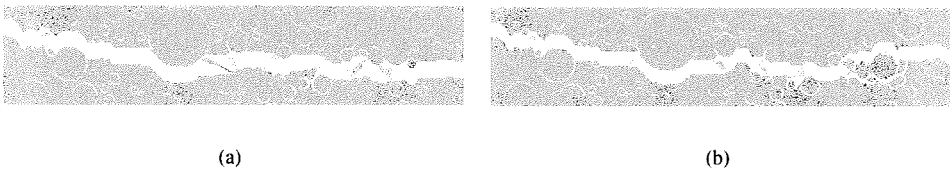
Figure 5.21: 2D lattice analyses with different stiffness of the ITZ. Macro-crack at $\delta = 25\ \mu$m in a specimen with $P_k = 0.35$ and interface thickness (a) 250 $\mu$m and (b) 50 $\mu$m.

In Figure 5.21 the crack pattern at $\delta = 25\ \mu m$ has been drawn for a specimen with $P_k = 0.35$. In this case, the cracks develop at a similar location both in the specimen with $E_b = E_m$ and in the specimen with equivalent Young's modulus of the bond elements, and the difference is only in the crack details. However, in Figure 5.23, which shows the crack pattern in a specimen with $P_k = 0.67$, it can be seen that the final crack is forming in different parts of the specimen. Figure 5.22 shows an example of crack patterns at peak in specimens with sparse and dense particle distribution.

(a)                                                 (b)
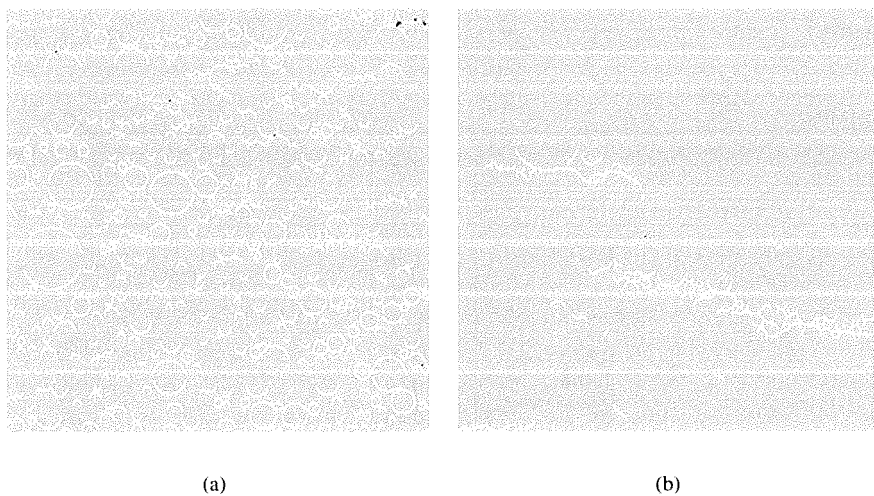
Figure 5.22: 2D lattice analyses with different stiffness of the ITZ. Crack patterns at the peak load in a specimen with (a) $P_k = 0.35$ and (b) $P_k = 0.67$, and a 50 $\mu$m thick ITZ.



(a)                                                 (b)
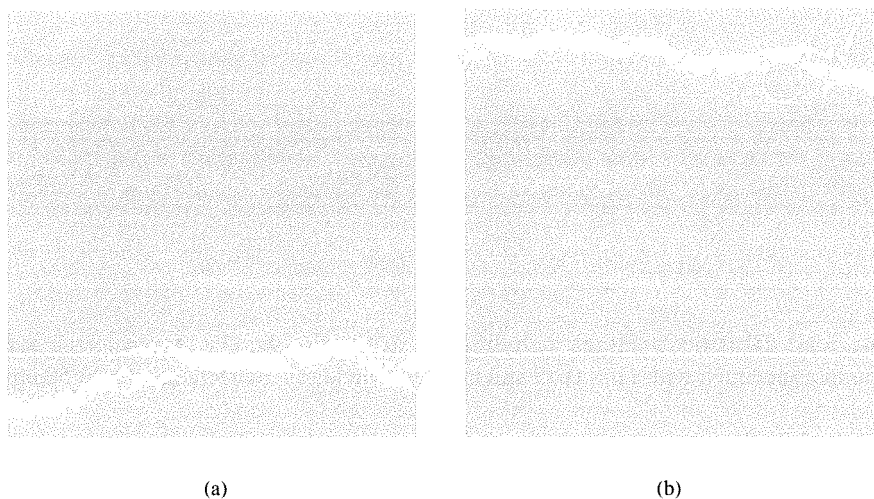
Figure 5.23: 2D lattice analyses with different stiffness of the ITZ. Macro-crack patterns at $\delta = 25$ $\mu m$ in a specimen with $P_k = 0.67$ and (a) 250 $\mu$m, (b)50 $\mu$m thick ITZ. The specimen with 50 $\mu$m thick ITZ is the same as in Figure 5.22(b).

Also in this case it can be observed that in the specimen with sparse particle distribution short cracks are distributed over the whole surface of the specimen, while they are locally concentrated in case of a specimen with dense particle distribution. As a conclusion, the assumption of bond elements having the same stiffness as the matrix elements can be accepted, as a different stiffness can affect only the details but not the overall fracture mechanism.

## 5.4    Concluding remarks

In the lattice model the ITZ is roughly schematized with one layer of elements, whose length is 5-10 times the thickness usually mentioned in literature (50 $\mu$m). Following this schematization, uniform mechanical properties are assigned to the interface element along its length, while it is commonly recognized that the physical and mechanical properties of the ITZ vary gradually from the inner to the outer side. Another approximation made in the lattice model is that the ITZ has the same stiffness as the matrix, while a lower stiffness should be expected as consequence of the high porosity of the ITZ.

It is very difficult to measure experimentally the mechanical properties of the ITZ and even the definition of ITZ remains ambiguous in literature. In the lattice model this phase is already quite roughly represented, and there is no sound reason to insist in matching parameters that, as a matter of fact, are still unknown. However, it is clear from earlier analyses as well as from the analyses reported in Chapter 4 of this thesis, that the ITZ determines the fracture behaviour, especially in the pre-peak regime. To have more insight in the influence of the ITZ properties on the lattice response, the effect of varying ITZ thickness, strength and Young's modulus have been investigated in this chapter.

The ITZ thickness was enlarged in the 2D specimens by adding sequentially layers of ITZ, after having fictitiously increased the diameter of the particles. The effect of increasing ITZ thickness is similar to increasing particle density: the nominal strength decreases, while the area under the post-peak branch of the dimensionless load-displacement diagram increases. Both these quantities reach an asymptotic value as soon as clusters of particles form sufficiently long and continuous paths of bond elements. However, while in the specimens with varying particle density extensive de-bonding occurs also in the case of dense particles, in the case of thick ITZ macro-cracks form already at early loading stages.

For studying the effect of the ITZ strength, the 3D analyses already reported in Chapter 4 were repeated assigning to the ITZ the same strength as the matrix. The results show in this case that the material becomes stronger but less ductile. Though the nominal strength is in this case independent of the particle density, the ductility still increases for denser particle distributions. Furthermore, the pre-peak regime remains linear. The micro-crack layout, which governs the pre- and peak regime, is characterized by isolated cracks that form randomly near the aggregates or within the matrix, independently of the particle distribution. The spatial random distribution of the particles still allows for crack bridging, though the cracks are generally more straight and even cross the particles, as a result of the high strength of the ITZ elements.

Finally, the effect of the Young's modulus of the ITZ was studied assuming for the bond elements a system in series and defining an equivalent Young's modulus which depends on the portions of the bond element that fall inside the aggregate, ITZ and matrix phase. The results from these analyses show that a variation in the stiffness of the ITZ elements does not affect the overall response of the specimens in terms of nominal strength and development of the fracture process. The variation of slope in the post-peak branch of the dimensionless load-displacement diagrams seems in this case consequence of the large scatter in the post-peak results.

The ITZ is determining the onset and propagation of cracks. The relative volume and strength of the ITZ determine a different layout of the micro-cracks in the pre-peak regime and, as consequence, a different strength of the specimen. In the post-peak regime, the properties of the ITZ influence to some extent crack bridging, but an important role is played also by the particles, which work as crack arrestors. Therefore, the distribution in space of the particles can affect the crack tortuosity and cause a large scatter in the results.

# Chapter 6

# Lattice analysis of the torsion test

The concept of elementary modes of failure, on which linear fracture mechanics is based, is commonly adopted also in non-linear fracture mechanics of concrete. According to the theory of linear fracture mechanics, crack surfaces are planar in each of the three elementary modes of failure, while curved crack surfaces point to mixed-modes of fracture [44]. However, crack curvature must be considered in relation to the scale of observation. The linear elastic fracture mechanics theory is of course valid only when the material is completely homogeneous. The straightness or tortuosity of the cracks surfaces depends on the relative size of particles and specimen, and on the particle distribution, as has been extensively discussed in the previous chapters. Different attempts have been made to measure in the laboratory fracture parameters related to the three elementary modes of fracture in concrete, and the debate about the validity of these experiments is sometimes quite intense. For example, 2D lattice analyses of four-point shear beams [82] have contributed, together with laboratory experiments [99], to invalidate previous laboratory experiments where mode II fracture energy was measured [13]. These lattice analyses showed that the entire response of the shear beam can be modelled using a mode I criterion at the mesolevel. If mode II of failure has been quite extensively investigated, not many examples of research on mode III of failure can be found. Attempts to investigate mode III fracture have been made in the past performing torsion tests on cylindrical specimens [112, 113]. It was found that the application of an axial restraint and the presence of a notch in the specimen are important for changing the fracture mode. However, not much attention was given to the crack patterns, with the exception of the cone-like failure mode detected in notched cylinders subjected to torsion under restrained axial displacements [6]. If mode II fracture can still be handled using the 2D version of the lattice model, mode III requires that the third direction is taken into account. In this chapter, the lattice model is applied to investigate torsion tests. The torsion tests are important not only for validating the 3D version of the lattice model, but also because they can help to better understand the limits of the model, since a variety of tensile/compressive failure modes can be obtained by varying the axial constraint. For this reason, an extensive series of experiments was conducted on notched and un-notched cylinders under imposed axial force or displacement

[58]. The limitation imposed by the available computational model, however, imposed to restrict the numerical experiments to the case of cylinders subjected to torsion and free axial displacements (where the axial force is constantly zero). These numerical/laboratory experiments will be the object of this chapter.

# 6.1   Lattice Analysis

The specimen used for the numerical analysis was an un-notched cylinder with the same dimensions as the specimens used in the laboratory: diameter 34 mm and height 68 mm. For the construction of the mesh a cell-size $s=1$ mm was adopted, with randomness $A/s = 0.001$. The corresponding lattice mesh is composed of 449179 elements with average length $l_{avr}=1.24$ mm. In order to reproduce in the numerical analysis the same boundary conditions as in the laboratory experiments, the nodes of the bottom end of the specimen were clamped, while an in-plane displacement corresponding to a unit rotation upon the axis was applied to the nodes of the upper end. These nodes could move freely in the axial direction. The same diameter of the cross section and the same mechanical properties of the different phases as in previous 3D lattice analyses were assigned to the beams ($h$=0.57735 mm, $E_a = 70$ MPa, $E_m = E_b$=25 MPa, $f_{t,a}/f_{t,m} = 2$ and $f_{t,b}/f_{t,m} = 0.25$). The diameter of the particle distribution varied between 2 mm and 8 mm. The initial particle density, $P_k = 0.40$, results in $P_{k,latt} = 0.22$ after overlaying of the particle distribution and the lattice mesh. In the fracture criterion, only contribution of the axial force was considered; both the contribution of the bending and of the torsional moment were neglected. The only aim of this analysis was to evaluate whether the model could predict the experiments qualitatively. For this reason no parametric study was conducted to match the maximum torque, which in fact results smaller than in the experiments by a factor $\approx 8$. The smoothened torque-rotation diagram obtained from the lattice analysis is represented in Figure 6.1. This diagram is characterized by a nearly-linear pre-peak behaviour and is very smooth in the post-peak regime. The crack patterns at different load levels in the post-peak regime are drawn in Figure 6.2 and Figure 6.3. In Figure 6.2 the cracks are represented as a cloud of points, which indicate the pattern of the macro-cracks. These points are the mid-points of the matrix elements that have failed prior to the loading level under consideration. In Figure 6.3 the cracks are represented in analogy with the impregnation technique, which was used to detect the cracks in some of the laboratory experiments. The specimen is cut into slices along the axis and the bond and matrix elements that have failed are represented in white and black, respectively. In the pre-peak regime de-bonding prevails, while macroscopic cracks form in the post-peak. According to the predictions from theory, cracks start from the outer surface of the specimen, where the principal tensile stresses have the maximum value. The crack, which spirals around the specimen, propagates through the depth of the cross section. Figure 6.3 suggests that the macro-cracks that started developing at one side of the specimen can be found after some more loading at the opposite side. Indeed, it was found in the experiment that the spiralling crack loops around the specimen. However, the 3D graphical representation which is adopted here is
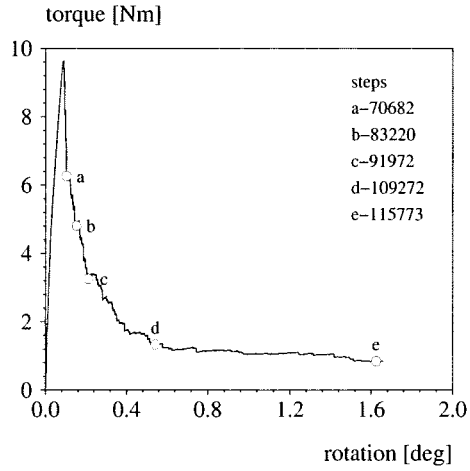
Figure 6.1: Lattice analysis of a torsion test: torque-rotation diagram.



step 70682    step 91972    step 103959    step 115773
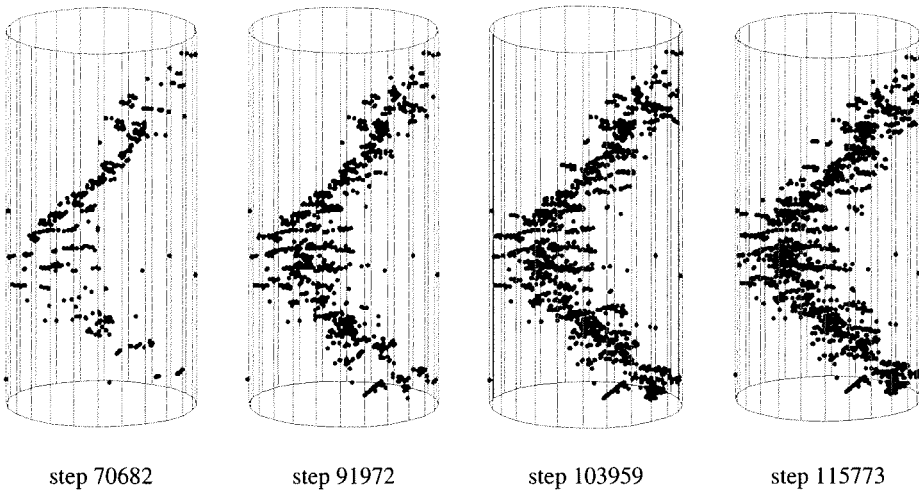
Figure 6.2: Lattice analysis of a torsion test: 3D crack patterns at different load levels (see Figure 6.1).

Step 83220

Step 115773

| 4 mm | 12 mm | 20 mm | 28 mm | 36 mm | 44 mm | 52 mm | 60 mm |

Z
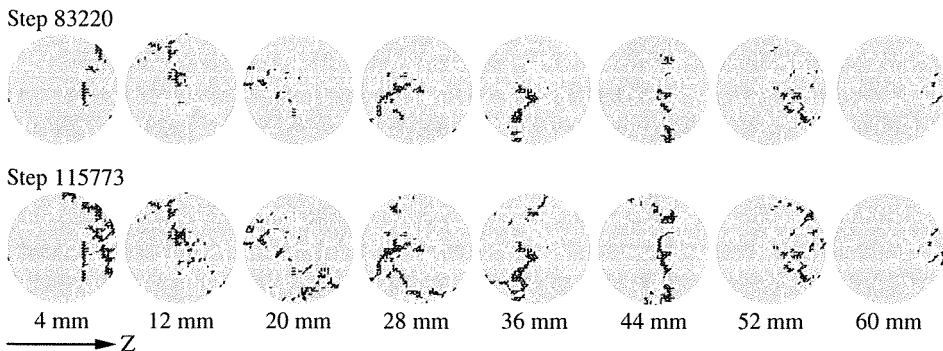
Figure 6.3: Lattice analysis of a torsion test. Crack patterns at different heights in the specimen.

not sufficient to understand how the different cracks open during loading, and to verify that looping indeed occurs. Such type of representation would have requested storage of the displacements at each node, at regular loading steps, while the computer memory allocation granted for this analysis was not sufficient for this. Though details of the crack obtained from the numerical experiment are still missing, it is important to stress that the main fracture mechanism, the spiralling crack, is fully captured.

## 6.2   Experiments

The laboratory experiments were conducted both on un-notched and notched cylinders. The specimens were cored from concrete blocks made of two different concrete mixtures, with maximum diameter $d_{a,max}$=8 mm and 2 mm, respectively [58]. The testing machine could apply a rotational and an axial load, which could be coupled or decoupled. The rotation of the cylinder was used as feedback signal, and axial displacement, axial load, rotation and torque were measured during the experiments. Three load-paths were explored: torque applied under zero axial load, torque applied under constant compressive load, and torque applied under zero axial displacement. It should be mentioned that if the axial deformation is zero, axial compression will build-up during torsion. The only difference with the case of constant compressive load is that the axial load does not remain constant but reaches a maximum in correspondence of the onset of the softening regime [58]. In all load-paths the constant axial load/deformation was applied prior to the torque. Here only the experimental results obtained for the first of the three load-paths are shown in Figure 6.4, for each of the two concrete mixtures. The diagrams in Figure 6.4 include the results from two series of experiments, each conducted using three specimens. The torque-rotation curves are very smooth and show a relatively small scatter. Furthermore, the main trends in behaviour for the two mixtures is similar. The insets in Figure 6.4 show the surface crack patterns recorded with the naked eye at the end of the tests. In

a number of specimens, crack detection was made impregnating the specimens with fluorescent epoxy while still clamped between the loading platens, and cutting it in slices after hardening of the epoxy. Each slice was photographed under UV light and the images obtained from a digital camera were then converted to greyscale and inverted. In this manner, the impregnated cracks appear black. An example of crack detection with this technique is given in Figure 6.6 for a specimen impregnated just after the peak load (specimen A), and a specimen impregnated in the tail of the diagram (specimen B). The corresponding torque-rotation diagram is represented in Figure 6.5. In all the experiments on un-notched cylinders the first crack to be detected was a spiralling crack. This crack is labelled with 1 in Figure 6.4(a). As this crack was detected with the naked eye, it could
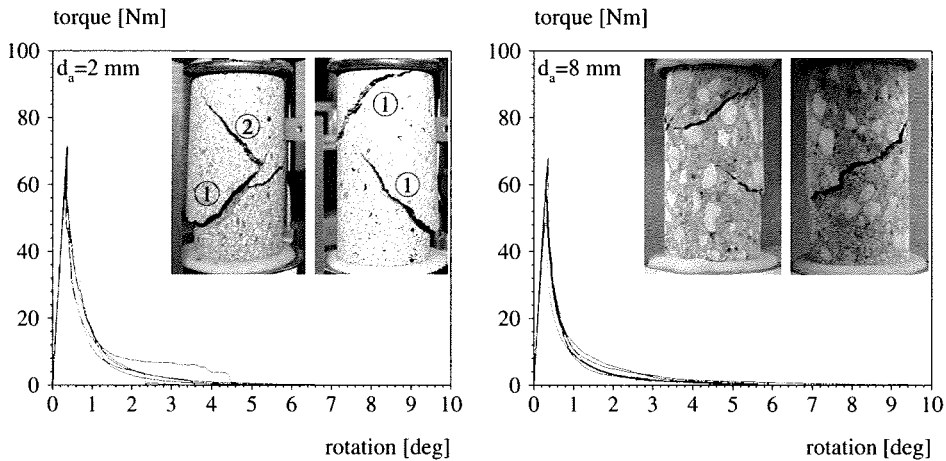


Figure 6.4: Experimental results from torsion tests. Torque-rotation diagrams and crack patterns.

be visualized only at a later stage, when it had already developed along the whole length of the specimen. For this reason, the visual detection alone of the crack could not indicate from which location the crack was actually starting to develop. Even the impregnation tests do not give a better insight in this sense (see Figure 6.6), because the ends of the specimen were cut away when the specimen was removed from the loading platens. The lattice analysis suggests that the spiralling crack starts in the body of the specimen and covers almost the whole height of the specimen already soon after the peak torque (see the crack pattern at step 70682 in Figure 6.2). From theory, on the other hand, one could expect that the weaker spot in the specimen is next to the loading platens, where the radial tensile stresses induced by the Poisson's effect contribute to a bi-axial tensile stress. After the spiralling crack has propagated, different failure processes could be observed. In the unconfined tests, the spiral crack could loop around the specimen, and secondary cracks departing from the spiralling crack form. The secondary crack is labelled with 2 in Figure 6.4(a). The fracture mechanism proposed in Figure 6.7, which shows the same

specimen of Figure 6.4(a) after complete failure, suggests that bending governs formation of the secondary crack. The spiral crack separates the specimen into two halves, and the tip of each part touches the bottom of the opposite part. Each of the two parts of the specimen behaves as a cantilever beam and the bending moment acting at the clamped end produces the secondary crack [100]. The lattice analysis cannot capture this mechanism because the model is not able to mimic contact between the two halves of the specimen. Anyhow, the analysis was stopped too prematurely for showing any secondary crack mechanism, which occurs only in the tail of the post-peak regime, when deformations become large.    In the other experiments, always an axial compressive force was
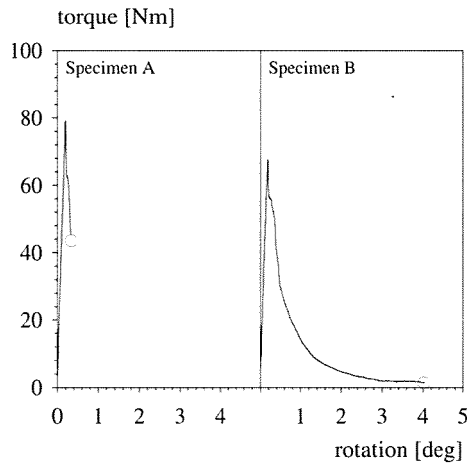


Figure 6.5: Experimental results from torsion tests. Torque-rotation diagrams in the impregnation experiments.

present. Among all these experiments, those conducted on notched cylinder under axial confinement are especially interesting. In these experiments cracks formed only in one of the two halves, while the other half was intact. The mechanism visible with the naked eye was still a spiralling crack. However, examination of the specimen after complete failure as well as impregnation technique showed a conical failure surface inside the specimen (see Figure 6.8). This type of failure very much resembles the failure in compression of a specimen loaded between rigid steel platens. In analogy with the cone-like failure under stiff aggregates in compression [95], it can be speculated that the cones form from an array of splitting micro-cracks and that shear occurs only at a later stage of loading. This questions the existence of shear as elementary mechanism of fracture (see also [68]).

Not many attempts were made in the past to study failure in compression with the beam lattice model. In [60] the correct crack patterns in a compression tests with unrestrained lateral deformations were found using the usual fracture criterion but with a coefficient $\alpha = 0.50$. In [102] the failure law derived in [16] was used as local fracture criterion in the lattice model for studying the bi-axial failure contours. In this case the model was a

Specimen A



| 10 mm | 15 mm | 22 mm | 29 mm | 35 mm | 43 mm | 50 mm | 57 mm |

Specimen B



| 3 mm | 11 mm | 20 mm | 32 mm | 37 mm | 45 mm | 52 mm | 59 mm |

Z
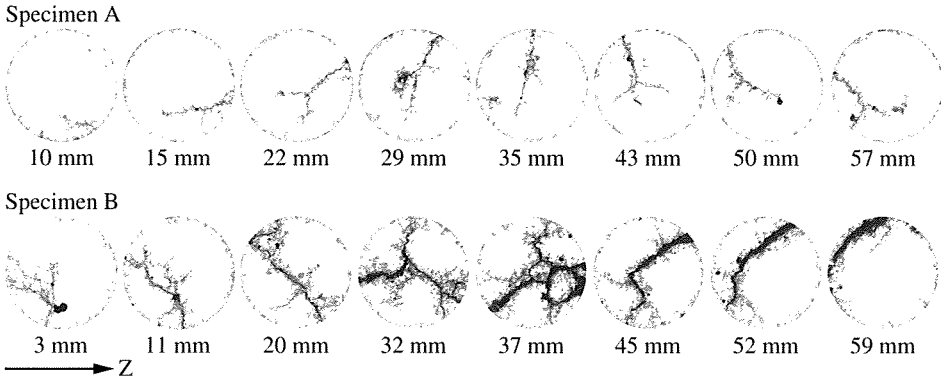
Figure 6.6: Experimental results from torsion tests. Crack patterns detected with the impregnation technique at different heights of the specimen.

very rough 3D schematization and the crack patterns were completely neglected.

A cone-like failure as in the torsion tests occurs also in the Brazilian test. This case was analyzed with the 2D lattice model (see Appendix A); the lattice model captures micro-cracking along the inclined planes, but the prevailing failure mode in this test remains bending. On the other hand, if compression/shear failure is taken into consideration already in the fracture criterion, only the conical failure mechanism develops, but the final failure mechanism cannot be captured because the model does not include friction/sliding mechanisms. Such type of fracture mechanisms can be captured when the beam model is coupled with a particle model type [52].

# 6.3 Concluding remarks

Torsion tests on concrete cylinders are suitable for validation of the 3D version of the beam lattice model for two reasons: the first, because crack surfaces oriented in multiple directions can be obtained; the second, because multiaxial tension/shear stresses can be obtained. A series of laboratory experiments was conducted on un-notched and notched cylinders with two different maximum sizes of the aggregates. The tests were conducted applying an axial force or displacement first, followed by a rotation upon the axis of the cylinder. Independently of the maximum aggregate sizes and the presence of a notch, it was found that the main fracture mechanism is the formation of a crack spiralling around the specimen, while in the tail of the torque-rotation diagram different secondary fracture mechanisms form, depending on the axial constraint.

The 3D lattice model, with the classical fracture criterion based on local mode I failure of the lattice beam, is able to capture the principal fracture mechanism not only in terms of torque-rotation diagram but also in terms of crack pattern. These results suggest that mode I is the local fracture mechanism in concrete. However, secondary fracture mechanisms develop in the torsion tests. These mechanisms involve friction between the crack sur-

Figure 6.7: Experimental results from torsion tests. Formation of secondary cracks due to bending.



(a)                                                    (b)
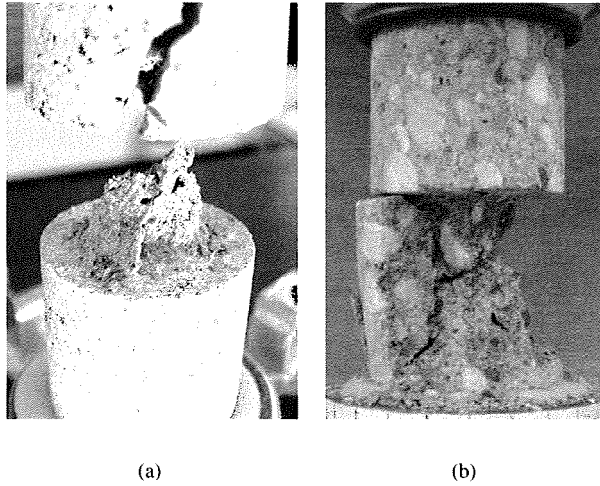
Figure 6.8: Experimental results from torsion tests. Cone-shaped crack surfaces in notched cylinders loaded in torsion under axial compressive load: (a) $d_{a,max}$=2 mm and (b) $d_{a,max}$=8 mm.

faces and cannot be captured with the lattice model. Nevertheless, the secondary fracture mechanisms are relevant only for predicting the final configuration of the crack pattern, when the structure has exhausted all its reserves of strength.

# Chapter 7

# Conclusions

Since the Fictitious Crack Model was proposed by Hillerborg in 1976 [42] models of fracture in concrete have persisted in considering concrete as homogeneous and in taking a macroscopic view on cracking. This approach involves the definition of strain softening as property of the material. Therefore, additional material properties such as fracture energy, shape of the softening curve and ultimate strain must be defined. However, all these parameters are *size dependent* and vary with the applied stress field (tension/compression/shear). Obviously, these parameters are not properties of the material, but depend also on the characteristics of the structure. Also the process of crack formation is neglected in these models. For sake of simplicity, it is assumed that the material remains linear elastic until the peak, and that all cracking phenomena (micro- as well as macro-cracking) develop in the post-peak regime. On the other hand, it is known from experiments that micro-cracks form already in the pre-peak regime, macro-cracks grow in the post-peak regime and branching/bridging of macro-cracks characterizes the tail of the softening [96]. Furthermore, cracking is often considered smeared over a certain region rather than modelled as a discontinuous phenomenon. The latter approach, if applied, requires knowledge "a priori" of the crack pattern.

A straightforward manner of taking the material heterogeneity and the process of crack formation into account is to consider a discrete model which mimics, up to an acceptable level of detail, the disordered material structure. Examples of such a type of approach can be found in rock mechanics [23] and in the field of theoretical physics [41]. In the first, rock is discretized with interacting rigid bodies; in the second, disordered materials are discretized with a lattice network. The discrete approach has several advantages with respect to the continuum approach: 1) the possibility of modelling progressive damage as broken bonds that form and coalesce in macroscopic fractures; 2) the possibility of modelling structural softening without introducing a constitutive law based on softening; 3) the possibility of reproducing anisotropic behaviour induced by damage accumulation and, as a consequence, any crack pattern.

In the field of concrete fracture mechanics there is still some hesitation to abandon the classical homogeneous/continuum approach for the heterogeneous/discrete approach. Nev-

119

ertheless, there are signs that things are moving in this direction. For example, one should think of the increasing interest towards a heterogeneous/homogeneous approach such as in the *multi-scale* approach. The major obstacle to using heterogeneous/discrete models is the computer power and computer time that are necessary to handle these models. Considering the speed with which computer technology evolves, it should be expected that not much time will elapse before this type of analysis will become a daily routine.

Computer power mainly affects the level of detail with which the material is schematized. For this reason, most of heterogeneous/discrete models that have been introduced up to date still use softening locally. In this case the advantage of using a discrete model instead of a continuum model is questionable. As a matter of fact, if softening is introduced locally, then the model looses its capability to explain the causes of softening. In the *Delft beam lattice model* developed by van Mier and Schlangen [81] the choice has been made to adopt a direct representation of the material at the meso-level, as detailed as possible, and a linear elastic purely brittle behaviour at local level. The immediate advantage of this approach is that the number of necessary material parameters is reduced to the elastic properties and tensile strength of the three phases: aggregate, matrix and interfacial transition zone. In this manner not only the number of size-dependent variables is limited to the tensile strength only, but such size-dependence is further reduced when homogeneous phases are considered. The main problem is to find the material characteristics of the interface [104]. This thesis comes after a series which started with the work of Schlangen [79] and continued with the works of Vervuurt [104] and van Vliet [101]. In all these works a 2D version of the Delft lattice model was applied to predict/reproduce laboratory experiments, showing a qualitatively good prediction of the crack pattern but too brittle load-displacement diagrams. This has motivated to further investigate reasons and remedies to such a brittleness, which is done in this thesis.

The first reason for the brittle lattice response is related to 3D effects, which are neglected in the 2D model. 3D effects are important in concrete. If the material would be perfectly homogeneous, and the stress distribution would be uniform through the thickness of the specimen, cracks would develop instantaneously across the specimen, and the 2D version of the model would suffice. However, randomly distributed particles that function as crack arrestors cause a tortuous crack in all directions, even when a planar crack is expected, as result of geometry of the specimen, loading and boundary conditions. 3D lattice analyses are practical only using parallel computing facilities. For this reason the 3D version of the model was implemented in a code for parallel computing [59]. The parallel version of the lattice put the author in a unique position with respect to her predecessors, because it gave for the first time the opportunity of investigating in more detail the influence of the material structure on the lattice response. This is done in Chapter 4 and Chapter 5.

In Chapter 4 attention focuses on the effect of the particle density. In order to compare the 2D and the 3D response, lattice analyses with increasing particle density have been conducted both with a 2D lattice and a 3D lattice. Though the size of the specimens is still relatively small in comparison to the size of laboratory specimens (60 mm in the 2D, and 24 mm in the 3D case), these analyses can still give some insight in the influence of the particle density on the overall response of the structure. Three different stages can be distinguished in the fracture process: in the pre-peak regime, small cracks form at

the interface between matrix and aggregate; in the steep post-peak load-drop the micro-cracks coalesce and form macro-cracks; finally, macro-cracks propagate and branching and bridging occurs in the tail of the softening regime. The results show that when the particle density increases, the strength of the lattice decreases and its relative ductility increases. Micro-cracking occurring in the pre-peak regime governs the behaviour at peak. In the 2D analyses micro-cracks are distributed over all the specimen in case of sparse particle distributions, and localized in narrow regions in case of dense particle distributions. It should be remarked here that in the case of high particle densities the definition of a Representative Volume Element would fail already in the pre-peak regime. In the 3D analyses the number of micro-cracks rather than their spatial distribution governs both the pre-peak and peak regime. In the 3D case, denser particle densities correspond to more micro-cracks during the pre-peak regime. This is also reflected in the load-displacement diagram, which exhibits a clear non-linear branch immediately before the peak. The interfacial transition zone plays the major role in the fracture mechanism, as it contributes to create continuous paths of weak elements in the case of high particle density. In this case cracks localize already at an early stage during loading. This phenomenon is somehow smoothened in the 3D lattice, where formation of micro-cracks through the depth of the specimen delays the coalescence of micro-cracks into macro-cracks. The response in the post-peak regime is governed by the tortuousity of the macro-cracks. In the case of high particle density the aggregates, working as crack arrestors, cause shorter macro-cracks, bridged by the particles. Complete failure occurs when all bridges are broken. On the contrary, in the case of sparse particle distributions cracks can follow a straighter path. A direct comparison of 2D and 3D results show that 3D lattices are more ductile in comparison to 2D lattices.

A closer look at the effect of the interfacial transition zone is given in Chapter 5, where the effects both of the interface thickness and strength are studied. For sake of computational time, the effect of varying interface thickness has been studied in a 2D lattice only. The lattice results show that thickening the interface has similar effects as densifying the particles, namely decrease the strength and increase the relative ductility. Both the strength and the energy consumed in the post-peak regime reach in this case asymptotic values as soon as the interfacial transition zone becomes thicker. The reason is that the interfacial transition zone is still too roughly schematized in the model, where the thickness of the interface is at least 5 times larger than in reality. This, of course, contributes to a premature formation of *percolation* paths. To investigate the effect of the strength of the interfacial transition zone, the extreme situation of an interface as strong as the matrix has been considered in the case of a 3D lattice. In this case the strength of the material is independent of the particle density, and the lattice is stronger but more brittle. In terms of crack patterns, these are generally straighter, and cross the particles in some cases. This situation resembles in practice the behaviour of high strength concrete. The unique feature of the lattice model, which is capable of modelling different types of materials, should be mentioned here. As a matter of fact, other discrete models such particle models, cannot model fracture through the particles, as these are considered as indefinitely elastic rigid bodies.

Chapter 4 and 5 of this thesis show that 3D effects and a more realistic representation of

the material, with denser particle distributions, all contribute to a more ductile response.
The validation of the 3D model has been done in Chapter 6. For validating the 3D version
of the beam lattice model a series of laboratory experiments was conducted on notched
and un-notched cylindrical specimens under different axial constraints. Due to the very
limited availability of computer tools for running this type of analysis (the analysis was
not run in-house), it was decided to restrict the interest only to the case of a un-notched
cylinder subjected to torsion, allowing free deformations in axial direction. The com-
parison between experimental results and lattice analysis shows that the model is able to
capture both the crack (a spiral which develops along the height of the specimen) and the
characteristics of the torque-rotation diagram. It has to be remarked that this result was
achieved with only one numerical simulation, without any parameter-fitting, and using
the usual fracture criterion which assumes locally only mode I failure.

The adopted fracture criterion has revealed adequate to simulate a wide range of experi-
ments, also when macroscopic shear failure can be expected. An additional example of
possible shear failure is included in Appendix A, which illustrates the comparison of ex-
periments and lattice analyses in the Brazilian test (this time the analyses are conducted
using the 2D lattice). Also in this case the lattice model is able to predict the crack
pattern. All numerical experiments conducted so far address to only one local mode of
failure: mode I. The final collapse of the specimen in the Brazilian test could not be sim-
ulated anyhow because of known limitations in the model, such as the impossibility of
modelling contact/friction mechanisms.

Another limitation of the model lies in the choice of beam elements rather than truss
elements. At the very beginning of this model, beam elements were chosen not only
because they enabled a wider range of Poisson's ratios by varying the ratio between flex-
ural and axial stiffness of the elements, which varies non-linearly with the length of the
lattice elements; another reason was that they were considered most suitable to model
crack bridging. However, if beams are used instead of trusses, the fracture mechanism is
affected by the choice of the lattice geometry, as a consequence of the non-linear depen-
dency of the ratio axial/bending stiffness on the lattice length. As bridging is governed
by the particles, dense particle densities as have been considered in this thesis are proba-
bly sufficient to retrieve bridging also in case a network of trusses is used. Besides this,
trusses also eliminate the uncertainty of the fraction of bending moment (and/or torque in
the case of a 3D lattice) to be taken into account in the fracture criterion.

**Future directions**

The lattice model has unique features but, as all models, also its limitations. One limi-
tation has already been addressed in the previous paragraph, and is related to the choice
of the beam element. The author thinks that such a choice is not necessary when a more
realistic schematization of the material is used in the model. This simplification is very
beneficial as reduces the number of parameters in the model.

The beam lattice model should be improved by coupling it with a particle model to repro-
duce also macroscopic compressive/shear failure mechanisms (as in the model proposed
by Kun et al. [52], for example), and related phenomena such as crack closure (for exam-

ple under cyclic load) or crack dilatancy.

An aspect which has not yet been investigated in the lattice is its dynamic response. In this case, in order to guarantee mass conservation, the beams should be considered massless and point masses should be introduced at the nodes. Despite the assumption of quasi-static conditions, dynamic effects are always present in the laboratory experiments. This poses a question about the feedback signal control to be used for ensuring a stable test [100]. The lattice model could contribute in this sense to optimize the design of laboratory experiments.

An interesting question is if and how the lattice can be applied in the engineering practice. As a matter of fact, the ultimate goal of the researcher dealing with concrete fracture mechanics is to provide engineers with a tool for designing (or assessing) big structures, based on the knowledge gathered from small specimens tested in the laboratory. Obviously, homogeneous continuum models still represent the only option for this type of applications. Nevertheless, the lattice model can help to define the parameters that are necessary to the homogeneous continuum models. Another interesting application of lattice models is in the field of material design and optimization, as well as in the application to coupled flow-stress problems.

.

# Appendix A

# Lattice analysis of the Brazilian test

A feature of the lattice model is that, with a very simple local fracture criterion based on mode I failure, it is possible to describe macroscopic failure mechanisms different than mode I. Examples are the four-point shear beam experiment [79], the bi-axial compression/tension-shear experiment [66], the anchor bolt pull-out [104] and the torsion test (see Chapter 6). In this appendix, the 2D version of the model is used to analyze the Brazilian test. In the Brazilian test, the two mechanisms of fracture to be observed are a splitting crack and a wedge beneath the loading platens (see Figure A.1). As the experiment is
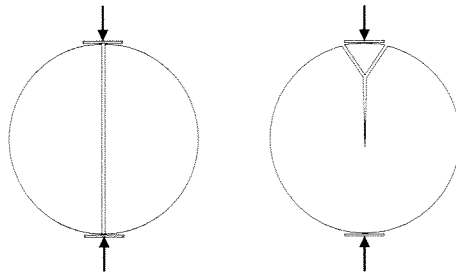


Figure A.1: Fracture mechanisms in the Brazilian test.

usually conducted in load-control, it is not clear which of the two mechanisms occurs first. This is important because the Brazilian test is often used as indirect tensile test, under the assumption that follows from theory of elasticity, that is the splitting crack the mechanism that brings the specimen to failure. The aim of the lattice analysis was to find out in which sequence the two mechanisms occur. Analyses recently conducted with a

model which couples a beam lattice with a particle type model show that in an asphalt cylinder the wedges form as first, and cause the splitting crack [21].

Results from experimental studies that can be found in literature are different and sometimes contradictory. In [38] it was found that aggregate interlock causes higher ratios of cylinder splitting strength over uni-axial tensile strength in specimens with larger aggregate sizes. This implies failure of the specimen after plastic slip of the wedge. Also the observed violation of the *size effect law* for large diameters can be the consequence of a change in failure mode for large sizes [11]. Other researchers, however, found a decrease of strength with increasing specimen size [73].

# A.1    Lattice Analysis

The 2D lattice analysis was conducted on a disc with diameter 75 mm. The specimen was schematized with a random lattice, with size of the Voronoi cell $s = 1$ mm, and average beam length $l_{avr}$=1.14 mm. The particle content was rather dilute ($P_k = 0.34$), and the diameter of the particles varied in the range 2 mm-8 mm. Due to the relatively long lattice elements in comparison with the diameter of the smallest particles, the density of the aggregate phase after overlaying the particle distribution on top of the lattice reached only $P_{k,latt} = 0.21$. As the aim of this numerical experiment was only to predict the fracture mechanism, no special effort was put to match the geometry of the test set-up, nor a parametric study was conducted. The geometry of the beam cross section and the mechanical properties of the different phases were as in all other lattice analyses that are included in this thesis ($E_a$=70 MPa, $E_m = E_b$=25 MPa, $f_{t,a}/f_{t,m} = 2$ and $f_{t,b}/f_{t,m} = 1.0$). The only difference is that the same strength was assigned to the matrix and to the bond phase. This was done only for sake of computational time. In fact, at the time of this lattice analysis the parallel version of the model was not available yet and each analysis, conducted on a single processor Origin 2000 Silicon Graphics machine, required about one week. In case of a weak interface, extensive de-bonding would occur before the first macro-cracks, and a larger number of loading steps would be necessary for reaching the peak load. The loading scheme was schematized in the lattice analysis considering the load applied (in displacement control) through steel loading platens glued to the specimen. Only the upper platen was moving, while the bottom platen remained fix. The loading platens were modelled with four-noded plane stress elements. The condition of no relative displacement between the specimen and the loading platens (which corresponds to the condition of specimen glued to the loading platens) was realized imposing that the displacement of each lattice node falling between the nodes of a plane stress element was expressed as linear interpolation of the displacements of these two nodes. In the numerical experiment the crack opening was measured at about half height of the specimen, as relative displacement of two nodes that were originally at about 30 mm distance. The layout of the numerical experiment is depicted in Figure A.2. The first analyses were conducted with the classical fracture criterion which computes the maximum stress using the Navier's formula, and weights the contribution of the bending moment with the coefficient $\alpha = 0.005$.

load [kN]

steps
a   300
b   450
c   530
d   700
e   820
f   890

crack opening [μm]

(a)                                    (b)
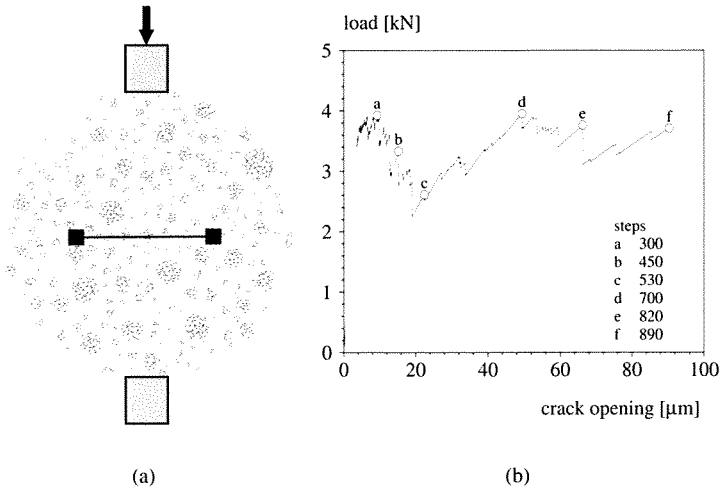
Figure A.2: Lattice analysis of a Brazilian test. (a) Layout of the numerical experiment and (b) load-crack opening diagram (b).

The numerical results are represented in Figure A.2 and Figure A.3. In Figure A.2(b), is the smoothened diagram of the vertical load versus the crack opening. The dots indicate the load levels that correspond to the crack patterns depicted in Figure A.3.

The load-deformation diagram shows two peak loads. In the valley beyond the first peak load (point $c$ in the diagram) a vertical macro-crack has already developed. This crack does not cross the specimen along its complete height, but stops close to the loading platens. At this stage only micro-cracks are present in the zone where wedges are expected to form. At the second peak load (point $d$ in the diagram) radial cracks start propagating from the edge of the specimen inwards. After a decrease of the load, another radial crack appears and the load increases again (point $f$ in the diagram). Also the splitting crack has propagated further to the top of the specimen. The wedge below the upper loading platen is already visible at step $b$. This could be expected since the confinement is active from the beginning. At step $f$ more micro-cracks have formed near the loading platens both at the top and bottom of the specimen.

If the simulation is carried out further, the radial cracks start bending and new radial cracks form. As a result, it is not possible to capture the failure of the specimen, which can occur as consequence of each of the two mechanisms: (1) the radial cracks propagate and join the splitting crack; (2) the wedges form beneath the loading platens and penetrate into the specimen through the splitting crack, producing separation of the specimen in two halves. Limitations in the lattice model prevent from capturing any of these two possible mechanisms of failure. The first mechanism is not captured because the adopted fracture criterion does not include any contribution from compressive stresses. When the splitting crack has propagated, the two halves of the specimen are subjected to bending, and, as a result, the central part of the specimen is under compression.

step 300

step 450

step 530

step 700

step 820

step 890

Figure A.3: Lattice analysis of a Brazilian test. Crack patterns at different load levels. The displacements are scaled by factor 100.
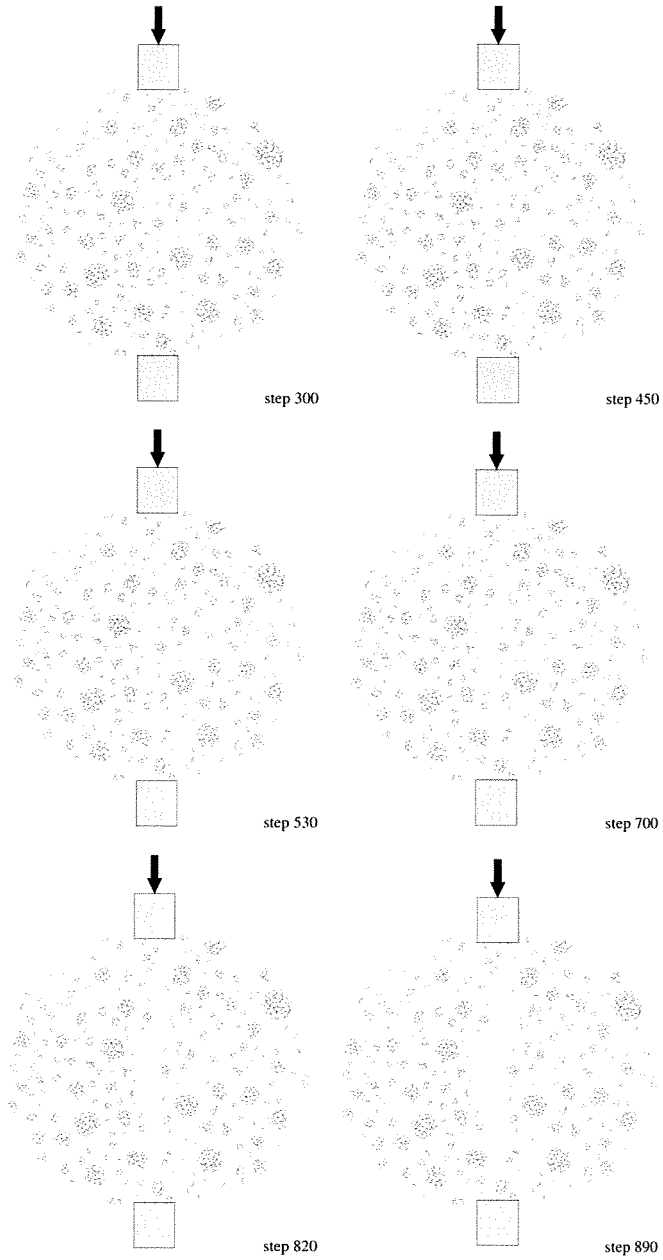
The second mechanism is not captured because no stress transfer is possible between the crack faces after the wedge has formed.

In order to include in the fracture criterion also the contribution of compression and shear, it was then decided to adopt the Mohr-Coulomb fracture criterion. In this analysis the friction angle was set at $\phi = 30^0$, and the corresponding value of the cohesion was derived from $c = f_t/2 \cdot (1/sin(\phi) - tg(\phi))$. For calculating the stresses, it was assumed that the shear stresses are uniformly distributed over the cross section of the beam, so that the maximum critical stress still occurs at the edge of the section. When the Mohr-Coulomb criterion was selected, the first beams to fail were beneath the loading platens and formed a wedge. At this point the numerical simulations was stopped because the wedge could move freely as a rigid body, causing singularity of the stiffness matrix. In order to overcome this numerical problem, as soon as the wedge formed stiff springs were introduced along its edge. These springs could transmit normal and shear stresses and simulate in this manner contact and friction between the edge and the still intact specimen. In this case, however, another wedge, of larger dimensions, was forming.

In order to validate or disprove the results from the lattice analysis, it was decided to conduct some laboratory experiments [56]. Though the results were published later, similar experiments were also being carried out at the University of Madrid [72], showing the existence of a *primary* and *secondary* fracture mechanism in the Brazilian test, which correspond to two different peak loads in the load-displacement diagram.

# A.2   Experiments

Two series of laboratory experiments were conducted: in the first series, the cracks were detected simply with the naked eye; in the second series a long-distance microscope was used for detecting the cracks. The specimens were concrete discs with diameter $D = 75$ mm and $D = 150$ mm and 10 mm thickness. Two different mixtures with river gravel aggregates were used, with maximum grain size $d_{a,max}$=8 mm and 2 mm, respectively. Two different boundary conditions were used in the experiments. In the first case, a plywood layer was placed between the steel loading platens and the specimen. In the second case, the specimen was glued directly to the steel loading platens. A detailed description of the experimental set-up and of the experimental results can be found in [56]. Some of the experimental results from the first series are shown in Figure A.4. The diagrams in Figure A.4 give the load as function of the crack opening, which was measured at about mid-height of the specimen, and the insets represent the post-failure crack patterns.

This first series of experiments turned to be quite sensitive to the adopted boundary condition. In the specimens with the plywood layer, different fracture patterns were detected, including: a single longitudinal splitting crack across the diameter of the specimen; two or more short cracks developing parallel to each other, with overlapping crack tips; secondary radial cracks that could eventually propagate until the splitting crack.
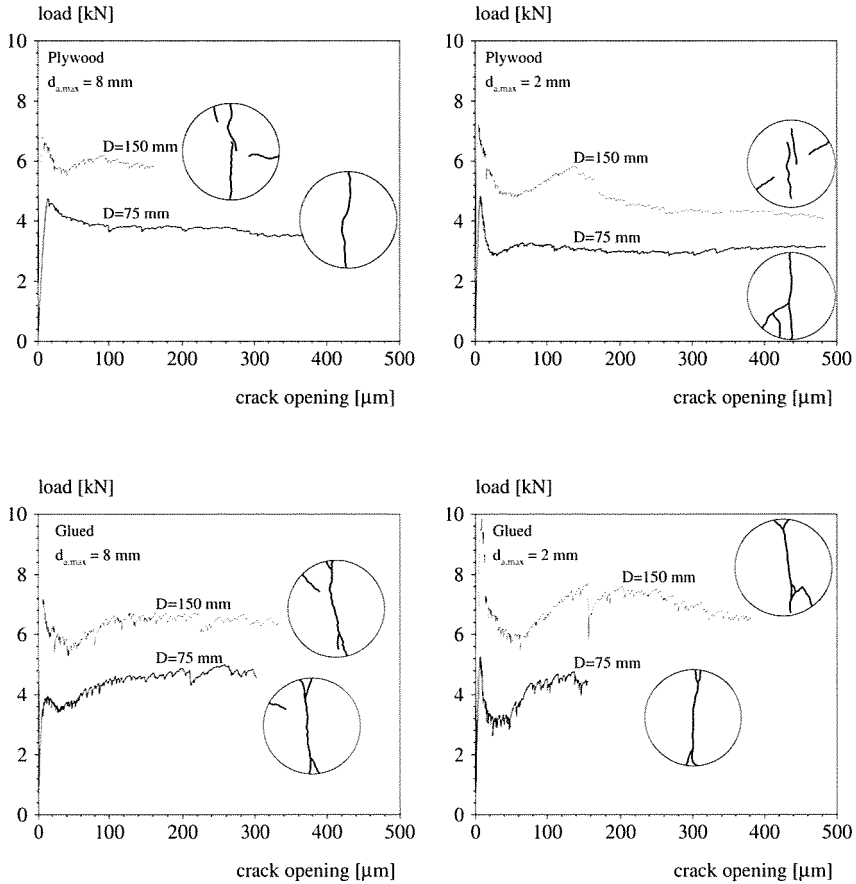
Figure A.4: Experimental results from Brazilian tests. Load-deformation diagrams and fracture patterns for different boundary conditions, specimen size and grain size.

In the specimens glued to the loading platens wedges could be observed. In this case, lateral displacement beneath the loading platens is prevented and, as a result of the high confinement in these zones, the splitting crack deviates from the nearly straight pattern. Also in this case secondary radial cracks were detected. Note that failure of the glued specimens was always abrupt.

The primary and secondary fracture mechanisms correspond to two different peak loads in the load-deformation diagrams.

Some of the results from the second series of experiments are shown in Figures A.5. The dots in the load-deformation diagrams indicate the load levels when each crack was first detected.
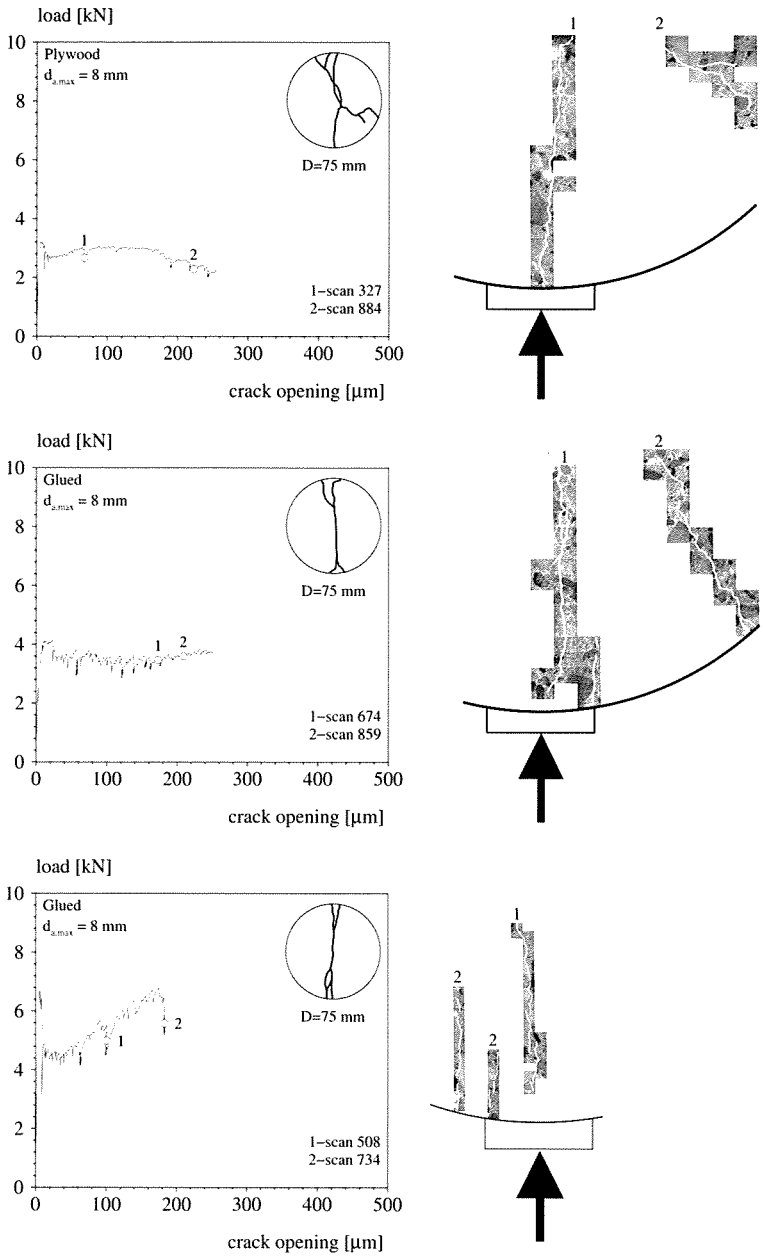
Figure A.5: Experimental results from Brazilian tests. Load-deformation diagram and crack patterns detected with the long-distance microscope.

In the 75 mm *plywood* specimen, failure of the specimen was induced by rapid propagation of the radial crack. Also in the 75 mm *glued* specimen a radial crack was detected. However, this crack closed again and failure occurred through the vertical splitting crack. In the 150 mm *glued* specimen, first the vertical splitting crack developed, and smaller vertical cracks were detected afterwards. No radial cracks were found in this case, perhaps because only a very small area of the specimen could be scanned with the microscope and the radial crack(s) might have formed outside the scanned area. Also in this case, the post-failure crack pattern included wedges beneath the loading platens. Crack growth was too fast to register final rupture and it can only be speculated that the wedges have formed from coalescence of the short splitting cracks detected at the edges of the loading platens. All microscopy experiments showed that the two crack faces move away from each other during the final stage of the test, and that no frictional slip occurs. These experiments suggest that the fracture mechanism that causes wedge formation is likely not of the *shear-type*, but originate from mode I cracks.

## A.3   Concluding remarks

The 2D lattice simulations of the Brazilian test show that the model, which uses a fracture law based on mode I local fracture, is able to predict the crack patterns detected in the laboratory experiments. Two different crack mechanisms develop in the Brazilian test: in the first mechanism, a vertical splitting crack forms in the middle of the specimen and propagates towards the two loading platens; in the second mechanism two types of cracks can develop: small vertical cracks departing from the edges of the loading platens, or radial cracks starting at the edge of the specimen and propagating towards the centre of the specimen. In the load-displacement diagram two peak loads correspond to the two crack mechanisms. The first peak, which corresponds to the formation of the vertical splitting crack, can indeed be considered as an approximation of the uni-axial tensile strength, as this crack forms in a region of (nearly) uni-axial tensile stresses. The second peak corresponds to the radial cracks, which can be detected only when the test is conducted in displacement control. If the test was conducted in load-control, failure would be imminent at the first peak. The final mechanism of collapse of the specimen could not be captured in the laboratory experiments because failure occurred always quite abruptly. The lattice analysis could not give more insight either, because of limitations in the model:

- The radial cracks stop when they encounter the region of compressive stresses. As the two halves of the specimens resulting from propagation of the splitting crack continue to bend, new radial cracks form, and new relative peaks can be found in the load-deformation diagram.

- Stress transfer along the surfaces of the wedge is not included for simulating penetration of the wedge into the specimen.

# Appendix B

# Supercomputing facilities

The use of supercomputing facilities is essential in the case of 3D lattice analyses because of the enormous number of degrees of freedom. In a lattice analysis the size of the problem is governed by the size of the stiffness matrix and of the resulting system of linear equations, that can be solved semi-independently. As lattice analyses do not require large memory space and are relatively modest in I/O communication, the performance depends on the scalability to the number of processors.

The lattice algorithm, already included in the Finite Element software DIANA, was later also included in ScaFIEP (Scalable Finite Element Package) [59]. ScaFIEP is built entirely in C++ and uses the MPI library for communication between the processors. Except for the analysis of the Brazilian test (see Appendix A), which was performed using DIANA, all other analyses included in this thesis were conducted with ScaFIEP. The 2D and 3D uni-axial experiments reported in Chapter 4 and Chapter 5 were conducted on a Cray T3E available at the HPAC of TU Delft, while the torsion experiment reported in Chapter 6 was conducted on the SGI Origin 3000 TERAS located at SARA in Amsterdam. For running this analysis a NCF grant was requested for 5000 CPU-hours. However, as this time was not sufficient to capture the softening regime, a new grant was requested later on. A comparison in performance between the TERAS and the Cray is reported in Table B.1. Table B.1 reports the User Time (UTime) as an average of three runs over ten steps. The specimen used in the TERAS was the same cylinder as in the torsion experiment (see Chapter 6), while the specimen used in the Cray was a relatively small prism with 56936 elements. The scaling results on the TERAS suggest that scaling does not play an important role while scaling is much more problematic on the Cray.

| CPU | TERAS (449179 beams) | | Cray (56936 beams) | |
|-----|---------|---------|---------|---------|
|     | UTime[s] | scaling | UTime[s] | scaling |
| 256 | 33.64   | 1.37    |         |         |
| 128 | 45.98   | 2.01    |         |         |
| 64  | 92.86   | 4.47    | 30.31   | 1.28    |
| 32  | 414.88  | 1.93    | 38.82   | 1.31    |
| 16  | 799.03  | 1.97    | 50.93   | 1.71    |
| 8   | 1573.91 | 1.53    | 87.17   | 1.76    |
| 4   | 2402.53 |         | 153.80  |         |

Table B.1: Scaling of the lattice module implemented in ScaFIEP.

# Bibliography

[1] F.E. Amparano, Y. Xi, and Y.S. Roh. Experimental study on the effect of aggregate content on fracture behaviour of concrete. *Engineering Fracture Mechanics*, 67(1):65–84, 2000.

[2] M. Anson and K. Newman. The effect of mix proportions and method of testing on poisson's ratio for mortar and concretes. *Magazine of Concrete Research*, 18(1):115–130, 1966.

[3] A. Arslan, R. Ince, and B.L. Karihaloo. Improved lattice model for concrete fracture. *Journal of Engineering Mechanics (ASCE)*, 128(1):57–65, 2002.

[4] A. Arslan, E. Schlangen, and J.G.M. van Mier. Effect of model fracture law and porosity on tensile softening of concrete. In F.H. Wittmann, editor, *Fracture Mechanics of Concrete Structures*, pages 45–54. AEDIFICATIO Publishers, 1995.

[5] G.I. Barenblatt. The mathematical theory of equilibrium of cracks in brittle fracture. *Advances in Applied Mechanics*, 7:55–129, 1962.

[6] Z. Bažant, P. C. Prat, and M. R. Tabbara. Antiplane shear fracture tests (Mode III). *ACI Materials Journal*, 87:12–19, 1990.

[7] Z. Bažant, M.R. Tabarra, T. Kazemi, and G. Pijaudier-Cabot. Random particle model for fracture of aggregate or fiber composites. *Journal of Engineering Mechanics (ASCE)*, 116(8):1686–1705, 1990.

[8] Z.P. Bažant. Instability, ductility, and size effect in strain-softening concrete. *Journal of Engineering Mechanics (ASCE)*, 102(2):331–344, 1976.

[9] Z.P. Bažant. Imbricate continuum and its variational derivation. *Journal of Engineering Mechanics (ASCE)*, 110(12):1693–1712, 1984.

[10] Z.P. Bažant and M.T. Kazemi. Determination of fracture energy, process zone length and brittleness number from size effect, with application to rock and concrete. *International Journal of Fracture*, 44(2):111–131, 1990.

[11] Z.P. Bažant, M.T. Kazemi, T. Hasegawa, and J. Mazars. Size effect in brazilian split-cylinder tests: measurements and fracture analysis. *ACI Materials Journal*, 88(3):325–332, 1991.

[12] Z.P. Bažant and B.H. Oh. Crack band theory for fracture of concrete. *Materials and Structures (RILEM)*, 16(3):155–177, 1983.

[13] Z.P. Bažant and P.A. Pfeiffer. Shear fracture test of concrete. *Materials and Structures (RILEM)*, 110(19):111–121, 1986.

[14] T.B. Belytschko, M. Plesha, and C.H. Dowding. A computer method for stability analysis of caverns in jointed rocks. *International Journal for Numerical and Analytical Methods in Geomechanics*, 8(5):473–492, 1984.

[15] A. Bentur and M.D. Cohen. Effect of condensed silica fume on the microstructure of the interfacial zone in portland cement mortars. *Journal of the American Ceramic Society*, 70(10):738–743, 1987.

[16] W.J. Beranek and G.J. Hobbelman. Constitutive modelling of structural concrete as an assemblage of spheres. In H. Mang, N. Bicanic, and R. De Borst, editors, *Computational Modelling of Concrete Structures*, pages 535–542. Pineridge Press, 1994.

[17] S. Berton and J.E. Bolander. Crack band model of fracture in irregular lattices. *Computer Methods in Applied Mechanics and Engineering*, 195:7172–7181, 2006.

[18] J.E. Bolander and Y. Kobashi. Size effect mechanisms in numerical concrete fracture. In F.H. Wittmann, editor, *Fracture Mechanics of Concrete Structures*, pages 535–542. AEDIFICATIO Publishers, 1995.

[19] N. J. Burt and J. W. Dougill. Progressive failure in a model heterogeneous medium. *Journal of Engineering Mechanics (ASCE)*, 103(3):365–376, 1977.

[20] A. Caballero, I. Carol, and C.M. López. A meso-level approach to the 3D numerical analysis of cracking and fracture of concrete materials. *Fatigue & Fracture of Engineering Materials & Structures*, 29(12):979–991, 2006.

[21] H.A. Carmona, F. Kun, J.S. Andrade Jr., and H.J. Herrmann. Computer simulation of fatigue under diametrical compression. *Physical Review B*, submitted.

[22] M.D. Cohen, A. Goldman, and W.F. Chen. The role of silica fume in mortar: Transition zone versus bulk paste modification. *Cement and Concrete Research*, 24(1):95–98, 1994.

[23] P.A. Cundall and O.D.L. Strack. A discrete numerical model for granular assemblies. *Géotechnique*, 29(1):47–65, 1979.

[24] G. Cusatis, Z.P. Bažant, and L. Cedolin. Confinement-shear lattice model for concrete damage in tension and compression:I. Theory. *Journal of Engineering Mechanics (ASCE)*, 129(12):1439–1448, 2003.

[25] G. Cusatis and L. Cedolin. Two-scale study of concrete fracturing behaviour. *Engineering Fracture Mechanics*, 74:3–17, 2007.

[26] J.P.B. de Barros Leite and V. Slowik. Simulation of concrete fracture by using mesolevel truss and particle models. In V.C. Li, C.K.Y. Leung, K.J. Willam, and S.L. Billington, editors, *Fracture Mechanics of Concrete Structures*, pages 337–344, 2004.

[27] J.P.B. de Barros Leite, V. Slowik, and H. Mihashi. Computer simulation of fracture processes of concrete using mesolevel models of lattice structures. *Cement and Concrete Research*, 34(6):1025–1033, 2004.

[28] R. De Borst and H.-B. Mühlhaus. Gradient-dependent plasticity-formulation and algorithmic aspects. *International Journal for Numerical Methods in Engineering*, 35(3):521–539, 1992.

[29] K. Duan and J.G.M. van Mier. Crack growth in four concretes under monotonic or cyclic splitting load. In A. Azizinamini, D. Darwin, and C. French, editors, *High Strength Concrete*, pages 444–456. ASCE, 1999.

[30] D.S. Dugdale. Yielding of steel sheets containing slits. the mathematical theory of equilibrium of cracks in brittle fracture. *Journal of the Mechanics and Physiscs of Solids*, 8(2):100–108, 1960.

[31] K.M. El-Sayed, G.V. Guinea, C. Rocco, J. Planas, and M. Elices. Influence of aggregate shape on the fracture behaviour of concrete. In H. Mihashi and K. Rokugo, editors, *Fracture mechanics of concrete structures*, pages 171–181. Aedificatio Publishers, 1998.

[32] J. Farran. Contribution minéralogique á l'etude de l'adhérence entre constituants hydratés des ciments et les matériaux enrobés. *Matériaux et constructions*, 490-91:155–172, 1956.

[33] N.Q. Feng, X.H. Ji, Q.F. Zhuang, and J.T. Ding. Effect of concrete materials on fracture performance. In F.H. Wittmann, editor, *Fracture mechanics of concrete structures*, pages 119–124. Aedificatio Publishers, 1995.

[34] Escadeillas G. and J.C. Maso. Approach of the initial state in cement paste, mortar and concrete. In S. Mindess, editor, *Advances in cement materials, Ceramic Transactions vol. 16*, pages 169–184. American Ceramic Society, 1991.

[35] G. Giaccio and R. Zerbino. Combined effects of coarse aggregates and strength level. *Advanced Cement Based Materials*, 7(2):41–48, 1998.

[36] A. A. Griffith. The phenomena of rupture and flow in solids. *Philosofical Transactions of the Royal Society of London*, 221:163–198, 1921.

[37] P. Gu, P. Xie, and J.J. Beaudoin. Microstructural characterization of the transition zone in cement systems by means of A.C. impedance spectroscopy. *Cement Concrete Research*, 23(3):581–591, 1993.

[38] D.J. Hannant, K.J. Buckley, and J. Croft. The effect of aggregate size on the use of the cylinder splitting test as a measure of tensile strength. *Matériaux et Constructions*, 6(31):15–21, 1973.

[39] Z. Hashin. Analysis of composite materials: a survey. *Journal of Applied Mechanics*, 50:481–505, 1983.

[40] Z. Hashin and J. Shtrikman. A variational approach to the theory of elastic behaviour of multiphase materials. *Journal of Mechanics and Physics of Solids*, 11:127–140, 1963.

[41] H. J. Herrmann, A. Hansen, and S. Roux. Fracture of disordered, elastic lattices in two dimensions. *Physical Review B*, 39(1):637–648, 1989.

[42] A. Hillerborg, M. Modéer, and P. E. Petersson. Analysis of crack formation and crack growth in concrete by means of fracture mechanics and finite elements. *Cement and Concrete Research*, 6:773–782, 1976.

[43] A. Hrennikoff. Solution of problems of elasticity by the framework method. *Journal of Applied Mechanics*, 12:169–175, 1941.

[44] D. Hull. Tilting cracks: the evolution of fracture surface topology in brittle solids. *International Journal of Fracture*, 62(2):119–138, 1993.

[45] A.R. Ingraffea and V. Saouma. Numerical modelling of discrete crack propagation in reinforced and plain concrete. In G.C. Sih and A. Di Tommaso, editors, *Fracture Mechanics of Concrete. Structural Application and Numerical Calculation*, pages 171–222. Martinus Nijhoff Publishers, 1985.

[46] G. Irwin. Analysis of stresses and strains near the end of a crack traversing a plate. *Journal of Applied Mechanics*, 24:361–364, 1957.

[47] Grandet J. and Ollivier J.P. New method for the study of cement-aggregate interfaces. In *Proceedings of the Seventh International Congress on Chemistry of Cement*, volume 7, pages 85–89, 1980.

[48] M. Jirásek and Z.P. Bažant. Particle model for quasi-brittle fracture and application to sea ice. *Journal of Engineering Mechanics*, 121(9):1016–1025, 1995.

[49] Y.C. Kan and S.E. Swartz. The effects of mix variables on concrete fracture mechanics parameters. In F.H. Wittmann, editor, *Fracture mechanics of concrete structures*, pages 111–118. Aedificatio Publishers, 1995.

[50] T. Kawai. New discrete models and their application to seismic response analysis. *Nuclear Engineering and Design*, 48:207–229, 1978.

[51] H. Kawakami. Effect of aggregate type on the mechanical behaviour of concrete. In J.C. Maso, editor, *Interfaces in cementitious composites*. E & FN Spon, 1993.

[52] F. Kun, G.A. D'Addetta, H.J. Herrmann, and E. Ramm. Two-dimensional dynamic simulation of fracture and fragmentation of solids. *Computed Assisted Mechanics and Engineering Sciences*, 6:385–402, 1999.

[53] A.K.H. Kwan, Z.M. Wang, and H.C. Chan. Mesoscopic study of concrete II: non-linear finite element analysis. *Computers & Structures*, 70(5):545–556, 1999.

[54] D. Lasry and T. Belytschko. Localisation limiter in transient problems. *International Journal of Solids and Structures*, 24(6):581–597, 1988.

[55] G. Lilliu, A. Meda, C. Shi, and J.G.M. van Mier. Effect of particle density on tensile fracture properties of model concrete. In M.A.N. Hendriks and J.G. Rots, editors, *Finite Elements in Civil Engineering Applications*, pages 69–78. A.A. Balkema Publishers, 2003.

[56] G. Lilliu and J. G. M. van Mier. Analysis of crack growth in the brazilian test. In R. Eligehausen, editor, *Construction Materials: Theory and Application (H.W. Reinhardt 60$^{th}$ birthday commemorative volume)*, pages 123–137. IBIDEM Verlag, 1999.

[57] G. Lilliu and J.G.M. van Mier. Simulation of 3D crack propagation with the lattice model. In *Proceedings International Congress on Advanced Materials, their Processes and Applications*, 2000.

[58] G. Lilliu and J.G.M. van Mier. Experimental investigation of fracture processes in concrete cylinders subjected to torsion. In R. de Borst, J. Mazars, G. Pijaudier-Cabot, and J.G.M. van Mier, editors, *Fracture Mechanics of Concrete Structures*, pages 395–402. A.A. Balkema Publishers, 2001.

[59] F.J. Lingen. *Design of an object oriented Finite Element package for parallel computers*. PhD thesis, Delft University of Technology, 2000.

[60] J. Margoldová and J.G.M. van Mier. Simulation of compressive fracture in concrete. In K.H. Schwalbe and C. Berger, editors, *Structural Integrity: Experiments, Models, Applications*, pages 1399–1408. EMAS Publishers, 1994.

[61] P.K. Mehta and P.J.M. Monteiro. Effect of aggregate, cement, and mineral admixtures on the microstructure of the transition zone. In S. Mindess and P.S. Shah, editors, *Bonding in Cementitious Composites*, pages 65–75. Materials Reserch Society, 1988.

[62] C. Moukarzel and H.J. Herrmann. A vectorizable random lattice. *Journal of Statistical Physics*, 68(5-6):911–923, 1992.

[63] K. Nagai, Y. Sato, and T. Ueda. Three-dimensional mesoscopic analyses of mortar and concrete model by rigid spring model. In V.C. Li, C.K.Y. Leung, K.J. Willam, and S.L. Billington, editors, *Fracture Mechanics of Concrete Structures*, pages 353–360, 2004.

[64] A. Needleman. Material rate dependence and mesh sensitivity in localization problems. *Computer Methods in Applied Mechanics and Engineering*, 67(1):69–85, 1988.

[65] M.B. Nooru-Mohamed. *Mixed mode fracture of concrete: an experimental approach*. PhD thesis, Delft University of Technology, 1992.

[66] M.B. Nooru-Mohamed, E. Schlangen, and J.G.M. van Mier. Experimental and numerical study on the behaviour of concrete subjected to biaxial tension and shear. *Advanced Cement Based Materials*, 1(1):22–37, 1993.

[67] R.H.J. Peerlings, R. De Borst, W.A.M. Brekelmans, and M.G.D. Geers. Gradient-enhanced damage modelling of concrete fracture. *Mechanics of Cohesive Frictional Materials*, 3(4):323–342, 1998.

[68] J.P. Petit and M. Barquins. Can natural faults propagate under Mode II conditions? *Tectonics*, 7(6):1243–1256, 1988.

[69] G. Pijaudier-Cabot and Z.P. Bažant. Nonlocal damage theory. *Journal of Engineering Mechanics (ASCE)*, 113:1512–1533, 1987.

[70] X. Ping and J.J. Beaudoin. Modification of transition zone microstructure-silica fume coating of aggregate surfaces. *Cement Concrete Research*, 22:597–604, 1992.

[71] D.O. Potyondy and P.A. Cundall. A bonded-particle model for rock. *International Journal of Rock Mechanics & Mining Sciences*, 41(8):1329–1364, 2004.

[72] C. Rocco, G.V. Guinea, J. Planas, and M. Elices. Mechanisms of rupture in splitting tests. *ACI Materials Journal*, 96(1):52–60, 1999.

[73] C. Rocco, G.V. Guinea, J. Planas, and M. Elices. Size effect and boundary conditions in the brazilian test: experimental verification. *Materials and Structures (RILEM)*, 32(3):210–217, 1999.

[74] P. E. Roelfstra, H. Sadouki, and F. H. Wittmann. Le béton numérique. *Materials and Structures (RILEM)*, 18(5):327–335, 1987.

[75] P. Rossi and S. Richer. Numerical modelling of concrete cracking based on a stochastic approach. *Materials and Structures (RILEM)*, 20(5):334–337, 1987.

[76] J.G. Rots. *Computational modelling of concrete fracture*. PhD thesis, Delft University of Technology, 1988.

[77] J.G. Rots and S. Invernizzi. Saw-tooth softening/stiffening model. In V.C. Li, C.K.Y. Leung, K.J. Willam, and S.L. Billington, editors, *Fracture Mechanics of Concrete Structures*, pages 375–382, 2004.

[78] M. Saito and M. Kawamura. Effect of fly ash and slag on the interfacial zone between cement and aggregate. In V.M. Malhotra, editor, *Fly Ash, Silica Fume, and Natural Pozzolans in Concrete*, pages 669–688. American Concrete Institute, 1989.

[79] E. Schlangen. *Experimental and numerical analysis of fracture processes in concrete*. PhD thesis, Delft University of Technology, 1993.

[80] E. Schlangen and E.J. Garboczi. Fracture simulations of concrete using lattice models: computational aspects. *Engineering Fracture Mechanics*, 57(2/3):319–332, 1997.

[81] E. Schlangen and J.G.M. van Mier. Experimental and numerical analysis of micromechanisms of fracture of cement-based composites. *Cement and Concrete Composites*, 14:105–118, 1992.

[82] E. Schlangen and J.G.M. van Mier. Shear fracture in cementitious composites. part II: numerical simulations. In Z.P. Bažant, editor, *Fracture Mechanics of Concrete Structures*, pages 671–676. Elsevier Applied Science Publishers, 1992.

[83] E. Schlangen and J.G.M. van Mier. Lattice model for simulating fracture of concrete. In F.H. Wittmann, editor, *Numerical Models in Fracture Mechanics of Concrete*, pages 195–205. A.A. Balkema Publishers, 1993.

[84] E. Schlangen and J.G.M. van Mier. Fracture simulations in concrete and rock using a random lattice. In H. Siriwardane and M.M. Zaman, editors, *Computer Methods and Advances in Geomechanics*, pages 1641–1646. A.A. Balkema Publishers, 1994.

[85] H. Schorn and U. Rode. 3D-modelling of process zone in concrete by numerical simulations. In S.P. Shah and S.E Swartz, editors, *Proceedings International Conference on Fracture of Concrete and Rock*, pages 220–228. Springer Verlag, 1989.

[86] P. Simeonov and S. Ahmad. Effect of transition zone on the elastic behaviour of cement-based composites. *Cement and Concrete Research*, 25:164–176, 1995.

[87] J.C. Simo, J. Oliver, and F. Armero. An analysis of strong discontinuities induced by strain softening in rate-independent inelastic solids. *Computational Mechanics*, 12(5):277–296, 1993.

[88] L.J. Sluys and R. De Borst. Wave-propagation and localization in a rate dependent cracked medium: Model formulation and one-dimensional examples. *International Journal of Solids and Structures*, 29(23):2945–2958, 1992.

[89] K.A. Snyder, D.N. Winslow, D.P. Bentz, and E.J. Garboczi. Interfacial zone percolation in cement-aggregate composites. In J.C. Maso, editor, *Interfaces in cementitious composites*, pages 259–268. E & FN Spon, 1992.

[90] M. Stroeven. *Discrete numerical modelling of composite materials*. PhD thesis, Delft University of Technology, 1999.

[91] A.S.J. Suiker, A.V. Metrikine, and R. De Borst. Comparison of wave propagation characteristics of the cosserat continuum model and corresponding discrete lattice models. *International Journal of Solids and Structures*, 38:1563–1583, 2001.

[92] C. Tasdemir, M.A. Tasdemir, F.D. Lydon, and B.I.G. Barr. Effects of silica fume and aggregate size on the brittleness of concrete. *Cement and Concrete Research*, 26(1):63–68, 1996.

[93] W.A. Tasong, C.J. Lynsdale, and J.C. Cripps. Aggregate-cement paste interface. Part I: Influence of aggregate geochemistry. *Cement Concrete Research*, 29:1019–1025, 1999.

[94] F. Tzschichholz. Peeling instability in cosserat-like media. *Physical Review B*, 45(22):12691–12698, 1992.

[95] J.G.M. Van Mier. *Strain softening of concrete under multiaxial loading conditions*. PhD thesis, Eindhoven University of Technology, 1984.

[96] J.G.M. van Mier. Mode I fracture of concrete: discontinuous crack growth and crack interface grain bridging. *Cement and Concrete Research*, 21(1):1–15, 1991.

[97] J.G.M. Van Mier. Reality behind fictitious crack? In V.C. Li, C.K.Y. Leung, K. Willam, and S.L. Billington, editors, *Fracture Mechanics of Concrete Structures*, pages 11–30. A.A. Balkema Publishers, 2004.

[98] J.G.M. van Mier, B. Chiaia, and A. Vervuurt. Numerical simulation of chaotic and self-organizing damage in brittle disordered materials. *Computer Methods in Applied Mechanics and Engineering*, 142(1-2):189–201, 1997.

[99] J.G.M. Van Mier, E. Schlangen, and M.B. Nooru-Mohamed. Shear fracture in cementitious composites. Part I: Experimental observations. In Z.P Bažant, editor, *Fracture Mechanics of Concrete Structures*, pages 659–670. Elsevier Applied Science Publishers, 1992.

[100] J.G.M. van Mier and C. Shi. Stability issues in uniaxial tensile tests on brittle disordered materials. *International Journal of Solids and Structures*, 39(13/14):3359–3372, 2002.

[101] M. R. A. van Vliet. *Size effect in tensile fracture of concrete and rock*. PhD thesis, Delft University of Technology, 2000.

[102] M.R.A. van Vliet and J.G.M. van Mier. Comparison of lattice type fracture models for concrete under biaxial loading regimes. In A. Carpinteri, editor, *Size-Scale Effects in the Failure Mechanisms of Materials and Structures*, pages 43–57. E & FN Spon, 1996.

[103] A. Vervuurt. *Interface fracture in concrete*. PhD thesis, Delft University of Technology, 1997.

[104] A. Vervuurt, J.G.M. van Mier, and E. Schlangen. Analyses of anchor pull-out in concrete. *Materials and Structures (RILEM)*, 27(5):251–259, 1994.

[105] R.A. Vonk. *Softening of concrete loaded in compression*. PhD thesis, Delft University of Technology, 1992.

[106] J.C. Walraven. *Aggregate interlock: a theoretical and experimental analysis*. PhD thesis, Delft University of Technology, 1980.

[107] R. Wasserman and A. Bentur. Interfacial interactions in lightweight aggregate concretes and their influence on the concrete strength. *Cement & Concrete Composites*, 18(1):67–76, 1996.

[108] J. P. Watt, G. F. Davies, and R. J. O'Connell. The elastic properties of composite materials. *Review of Geophysics and Space Physics*, 14:541–563, 1976.

[109] G.N. Wells. *Discontinuous modelling of strain localization and failure*. PhD thesis, Delft University of Technology, 2001.

[110] H.M. Westergaard. Bearing pressures and cracks. *Journal of Applied Mechanics*, 6:49–53, 1939.

[111] K.R. Wu, B. Chen, W. Yao, and D. Zhang. Effect of coarse aggregate type on mechanical properties of high-performance concrete. *Cement and Concrete Research*, 31(10):1421–1425, 2001.

[112] D. Xu and H. W. Reinhardt. Softening of concrete under torsional loading. In S. P. Shah, S. E. Swartz, and B. Barr, editors, *Fracture of Concrete and Rock: Recent Developments*, pages 39–50. Elsevier Applied Science, 1989.

[113] Z. Yacoub-Tokatly, B. Barr, and P. Norris. Mode III fracture - A tentative test geometry. In S. P. Shah, S. E. Swartz, and B. Barr, editors, *Fracture of Concrete and Rock: Recent Developments*, pages 596–604. Elsevier Applied Science, 1989.

[114] M.H. Zhang and O.E. Gjørv. Microstructure of the interfacial zone between lightweight aggregate and cement paste. *Cement Concrete Research*, 20:610–618, 1990.

[115] F.P. Zhou, F.D. Lydon, and B.I.G. Barr. Effect of coarse aggregate on elastic modulus and compressive strength of high performance concrete. *Cement and Concrete Research*, 25(1):177–186, 1995.

[116] D.G. Zollinger, T. Tang, and R.H. Yoo. Fracture toughness of concrete at early ages. *ACI Materials Journal*, 90(5):463–471, 1993.

# Summary

Modelling fracture processes in concrete requires that material heterogeneity and displacement discontinuity are taken into account. Classical models of concrete fracture assume the material as homogeneous and/or the displacements as continuous, and are based on the concept of *material softening*. As softening is the result of a combined effect of material behaviour, geometry of the structure, boundary and loading conditions, these models are, as a matter of fact, encompassing structural effects into the material behaviour. For this reason, such models are unable to give more insight in the causes of softening and in the influence of different parameters on it.

Lattice models, on the contrary, can take into account both material heterogeneity and displacement discontinuity in a straightforward manner. The first is achieved by overlaying a computer-generated particle distribution on the lattice and assigning different mechanical properties to the lattice elements falling in each of the three phases: aggregate, matrix and interfacial transition zone. The second is achieved by the sequential removal of lattice elements that exceed the tensile strength. The advantage of this model is that, despite the local linear elastic brittle response, structural softening is still obtained.

One limitation to the application of lattice models is the computer power and computer time, which can be overcome by using parallel computing facilities. Another disadvantage of the model is that it gives a too brittle response in terms of load-displacement diagrams, in comparison with laboratory experiments. The major causes of lattice brittleness are two: 1) the accuracy in schematizing the material structure; 2) 3D effects, which are not considered in the 2D versions of lattice models.

Both influence of the material structure and of 3D effects have been investigated in this thesis, where a 3D version of a pre-existing 2D beam lattice model has been developed. The results show how the material structure influences both structural strength and post-peak behaviour, with emphasis to the decisive role of the interfacial transition zone, especially in the pre-peak regime and at peak. Comparison between 2D and 3D lattices highlights that 3D effects are determinant for a more ductile structural response.

3D effects are important in modelling concrete fracture even when mechanics theory would predict a planar crack, due to the random 3D particle distribution, which determines the fracture process and the final crack pattern. However, there are cases when it is known *a priori* that 3D cracks develop, such as in the torsion test. For this reason, a torsion test where a spiralling crack develops along the specimen's height has been used in this thesis to validate the 3D beam lattice model. Comparison of numerical and labora-

tory experiments show that the 3D beam lattice model can capture both the correct crack pattern and torque-rotation diagram.

Giovanna Lilliu

# Samenvatting

Het modelleren van breukprocessen vereist het in rekening brengen van de inhomogeniteit van het materiaal en van de discontinuïteit van de verplaatsingen. Klassieke modellen voor de breuk van beton beschouwen het materiaal als homogeen en/of de verplaatsingen als continu, en zijn gebaseerd op een geleidelijke afname van de strekte van het materiaal. Omdat de afname van de sterkte een constructie het resultaat is van zowel materiaalgedrag, als van de geometrie van de constructie, als van de randvoorwaarden en belastingen, verdisconteren deze modellen feitelijk constructieve aspecten in het materiaalgedrag. Hierom zijn klassieke modellen niet in staat meer inzicht de geven in de oorzaken van de voortgaande degradatie van de sterkte van een constructie en de invloed van de verschillende parameters op deze degradatie.

*Lattice* modellen, daarentegen, kunnen zowel de inhomogeniteit van het materiaal als ook de discontinuïteit van de verplaatsingen rechtstreeks verdisconteren. Het eerste wordt bewerkstelligd door een korrelstructuur te projecteren op het raamwerk van het *lattice* model, en verschillende mechanische eigenschappen toe te kennen aan drie fasen: toeslagmateriaal, matrix en een grenslaagzone. Het tweede wordt bewerkstelligd door het achtereenvolgens verwijderen van die elementen van het raamwerk die de treksterkte overschrijden. Het voordeel van deze modellering is dat, ondanks dat lokaal sprake is van bros gedrag, op constructieniveau een geleidelijke degradatie van de sterkte van de constructie kan worden verkregen.

De toepassing van *lattice* modellen wordt beperkt door de rekenkracht en de rekentijd van computers. Deze beperking kan tenietgedaan worden door de toepassing van parallel rekenen. Een ander nadeel van *lattice* modellen is dat zij een té bros gedrag vertonen in vergelijk met experimenten. De belangrijkste oorzaak is tweeledig: 1) de nauwkeurigheid van de schematisering van de materiaalstructuur; 2) 3D effecten, welke buiten beschouwing genomen worden in 2D *lattice* modellen.

Zowel de invloed van de materiaalstructuur als de invloed van 3D effecten zijn in dit proefschrift bestudeerd. Hierbij is een 3D versie ontwikkeld uitgaande van het reeds bestaande 2D *lattice* model op basis van balkelementen. De resultaten laten zien hoe de materiaalstructuur invloed heeft op zowel de pieksterkte van de constructie als op ook op het na-piek-gedrag. Er wordt een doorslaggevende rol aangetoond voor de grenslaagzone, vooral op het voor-piek-gedrag en de pieksterkte. Vergelijkingen tussen 2D en 3D *lattice* modellen bevestigen dat 3D effecten bepalend zijn voor het verkrijgen van een meer taai gedrag.

147

3D effecten zijn belangrijk bij het modeleren van breuk in beton. Dit is zelfs het geval wanneer een mechanische beschouwing een vlak breukvlak voorspelt. De 3D materiaalstructuur is dan bepalend voor het breukproces en het uiteindelijke scheurpatroon. Echter, er zijn ook gevallen waarbij het *a priori* bekend is dat een 3D scheurpatroon ontwikkeld. Dit is het geval bij de torsie-test. Om deze reden is de torsie-test, waarbij een spiraalvormig scheurpatroon ontstaat over de hoogte van het proefstuk, gebruikt om het 3D *lattice* model op basis van balkelementen te valideren. Een vergelijking van de numerieke resultaten en de experimentele resultaten laten zien dat het 3D *lattice* model in staat is om zowel het scheurpatroon als het moment-rotatie diagram te simuleren.

Giovanna Lilliu

# Propositions

1. Realistic modelling of fracture processes in concrete requires material heterogeneity and displacement discontinuity to be taken into account.

2. A major advantage of lattice modelling over homogeneous-continuum models is the possibility to simulate structural softening without introducing material softening.

3. Market life of a product is as prone to softening as concrete.

4. Most elegant models contain a minimum number of essential parameters.

5. Quality of a conference is inverse proportional to the beauty of the conference site.

6. Multi-processing has been natural for women long before parallel analysis was introduced.

7. Living abroad boosts appreciation of one's own country.

8. Tolerance is often another name for indifference.
   *(adapted from Maugham W. Somerset)*

9. There is no revenge as complete as forgiveness.
   *(John Billings)*

10. Linguistic development of a multilingual child can be harmed by parents speaking to him/her another language than their mother tongue.

These propositions are considered opposable and defendable and as such have been approved by the supervisor, Prof.dr.ir. J.G.M. van Mier.

149

# Stellingen

1. Het realistisch modelleren van breukprocessen in beton vereist het in rekening brengen van de inhomogeniteit van het materiaal en van de discontinuïteit van de verplaatsingen.

2. Een belangrijk voordeel van *lattice* modellen ten opzichte van continuüm modellen is de mogelijkheid de degradatie van de sterkte van een constructie te modelleren zonder een geleidelijke degradatie van de sterkte van het materiaal te introduceren.

3. Het leven van een product in de markt is even vatbaar voor verval als de sterkte van beton.

4. De elegantste modellen bevatten het minimum aantal essentiële parameters.

5. De kwaliteit van conferenties is omgekeerd evenredig met de schoonheid van de conferentielocatie.

6. Lang voor de introductie van parallel rekenen was *multi-processing* voor vrouwen gewoon.

7. Verblijf in het buitenland stimuleert de waardering voor het moederland.

8. Tolerantie is vaak een ander woord voor onverschilligheid.
   *(vrij naar Maugham W. Somerset)*

9. Er is geen wraak zo volledig zoals vergeving.
   *(John Billings)*

10. De taalontwikkeling van een meertalig kind kan beschadigd raken als het door de ouders niet in hun moedertaal wordt aangesproken.

Deze stellingen worden opponeerbaar en verdedigbaar geacht en zijn als zodanig goedgekeurd door de promotor, Prof.dr.ir. J.G.M. van Mier.

# Curriculum vitae

| | |
|---|---|
| 16 May 1966 | born in Tuili (Cagliari), Italy, as Giovanna Lilliu |
| 1985 | high school diploma (classical studies)<br>Liceo Classico Siotto Pintor, Cagliari, Italy |
| 1994 | degree in Civil Engineering, cum laude<br>Facoltá di Ingegneria Civile, Cagliari, Italy |
| 1997 | postgraduate school diploma<br>Scuola di Specializzazione F.lli Pesenti,<br>Politecnico di Milano, Italy |
| 1997-2002 | PhD researcher, Microlab,<br>Delft University of Technology, The Netherlands |
| since 2003 | Sales engineer, TNO DIANA BV, Delft, The Netherlands |

Concrete fracture is governed by randomly distributed aggregate particles, which make cracks fundamentally not planar. This phenomenon can be captured only by 3D models. Within the 3D framework, material heterogeneity and displacement discontinuity must be incorporated. Lattice models allow to consider all these aspects adequately. In this thesis a lattice model is used to analyze the influence of the material structure on the global structural response and to compare results from 2D and 3D modelling. Concrete is schematized as a network of beams with different mechanical properties corresponding to three phases: aggregate, matrix, and interfacial transition zone. Fracture is mimicked by sequential removal of elements where the stress exceeds the tensile strength. Though a purely brittle linear elastic behaviour is assumed for each element, structural softening is modelled successfully.